

Experimental Investigation of the Tractive Performance of an Instrumented Off Road Tire on a Soft  
Soil Terrain

Scott David Naranjo

Thesis submitted to the faculty of the Virginia Polytechnic Institute and State University in partial  
fulfillment of the requirements for the degree of

Master of Science  
In  
Mechanical Engineering

Corina Sandu, Chair  
Saied Taheri  
Paramsothy Jayakumar

June 7<sup>th</sup> 2013  
Blacksburg, VA

Keywords: terramechanics, tires, soft soil, single wheel tester, tire instrumentation

# Experimental Investigation of the Tractive Performance of an Instrumented Off Road Tire on a Soft Soil Terrain

Scott David Naranjo

## ABSTRACT

The main goal of this study is to improve the understanding of the interaction between a pneumatic tire and deformable terrain. A design of experiments has been implemented, that gives insight into the effect of individual tire and soil parameters, specifically wheel slip, normal load, inflation pressure, and soil compaction, as well as into the effect of combinations of such parameters on the tire and soil behavior. The results of such test data is exceedingly relevant, providing significant information to tire design for tire manufacturers, to users for operating conditions selection, as well as providing modeling parameters for tire models. Moreover, experimental investigation of tire-soil interaction provides validation data for tire models operating under similar conditions. In support of the validation of a soft soil tire model currently being developed at Virginia Tech under the auspices of the Automotive Research Center, experimental work has been performed on a low-speed, indoor single-wheel tester built to investigate studies in terramechanics. The terramechanics rig provides a well-controlled environment to assure repeatable testing conditions and void vehicle component effects. The test tire for the rig is instrumented with a wireless sensory system that measures tire deflection at the contact patch; combining this system with other instruments of the rig allows accurate estimations of wheel sinkage. A methodical soil preparation procedure has rendered great data to analyze several relations, such as the drawbar pull and the sinkage dependency on slip. The data collected indicated that, when looking at the effect of individual parameters, by increasing the soil compaction, the normal load, and by decreasing the inflation pressure will result in a higher normalized drawbar pull. A higher normal load under all conditions consistently lowered the max tire sinkage depth. The sinkage has increased dramatically with the slip ratio, growing threefold larger at high slip (70-90%) when compared to lower slip (0-5%) ratios.

## Acknowledgements

I would like to thank Dr. Corina Sandu for being my advisor and constantly giving me support and encouragement despite how difficult the situation. It was in her Intro to ME Design class that I was first introduced to Terramechanics, which inspired me to do undergraduate research that lead to this thesis work. Since then, I have met several professors, industry and military professionals, and many other great minds in the field that kept me inspired in my work. I am forever grateful to her for this educational experience, funding my studies, and being hands-down the best mentor.

Also, I would like to thank Dr. Saied Taheri for being part of my committee and being a great mentor. Since my Senior Design project, I have learned so much from Dr. Taheri's advice stemming from his great research in tires and vehicle dynamics and experience in the automotive industry.

Additionally, I would like to thank Dr. Paramsothy Jayakumar for being on my committee and teaching me about the constant army needs that should be addressed in this research.

Special thanks to the Automotive Research Center (ARC) for providing the majority of funds for this study. Moreover, I thank the ARC for giving me the opportunity to network with industry and military professionals, especially the quad members of this project.

I would like to thank several past and current colleagues at the Center for Vehicle Systems and Safety (CVeSS). Great input that was received for this study came from Troy Holley, Adam Woodward, Eduardo Pinto, Anake Umsrithong, Jody Priddy, Shahyar Taheri and several other undergraduate students, Tarek Shalaby, Michael Smith, and Matt Givens, that were always happy to help with my research and learn valuable engineering applications. I would like to thank Michael Craft for his great input in machining, electronics, and design. I would like to thank Dr. Mehdi Ahmadian who not only was a great professor and mentor, but also treated me as his own student throughout my time at CVeSS. I would like to thank Sue Teel for her great motherly support during my transition into being a graduate student at CVeSS. Very special thanks to Clément Nagode, who was a great friend with a brilliant mind that helped me to tackle several challenges in my work - no matter the time of day!

Furthermore, a special thanks to my lovely companion, Jessica Lam, who gave great support throughout my studies to keep me motivated with a smile on my face, and who pitched in to help review my writing whenever I needed. I give thanks to the several friends throughout my undergraduate and graduate studies for all the great experiences.

Finally, I would like to express my deepest gratitude to my family who have always been very supportive of all my decisions and provided me with immeasurable love and comedic relief, especially my parents, Donaciano and Irma Naranjo.

Unless otherwise noted, all photos are from the author.

# Table of Contents

1	Introduction.....	1
1.1	Motivation .....	1
1.2	Research Objective .....	1
1.3	Thesis Outline.....	2
2	Review of Literature .....	3
2.1	Definition of Relevant Parameters .....	3
2.2	Terramechanics Testing Techniques .....	4
2.3	Tire Instrumentation .....	7
3	Experimental Equipment and Instruments.....	10
3.1	Terramechanics Rig.....	10
3.2	Rig Upgrades and Modifications .....	13
3.2.1	Active Normal Load Control .....	13
3.2.1.1	Controls Strategy for Implementing Fluid Regulation.....	14
3.2.1.2	Fluid Control via Pressure Regulation.....	16
3.2.1.3	Fluid Control via Flow rate Regulation .....	18
3.2.2	Robust Motor Control.....	21
3.2.3	Automatic Offloading of Wheel Assembly .....	22
3.2.4	Rig – Driven Soil Compactor .....	23
3.2.5	Rigidized Leveling Blade .....	25
3.3	Soil Measurements .....	26
3.3.1	Real-time Soil Height Monitor .....	27
3.3.2	Cone Penetrometer.....	29
3.3.3	Soil Moisture Content.....	30
4	Development of a Tire Deflection Measurement System.....	31
4.1	Design Considerations .....	31
4.2	List of Materials.....	32
4.3	Familiarization of Electronics .....	35

4.3.1	Microcontroller .....	36
4.3.2	Distance Measuring Sensor.....	37
4.3.3	Proof of Concept Test .....	40
4.3.4	Sensor Selection Control Strategy .....	42
4.4	Sensor Rim Attachment Methods.....	43
4.4.1	Wheel Strap.....	43
4.4.2	Hook and Loop Fastener .....	44
4.4.3	Custom Mount .....	45
4.5	Quarter–Car Rig Validation Test.....	47
4.6	Wireless Implementation.....	51
4.6.1	Wireless Communication.....	51
4.6.2	Power Supply .....	52
4.7	Tire and Wheel Calibration .....	55
4.8	Final Design and WITS Capabilities .....	56
4.9	Determination of Tire Sinkage .....	59
5	Experimental Soil.....	61
5.1	Soil Retrieval .....	61
5.1.1	Rough Tire Sinkage Estimation .....	61
5.1.2	Amount of Soil Needed .....	64
5.2	Soil Preparation Procedure .....	65
5.3	Laboratory Testing .....	68
6	Design of Experiment .....	70
6.1.1	Test Tire .....	70
6.1.2	Soil Parameter Levels .....	72
6.1.3	Initial Design of Experiment.....	73
6.2	Experimental Procedure .....	73
6.3	Reflection of Initial DOE .....	76
6.3.1	Inconsistent Slip Change.....	76
6.3.2	Small and Large Impact of Parameters .....	78

6.4	Final DOE.....	80
7	Experimental Results and Discussion.....	81
7.1	Data Processing Method and Baseline Analysis .....	81
7.2	Comparative Analysis of One Parameter Change .....	84
7.3	Comparative Analysis of Several Parameter Changes .....	88
7.4	Review of all DOE Conditions.....	92
7.5	Main Effects and Interaction of Parameters .....	94
7.5.1	Parameter Effects on Drawbar Pull Response .....	94
7.5.2	Parameter Effects on Sinkage Response.....	97
7.6	Parameter Variation.....	98
8	Conclusions and Future Work .....	102
8.1	Recommendations .....	103
	References.....	105
	Appendices.....	108
	Appendix (A) Raw Data .....	109
	Appendix (B) Drawbar Pull Plots.....	111
	Appendix (C) Sinkage Plots.....	115
	Appendix (D) WITS Circuit Diagrams and Notes.....	119
	Appendix (E) Normal Load Controller Manual.....	124

## List of Tables

Table 3-1. Comparison of various USB-powered DAQ systems. ....	15
Table 3-2. Comparison of various control valves. ....	19
Table 4-1. Estimated cost of the originally purchased materials .....	35
Table 4-2. Sinusoidal wave properties applied as input by the Quartr-car rig. ....	49
Table 5-1. Terrain Profiles obtained from J. Y. Wong, <i>Theory of ground vehicles</i> , 4th ed. Hoboken, N.J.: Wiley, 2008. Used under fair use, 2013. ....	62
Table 5-2. Known tire parameters obtained from J. Y. Wong, <i>Theory of ground vehicles</i> , 4th ed. Hoboken, N.J.: Wiley, 2008. Used under fair use, 2013. ....	62
Table 5-3. Revised parameters for calculating tire sinkage of a deformable tire. ....	64
Table 5-4. Tire Sinkage results for a flexible wheel. ....	64
Table 5-5. Nuclear density (lb/ft <sup>3</sup> ) test results. ....	69
Table 6-1. Specifications of the instrumented Land Rover Defender 110. ....	71
Table 6-2. Initial design of experiment parameter matrix. ....	73
Table 6-3. Final design of experiment parameter matrix.....	80
Table A-1. All DOE Raw Data. ....	109

## List of Figures

Figure 2-1. Tire axis system from SAE, <i>Vehicle Dynamics Terminology: SAE J670e</i> : Global Info Centre Canada, 1978. Used under fair use, 2013.....	3
Figure 2-2. Comparing Programmed -Increasing and -Decreasing slip, Constant slip, and Constant Pull test results from N. R. M. a. A. J. Green, "Effects of Test Techniques on Wheel Performance," <i>Journal of Terramechanics</i> , vol. 6, pp. 37-52, 1969. Used under fair use, 2013. ....	5
Figure 3-1. Terramechanics rig fitted with a pneumatic wheel undergoing a rigid platform test. ....	10
Figure 3-2. Close front-view of the Terramechanics rig carriage and wheel assembly. ....	11
Figure 3-3. Front view of wheel assembly.....	12
Figure 3-4. Inconsistent Normal Load on a rigid surface test.....	14
Figure 3-5. Screenshot of the normal load control VI. ....	16
Figure 3-6. Normal load response to two separate step inputs. ....	17
Figure 3-7. Fluctuating wheel load of tire on soil moving forward then reverse. ....	18
Figure 3-8. M1d Valve Diagram (ISO 1219) from Enfield Technologies, "M1d Proportional Pneumatic Control Valve " <i>Datasheet</i> , pp. 1-2, 2010. Used under fair use, 2013. ....	19
Figure 3-9. Arrangement of new hoses and M1d valve controller. ....	20
Figure 3-10. Normal load of a rolling tire under active control at less than 3% variation. ....	20
Figure 3-11. PiCPro ladder logic program.....	21
Figure 3-12. Comparison of old and new rig handheld control box.....	22
Figure 3-13.[Left] Original Manual Winch. [Right] Electric Winch.....	23
Figure 3-14. Agricultural roller along with the original position of the electric winch.....	24
Figure 3-15. Two views of the new guide arms installed on the roller. ....	24
Figure 3-16. Mounts and pins used to attach roller guide arms to the rig. ....	25
Figure 3-17. (a) Detailed view of the modified blade. (b) Old configuration with linear bearings and clamps. (c) New configuration secured on rig carriage. ....	26
Figure 3-18. PING sensor and Arduino UNO fitted on the custom mount. ....	28
Figure 3-19. LabVIEW soil height monitor VI [left] and block diagram [right]. ....	28
Figure 3-20. Soil height monitor system mounted on the rig for testing .....	29
Figure 3-21. Microwave, weight scale and glasse vials of various sizes used for MC testing.....	30
Figure 4-1. SHARP GP2Y3A001K0F wide angle distance measuring sensor fitted to an early mount prototype. ....	33
Figure 4-2. Pictured on the left is the Arduino Mega, center is the data logging shield with an SD card, and on the right is the XBee shield fitted with an XBee series 1 RF module.....	34
Figure 4-3. Screenshot of the Arduino programming software. ....	36

Figure 4-4. Timing chart for proper use of the sensor from SHARP, "Wide angle Distance Measuring Sensor Unit," <i>GP2Y3A001K0F Datasheet</i> , 2006. Used under fair use, 2013. ....	38
Figure 4-5. Voltage output of a sensor measuring a moving surface while ignoring the timing schedule.....	39
Figure 4-6. Raw and filtered voltage output of an object moving in 1cm increments. ....	39
Figure 4-7. Original sensor wheel arrangement diagram.....	40
Figure 4-8. Proof of concept false wheel .....	41
Figure 4-9. Results from bouncing and rolling the false wheel, sensors A and B.....	41
Figure 4-10. Tire installation and instrumentation with an electro-pneumatic tire changer.....	44
Figure 4-11. Custom mount (left) and new fasteners (right). ....	45
Figure 4-12. Bead lock wheel fitted on to the manual tire changer. ....	46
Figure 4-13. PERL Quarter-car rig fitted with the rigid arm attachment and test tire. Photo courtesy of Anake Umsrithong.....	48
Figure 4-14. Deflection response of the tires sensor and Quarter-car rig to a step input.....	49
Figure 4-15. Deflection response of the tire sensor and Quarter-car rig to a 5mm sine wave at $\frac{1}{4}$ Hz. ....	50
Figure 4-16. Rigid arm attachment for the test tire on the Quarter-car rig. Photo courtesy of Anake Umsrithong. ....	50
Figure 4-17. Operator XBee and digital logic button circuit. ....	51
Figure 4-18. H-Bridge Relay circuit used to power the sensor system. ....	53
Figure 4-19. Battery pack and voltage regulator used to power the sensor system.....	54
Figure 4-20. XBee shield fitted with the tilt switch.....	54
Figure 4-21. Calibration test to determine the relative distance each sensor has to the wheel center and instrumented accelerometer. ....	56
Figure 4-22. Diagram of the final WITS arrangement inside the wheel. ....	57
Figure 4-23. WITS output from measuring the deflected tire radius in a test run of the DOE. ....	58
Figure 4-24. Main WITS circuit boards fully assembled in their final circuit design and connected to the accelerometer. ....	59
Figure 4-25. Diagram for sinkage measurements .....	59
Figure 5-1. Average ground pressure as a function of inflation pressure and normal load for the 11.0R16 XL tire, obtained from J. Y. Wong, <i>Theory of ground vehicles</i> , 4th ed. Hoboken, N.J.: Wiley, 2008. Used under fair use, 2013.....	63
Figure 5-2. Tiller used to loosen the soil. ....	66
Figure 5-3. Raking soil smooth.....	66
Figure 5-4. Cone penetrometer test results for a low level of compaction. ....	67

Figure 5-5. Cone penetrometer test results for a high level of compaction. ....	68
Figure 6-1. Michelin LT235/85R-16 LTX A/T 2 E test tire tread pattern.....	71
Figure 6-2. Test run of a 0-5% slip change with all parameters set to level one. Blue curve represents the measured longitudinal force. Green curve represents the speed of the wheel. ....	76
Figure 6-3. Comparisons of ideal and measured wheel angular velocity collected for three runs under the level 1 condition for all parameters.....	77
Figure 6-4. Angular rate comparison of a wheel crossing a 4 meter soil path while applying 8 slip changes (0-5-10-15-20-40-60-90%) with either a loaded or unloaded wheel. ....	77
Figure 6-5. Comparative plot of the normalized drawbar pull vs slip collected of two runs under the level 2 MC condition. Outliers are a result of separate days of testing. ....	78
Figure 6-6. Comprehensive plot displaying the impact of several parameter changes on the normalized drawbarpull response. ....	79
Figure 7-1. Drawbar pull response vs. slip for all level one parameters of the DOE.....	82
Figure 7-2. Test run of 4 low range slip changes displaying string pot, WITS, and soil height(PING) measurements.....	83
Figure 7-3. Sinkage measured for the DOE condition of all parameters held to level one. ....	84
Figure 7-4. DP coefficient vs slip response to individual parameters changes of the DOE. The black curve represents the level one condition for all parameters. The blue, red, and green curve represent the second level of inflation pressure, normal load and compaction resistance, respectively.....	85
Figure 7-5. DP coefficient vs slip response to individual parameters changes of the DOE, with the zero slip conditions shift to a zero DP coefficient response. The black curve represents the level one condition for all parameters. The blue, red, and green curve represent the second level of inflation pressure, normal load and compaction, respectively. ....	86
Figure 7-6. Wheel sinkage vs. slip response to individual parameters changes of the DOE. The black curve represents the level one condition for all parameters. The blue, magenta, and red curve represent the second level of compaction, normal load and inflation pressure, respectively.....	87
Figure 7-7. DP coefficient vs slip response to several parameters changes of the DOE. The black curve represents the level one condition for all parameters. The following second level parameter combinations and their representative color are: blue, for normal load and inflation pressure; green, for normal load and compaction; red, for inflation pressure and compaction; and magenta for all parameters at the second level. ....	88
Figure 7-8. DP coefficient vs slip response to several parameters changes of the DOE, with the zero slip conditions shift to a zero DP coefficient response. The black curve represents the level one condition for all parameters. The following second level parameter combinations and their	

representive color are: blue, normal load and inflation pressure; green, normal load and compaction; red, inflation pressure and compaction; and magenta for all parameters at the second level.....90

Figure 7-9. Wheel sinkage vs. slip response to several parameters changes of the DOE. The black curve represents the level one condition for all parameters. The following second level parameter combinations and their representative color are: blue, normal load and inflation pressure; green, inflation pressure and compaction resistance; red, normal load and compaction resistance; and magenta for all the parameters held to the second level. ....91

Figure 7-10. DP coefficient vs slip response to all the conditions of DOE. The black and orange curves represent all parameters set to level one and two, respectively. The individual parameter changes and their representative color are: blue, compaction (CR); green, normal load (Fz) ; and red, inflation pressure (TP). The following second level parameter combinations and their representative color are: magenta, Fz and TP; beige, Fz and CR; and gray, TP and CR.....92

Figure 7-11. Sinkage vs slip response to all the conditions of DOE. The black and orange curves represent all parameters set to level one and two, respectively. The individual parameter changes and their representative color are: blue, compaction (CR); green, normal load(Fz) ; red, inflation pressure (TP); purple, Fz and TP; beige, TP and CR; and gray, Fz and CR.....93

Figure 7-12. Main effects plot of the average peak drawbar pull coefficient.....94

Figure 7-13. Main effects plot of the average high slip drawbar pull coefficient. ....95

Figure 7-14. Interaction plot of the norma load, inflation pressure, and soil compaction paramter levels on the peak drawbar pull response. ....96

Figure 7-15. Interaction plot of the norma load, inflation pressure, and soil compaction paramter levels on the high slip drawbar pull response. ....96

Figure 7-16. Main effects plot of the overall average sinkage. ....97

Figure 7-17. Interaction plot of the normal load, inflation pressure, and soil compaction parameter levels on the sinkage response. ....98

Figure 7-18. Normal load variation for the level one condition of 5 kN.....99

Figure 7-19. Normal load variation for the level two condition of 6 kN.....99

Figure 7-20. Soil compaction variation measured with the CI gradient (kPa/mm) between all DOE conditions..... 100

Figure 7-21. Moisture content variation between each condition and run. .... 101

Figure B-1. DP of three runs of all parameters held at level 1; specifically 5 kN load, 29 psi inflation pressure, and 4.4 kPa/mm cone index gradient..... 111

Figure B-2. DP of three runs of soil compaction held to level 2; specifically 5 kN load, 29 psi inflation pressure, and 6.5 kPa/mm cone index gradient. .... 111

Figure B-3. DP of three runs of normal load held to level 2; specifically 6 kN load, 29 psi inflation pressure, and 4.4 kPa/mm cone index gradient.....	112
Figure B-4. DP of three runs of inflation pressure held to level 2, specifically 5 kN load, 20 psi inflation pressure, and 4.4 kPa/mm cone index gradient. ....	112
Figure B-5. DP of two runs of both normal load and inflation held at level 2, specifically 6 kN load, 20 psi inflation pressure, and 4.4 kPa/mm cone index gradient. ....	113
Figure B-6. DP of three runs of normal load and soil compaction held at level 2, specifically 6 kN load, 29 psi inflation pressure, and 6.5 kPa/mm cone index gradient. ....	113
Figure B-7. DP of two runs of both inflation pressure and soil compaction held at level 2, specifically 5 kN load, 20 psi inflation pressure, and 6.5 kPa/mm cone index gradient.....	114
Figure B-8. DP of two runs of all parameters held at level 2, specifically 6 kN load, 20 psi inflation pressure, and 6.5 kPa/mm cone index gradient.....	114
Figure C-1. Sinkage of three runs of all parameters held at level 1, specifically 5 kN load, 29 psi inflation pressure, and 4.4 kPa/mm cone index gradient. ....	115
Figure C-2. Sinkage of three runs of soil compaction held to level 2; specifically 5 kN load, 29 psi inflation pressure, and 6.5 kPa/mm cone index gradient. ....	115
Figure C-3. Sinkage of three runs of normal load held to level 2; specifically 6 kN load, 29 psi inflation pressure, and 4.4 kPa/mm cone index gradient. ....	116
Figure C-4. Sinkage of three runs of inflation pressure held to level 2, specifically 5 kN load, 20 psi inflation pressure, and 4.4 kPa/mm cone index gradient. ....	116
Figure C-5. Sinkage of two runs of both normal load and inflation held at level 2, specifically 6 kN load, 20 psi inflation pressure, and 4.4 kPa/mm cone index gradient. ....	117
Figure C-6. Sinkage of three runs of normal load and soil compaction held at level 2, specifically 6 kN load, 29 psi in-flation pressure, and 6.5 kPa/mm cone index gradient. ....	117
Figure C-7. Sinkage of two runs of both inflation pressure and soil compaction held at level 2, specifically 5 kN load, 20 psi inflation pressure, and 6.5 kPa/mm cone index gradient. ....	118
Figure C-8. Sinkage of two runs of all parameters held at level 2, specifically 6 kN load, 20 psi inflation pressure, and 6.5 kPa/mm cone index gradient. ....	118
Figure D-1. Wire harness for all sensors to connect to the microcontroller. ....	119
Figure D-2. H-bridge circuit that controls the relay that supplies power to the microcontroller .....	119
Figure D-3. Accelerometer to microcontroller connection, made directly to the SD logger shield rather than the microcontroller itself.....	120
Figure D-4. Operator XBee circuit to communicate with the microcontroller.....	121
Figure D-5. XBee to microcontroller connection. Digital signals are passed from the operator. ....	121
Figure D-6. DC to DC converter circuit used to provide a clean 5 V power to the WITS system....	122

Figure D-7. Several batteries in series and parallel provide a 9 V voltage battery power supply for the DC-DC converter circuit used to power the WITS system.....	122
Figure D-8. Battery pack for the tilt switch used to trigger the WITS system to power on when disconnected from its own power supply.....	123
Figure E-1. LabVIEW VI used for normal load control.....	124
Figure E-2. Voltage supply for the electro-pneumatic control valve.....	124
Figure E-3. Manual regulator and filter for the inlet supply air of the electro-pneumatic control valve. .....	125

# **1 Introduction**

This section will provide the motivation and research objective for this work. Furthermore, it will also outline the chapter structure of this thesis.

## ***1.1 Motivation***

Among the many components that form a vehicle, arguably the most important is the tire; as this quite literally provides the foundation of the vehicle's stability and tractive performance. Understanding the interaction between a tire and the underlying ground is imperative to tire design and vehicle mobility. The complexity of this interaction varies significantly from being fairly simple on a hard, smooth surface, like in common roads, to great difficulty such as on deformable soft soils. For this reason, countless research efforts have been made to construct models that predict a tire's performance. Despite the physical accuracy of tire models, supplemental experimental work is vital to the design and validation of a tire model's performance in capturing all factors of interest. Therefore this thesis takes on the challenge of collecting experimental data for a tire performing in a soft soil environment and investigates the effects of several tire and soil parameters.

## ***1.2 Research Objective***

The primary objective of this work is to study the interaction of an off-road tire in a controlled soft soil environment. Moreover, the results of this work will be used to validate and provide input for a developing soft soil tire model at Virginia Tech [1]. This research effort investigates several key factors that influence tire mechanics and the structural integrity of the soil upon which the tire acts on. The factors investigated specifically are longitudinal wheel slip, normal load, inflation pressure and soil compaction. To make this research challenge possible, the following tasks were performed:

- Improvement of a single-wheel test rig to accommodate testing heavy wheel loads on a soft soil.
- Employment of an efficient and repeatable method of preparing a soft soil test path.
- Application of a new instrumentation method to measure phenomena special to soft soil environments.

### **1.3 Thesis Outline**

Chapter 2 presents the literature review done throughout the span of this study. It begins with defining relevant parameters that will be discussed over the course of the document. Several experiments concerning indoor and outdoor tire-soil testing are discussed. Moreover, the advancements in tire instrumentation will be presented.

Chapter 3 goes over the experimental equipment and instruments that were acquired and modified to accurately address the experimental needs of this study.

Chapter 4 presents the design, development, and validation of an instrumented tire sensor system termed Wireless Internal Tire Sensors (WITS).

Chapter 5 discusses the experimental soil used in this study, the procedure followed to prepare soil for test conditions, and contracted laboratory test work.

Chapter 6 outlines the process followed to obtain the design of experiment used in this study.

Chapter 7 discusses the experimental procedure followed to attain the presented results of the study. Parameter effects and interactions within the drawbar pull and sinkage response will be thoroughly discussed.

Chapter 8 outlines the main conclusions of the study and recommendations for future work related to the terramechanics rig and the WITS system.

The appendix provides the main raw data used in the analysis, extra plots, circuit diagrams and notes for the WITS system, and manual to operate a normal load controller.

## 2 Review of Literature

This section will detail the comprehensive literature review done for this project in order to understand what has been done, the challenges, and what improvements can be made. The section will define the relevant parameters of the study and explore the work done in off-road tire testing and in tire instrumentation.

### 2.1 Definition of Relevant Parameters

For clarification purposes, this section will provide the definitions of parameters and common vehicle dynamics terminology that will be used throughout this thesis. For reference, understanding tire mechanics requires following a common axis system, such as that defined by the Society of Automotive Engineers (SAE), shown in Figure 2-1 [2].

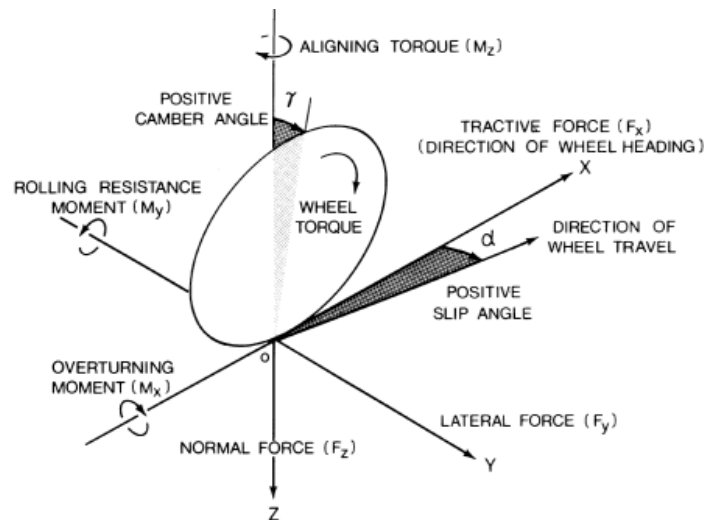


**Figure 2-1. Tire axis system from SAE, *Vehicle Dynamics Terminology: SAE J670e*: Global Info Centre Canada, 1978. Used under fair use, 2013.**

In Figure 2-1, the origin of the axis system is the center point at which the tire contacts the ground. From this center point, three forces and moments along all axes are caused by the tire and ground interaction. Along the X axis, in the direction of the wheel heading (noted as positive) is the resultant X component force between the tire and ground known as the tractive or longitudinal force,  $F_x$ ; upon this axis acts the overturning moment  $M_x$ . The resultant Y component force, known as the lateral force,  $F_y$ , points in the positive direction, outward from the wheel torque causing the wheel to rotate; upon this axis acts the rolling resistance moment,  $M_y$ . The resultant Z component force, known as the normal force,  $F_z$ , points downward in the positive direction of gravity; upon this axis acts the aligning torque,  $M_z$ . Between the XZ plane and the wheel plane is the camber angle,  $\gamma$ , and within the XY plane between the directions of wheel heading and wheel travel is the slip angle,  $\alpha$ .

A principal design factor for most off-road vehicles is the tractive capability to push or pull various weights which is known as the drawbar pull.

$$DP = F - \Sigma R \quad (1.1)$$

The drawbar pull is the difference between the tractor effort  $F$ , caused by the running gear of the vehicle, and the resultant resistive forces  $\Sigma R$  acting against the vehicle[3].

Due to various operating conditions such as tire and ground properties, normal load, etc., as the vehicle applies torque at the wheels to achieve traction, the intended rotational speed of the tire will not always meet the resulting speed, thus inducing what is known as longitudinal slip on the tire.

$$s_d = \left(1 - \frac{V}{r_e \omega}\right) \times 100\% \quad (1.2)$$

Where  $V$  is the translational speed of the wheel center,  $r_e$  is the effective radius of the wheel, and  $\omega$  is the angular velocity of the wheel. Although various types of slip exist in tire mechanics, such as lateral slip, combined slip, and slip angle, unless otherwise stated, this thesis will reference the term longitudinal slip as slip or slip ratio. Note that the effective radius, or rolling radius, is greater than the height of a loaded wheel ( $r_H$ ), yet lower than the geometric or unloaded radius ( $r_U$ ) of a wheel. The effective radius of a wheel is mainly dependent on tire structure, composition, load conditions, inflation pressure, and longitudinal velocity of the wheel [4].

As a ground vehicle applies normal load to propel itself over a terrain surface, the vehicle experiences sinkage,  $z$ , giving rise to motion resistance[3]. This is known as the depth that the tire contact patch descends from the surface level of the undisturbed soil.

To assess vehicle mobility in the field, the Waterways Experiment Station (WES) of the U.S. Army Corps of Engineers, developed a cone penetrometer technique to establish the parameter known as the Cone Index ( $CI$ ). The  $CI$  represents the resistance to penetration into a terrain per unit of a known cone base surface area, representing the combined shear and compressive characteristics of a terrain [5]. Both cone index and its gradient with respect to the cone's penetration depth are commonly used in off-road vehicle studies.

## ***2.2 Terramechanics Testing Techniques***

In experimental work related to terramechanics, specifically tire testing, many different approaches have been taken to investigate and model traction performance affected by several tire properties, terrain, and operational conditions. Confirmed test methods of researchers, past and present, can be learned and adapted to insure proper techniques are applied to the work of this thesis. Although the work done for this document revolves around the use of a single wheel tester (SWT), studies done on both SWTs and instrumented vehicles are reviewed for not only their test methodologies, but also their consideration and measurement of terrain conditions. Historically, each approach

has its own benefits and drawbacks; for example, on a SWT all effects of vehicle dynamics are ruled out, such as load transfer, suspension response, etc., to focus primarily on tire performance. Although this may not be a realistic representation of the real world wheel-terrain interaction, SWTs do allow great control of various test metrics to attain repeatable results in a timely manner, compared to instrumented vehicles, thus allowing a more thorough evaluation of the wheel-terrain interface for model development and validation.

Looking far back in the 1960's, Green and Murphy at WES noticed the trend in differences between SWTs and instrumented vehicles, primarily in the [drawbar] pull –slip relation, and decided to investigate the effects of test techniques on tire-soil relations [6]. In that study, the effect of starting conditions, comparability of programmed (both increasing and decreasing) and constant slip results, and the comparability of controlled slip and controlled pull test results were evaluated for a military tire on air-dry sand. Testing between different starting conditions: (1) non-yielding surface, (2) resting on the soil, and (3) embedded in the soil (approximately 10-11 inches) were compared; Green and Murphy found that once the desired slip was attained, the wheel performed the same no matter the starting conditions. Woodward performed a similar study to this test and confirmed the same results [7].

Investigating programmed slip alone, whether a run is decreasing or increasing slip made an interesting difference in the pull-slip and torque-slip curves up until  $\pm 10$  to  $\pm 15$  percent slip. In the low range slip, the programmed decreasing slip resulted in a slightly higher pull and torque; meanwhile, the programmed increasing slip runs resulted in a slightly lower pull and torque relation. Comparing the programmed-slip to constant-slip resulted in the pull and torque slip curve to lie in the middle of the programmed-slip results, as shown in Figure 2-2.

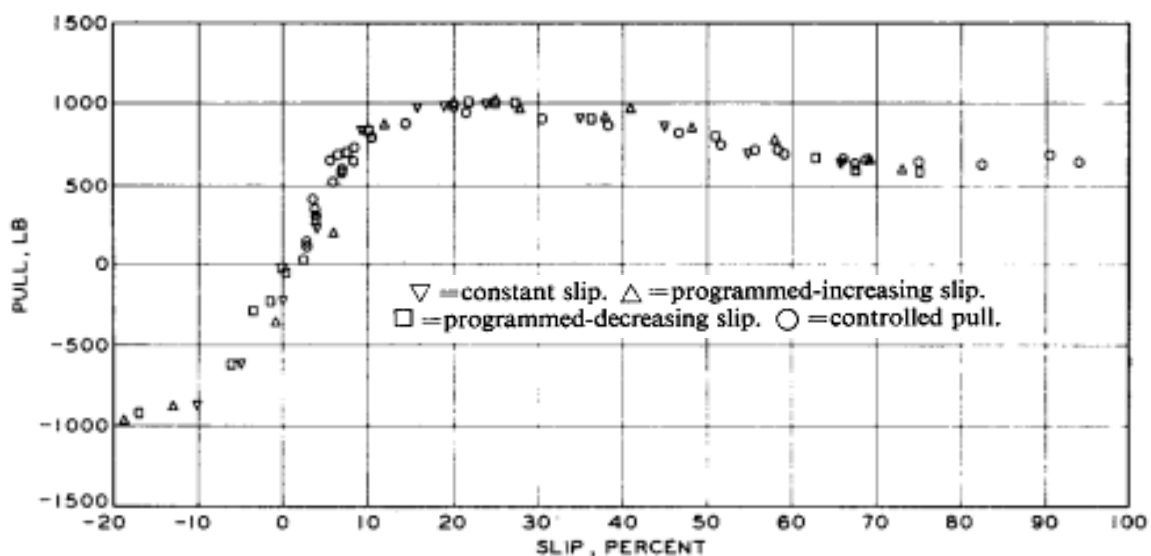


**Figure 2-2. Comparing Programmed -Increasing and -Decreasing slip, Constant slip, and Constant Pull test results from N. R. M. a. A. J. Green, "Effects of Test Techniques on Wheel Performance," *Journal of Terramechanics*, vol. 6, pp. 37-52, 1969. Used under fair use, 2013.**

Controlled-pull tests are also reflected in Figure 2-2; although the results are the same as the tests done with programmed or constant slip, Green and Murphy found that processing the constant-pull data was more involved and the results were not as consistent. The constant pull tests were administered by disengaging the system to apply constant longitudinal velocity to the SWT and allowing an external force to maintain the desired constant velocity, or slip. This method of testing proved difficult for higher drawbar pull tests where desired velocities could not be kept constant, thus inducing variation in the pull-slip data. Comparing the results of the transducer used to measure drawbar pull on a constant-slip test and the transducer used to measure the applied drawbar pull from an external load, the probable source of difference between SWTs and instrument became evident [6]. Without taking inertial forces between the SWT and source of the external load along with parts of the frictional forces that the test wheel must overcome, the pull-slip relation will appear to increase with slip rather than decrease, as in Figure 2-2.

Woodward [7] performed a more recent and similar study for a lunar rover vehicle on a lunar soil simulant in order to develop a repeatable drawbar pull test procedure. Once active control was set on the mechanism applying the external drawbar pull to the test vehicle, Woodward found that as little as 1.64 ft. (0.5 m) of wheel travel was sufficient to provide data representative of common drawbar pull-slip relations. Similar to the findings of WES, several starting positions of the test tire were compared and found to have no effect on the tire performance.

Common parameters of interests in tire-soil interaction tests are normal load, inflation pressure, vehicle speed, and soil compaction. Šmerda and Čupera [8] investigated the influence of tire inflation on tractive characteristics of a ploughing set. Two tire sets of different tire pressures were tested in field conditions, revealing that reduced tire inflation improved the drawbar characteristics. Raper et. al [9] investigated the effects of lower inflation pressures on the soil-tire interface pressures by measuring the stresses on the lugs of a 18.4-R38 R-1 radial tire. The results showed that as the inflation pressure increased, the soil-tire interface stresses near the center of the tire would increase as well; however, the stresses near the edge of the tire did not change. The increased stresses were observed to further compact the soil.

Park and Lee [10] studied the effect of dynamic load, inflation pressure and number of passes of a tire on soil compaction. The tests were performed on a 6.00R14 radial-ply tire in a sandy loam soil bin where the tire sinkage, density and volume of the traversed soil were measured. Park and Lee observed that all tested parameters increased sinkage and soil compaction yet no parameter was comparatively effective as the dynamic load. The effect of the parameters, however, decreased as the soil sample depth increased.

Pytka [11] performed field experiments on off-road vehicle traction and wheel-soil interactions and found that reduced inflation pressure had positive effects on traction and increased soil stress at the contact patch. Drawbar pull was found to increase with increasing wheel load. The soil surface was observed to deform in mainly the vertical and longitudinal directions; where vertical deformations were affected by wheel loading and longitudinal deformations were affected by inflation pressure. These measurements and observations were made possible with an array of pressure sensors and videogrammetry.

In all tire-soil interaction studies, great consideration was put into the soil conditioning to maintain repetitive conditions, whether done by hand [7, 11, 12] or with purpose-built equipment. In the development of an indoor SWT for agricultural tires, Kawase et. al [13] developed a device with a tiller in the front with a motor-driven roller in the rear; this would mix, flatten, and compact the soil with one pass.

In the design of the soil bin-SWT facility to study soil -tool and -tire interaction [14], soil conditioning begins with the loosening of the soil with a cultivator connected to the soil bin overhead carriage, then leveling it with a smaller carriage leveler, then compacted with a variable weight roller compactor. The soil strength in the bin is set by controlling the compactor speed, weight, and number of runs. Similarly, a soil processing trolley is used at the Indian Institute of Technology [15] for soil preparation. This trolley consists of a rotary tiller, a leveler blade, and a compacting roller, which is driven along the length of a soil bin with its own drive system.

In review of experimental studies done in the tire-soil testing, a common trend is seen with many wheel parameters such as wheel slip, normal load, and inflation pressure, and their impact on drawbar pull and sinkage. Soil compaction effects are noted as well. Moreover, great emphasis within each study begins with a methodological process of conditioning the soil before a test run.

### ***2.3 Tire Instrumentation***

The tire is a very fundamental aspect of vehicle dynamics, as it is the medium between the vehicle and terrain, which experiences all the forces acting on the vehicle from the terrain and applies driving and steering torque to maintain maneuverability of the vehicle. However, despite this importance, many features of tire behavior are poorly understood. Instrumenting a tire to monitor how it performs under various conditions can help in better understanding of tire performance so that tire model development can hold more realistic results and overall tire design in future products can be improved.

In particular to this study, understanding tire deformation in a soft soil can aid in measuring the wheel sinkage, as it is difficult to visually observe sinkage depth, in real time, and determine how the rut of the soil differs from the actual wheel sinkage. For soil applications and countless others related

to vehicle dynamics, tire instrumentation has been growing and improving with advancements in technology. As a great portion of this study focuses on tire instrumentation, understanding what has been done and what technologies yield the best results are imperative to great tire instrument development.

Various sensor technologies have been used in the past to collect different types of data such as the following:

- Pressure monitoring
- Tread deformation
- Carcass deflection
- Estimation of tire-road friction
- Estimate of tire forces
- Estimation of slip angle and slip ratio
- General tire health, etc.

Early developments, such as the Darmstadt Tire Sensor system, was made to measure tread displacement to eventually estimate friction forces between a road and tire [16, 17]. The measurement approach taken in that study was to embed a permanent magnet in the tire tread and monitor position and deformation with a position sensor using various voltage differentials obtained between crosses of the Hall Effect.

Magori et al. installed an ultrasonic sensor inside a tire to determine wheel load and vertical deflection of the tire [18]. The sensor was attached to the rim inside the wheel and was continuously measuring the deflection of the tire carcass. Aside from deflection measurements, tire temperature and tire-road contact parameters were also claimed to be extracted from the sensor signal.

Erdogran et al. utilized a wireless piezoelectric sensor system to measure tire carcass deformation to estimate both slip angle and tire-road friction coefficient [19, 20]. The unique design of the system allowed decoupling of the lateral carcass deformation from the radial and tangential deformations to provide accurate estimates of the slip angle.

Pohl et.al applied a tread element deformation method of using passive surface acoustic wave (SAW) devices to measure tread element deformation [21]. A SAW is an acoustic wave resulting from the elasticity of a material. As a wave prorogates from a point, it travels along the surface of the material in all directions while decaying exponentially into the depth of material; SAW devices utilize interdigital transducers (IDT) settled on the surface of a piezoelectric substrate to measure this wave.

Palmer et al. embedded fiber optic technology to monitor tire strain and measure the onset of skid [22] based on its estimation of low friction conditions. Along with being able to measure tread

strain, it also monitored inflation pressure and temperature to aid in conditions estimation and overall health of the tire.

Tuononen attached a Light Emitting Diode (LED) to the tire carcass to be measured by an optical sensor attached to the wheel [23-25]. A lens is used to focus the infrared light of the LED into a Position Sensitive Detector (PSD) to measure the three-dimensional movement of the LED and provide comprehensive information of the tire carcass deformation. This system was shown to estimate tire forces, aquaplaning, and vehicle slip angle [23, 26]. Tuononen also applied a laser triangulation method to measure tire carcass deflection [27].

Yi and Tseng, used a polyvinylidene fluoride (PVDF) based sensor to embed on the inner tread surface of a tire to measure tread deformation for estimation of tire-road interaction for wheeled robots and vehicles [28].

Matsuzaki et al. has worked on various types of strain sensors, such as a patch-like sensor composed of flexible polyimide substrates and epoxy resin, to reduce sensor stiffness and elongate it to cover a large length within a tire carcass[29]. A rubber-based strain sensor was also made with photolithography to mimic the mechanical properties of a tire so as to not interfere with tire deflection and monitor its status with changes in sensor capacitance [30]. The tire itself was used as a sensor by placing the tire steel wire structure in a parallel circuit of a capacitor and resistor [31, 32].

Additionally, several automotive and electronic industries have developed simple tire pressure monitoring systems (TPMS) to monitor tire inflation and alert the vehicle operator of low pressure. Among the various designs that exist for TPMS, the most common either have the sensor mounted on a rim with a stainless steel strap or are attached to the tire air valve. These systems are design to be very lightweight, power efficient, and wireless.

In summary, the tire sensor technologies investigated had common challenges, which were: to avoid disturbing the natural tire stiffness, packaging the instrumented into a small size, data transmission, and power management. Many approaches chose to embed a sensor or other materials in the tire, which can obtain good deformation data, but can also affect the natural deformation of the tire and are difficult to adhere to the tire due to the flexible rubber composition. Depending on the type of tire, such as one used for agricultural or common passenger vehicle purposes, there is a size constraint when instrumenting inside the tire. Because of the rotational nature of a tire, using wires to collect data from a sensor can be difficult. So many approaches have gone completely wireless or used slip rings, which often have speed limitations. Lastly, most sensors require some power to be able to take measurements, so similar to the data transmission challenging, various forms of powering a tire sensor system, whether it be wired or battery operated, are explored. All of these issues were considered for the tire sensor system developed in this study.

### 3 Experimental Equipment and Instruments

This section will go over the experimental equipment that was acquired at the start of this study, along with the additional equipment and improvements that were deemed necessary to ensure consistent experimental practice, provide accurate data collection, and reduce operator error.

#### 3.1 Terramechanics Rig

The primary test platform of this study was the AVDL Terramechanics rig. This single wheel tester was mainly designed and near-fully assembled by Biggans in 2007 [33]. The test rig was developed to investigate wheel interaction with various terrains under a well-controlled environment, essentially the terramechanics of a loaded wheel. The rig is primarily composed of four major components and will be referenced as the following: 1) soil vane 2) carriage 3) wheel assembly and 4) the two independent drivetrains. A few of these components are shown in Figure 3-1; the carriage in the image is located in the “Home” position of the soil vane and the opposing extreme is termed the “Away” position.

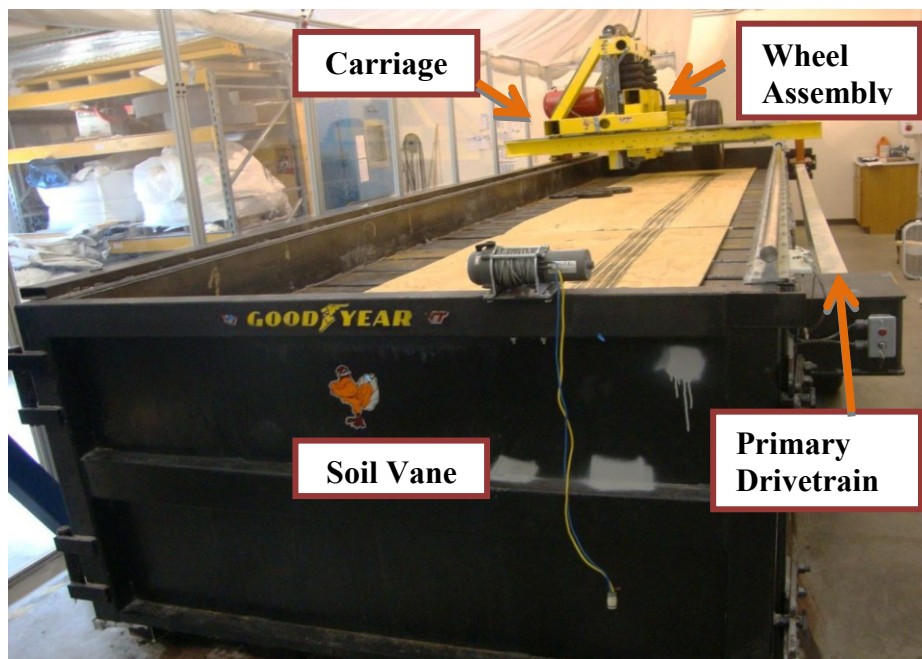


**Figure 3-1. Terramechanics rig fitted with a pneumatic wheel undergoing a rigid platform test.**

The soil vane was designed to provide a solid steel foundation to house various terrains ranging from sand to ice. The soil vane’s absolute horizontal area was 25 ft. (long) X 6 ft. (wide) and could vary in total volume depending on any of the three capable height configurations ranging from

3.5 ft. to as little as 10 inches. The change in height is made possible with the 25 steel U-channels that are used to form the rigid test surface. Opposing L-shaped brackets along the interior soil vane wall allow the U-channels to be arranged in two different height levels or removed completely to expose the total height of the soil vane.

The top portion of the soil vane yields the guide rails used by the carriage to follow when in motion and holds the primary drive train that actuates the longitudinal motion of the carriage. The motion is induced by a DC synchronous servomotor which drives a gear box and a pair of drive shafts which ultimately drives the dual belt pulley system shown in Figure 3-1. The carriage, wheel assembly, and their respective directions of travel can be more easily depicted in Figure 3-2.

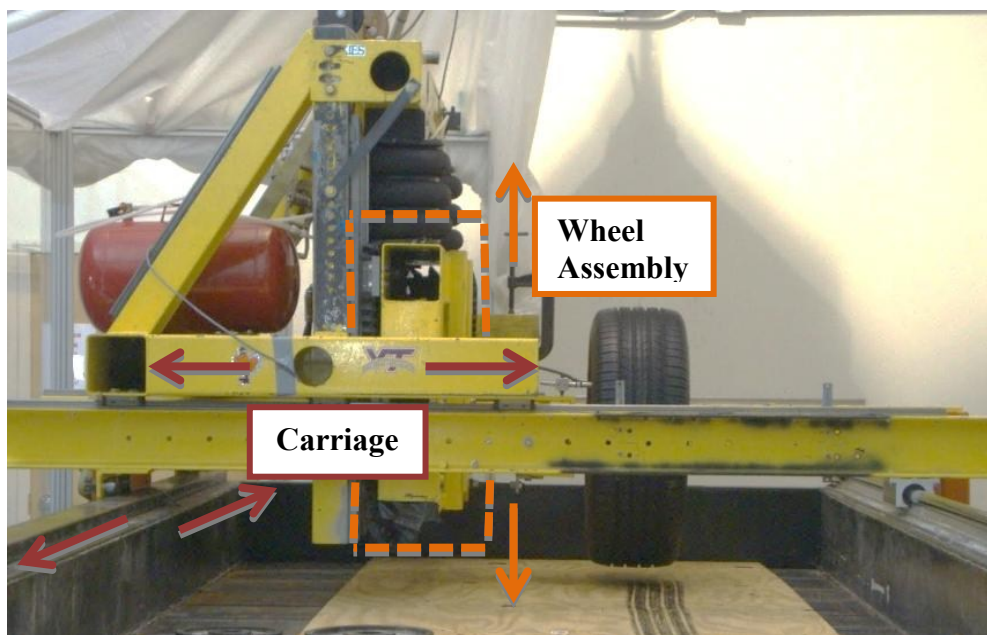


**Figure 3-2. Close front-view of the Terramechanics rig carriage and wheel assembly.**

The carriage of the rig is what essentially mimics a rigid, quarter-car model of a vehicle. The carriage is capable of moving along the length of the soil vane via the primary drivetrain and can be manually moved along the width of the soil vane. The wheel assembly is attached to the carriage via two linear rails which constrains the wheel assembly to only move in a vertical direction. This one-directional constraint allows the carriage to apply a normal load to the wheel assembly via two pneumatic air springs. The vertical displacement of the wheel assembly is measured via a string potentiometer.

The wheel assembly of the rig is what carries the secondary drivetrain, the test wheel and the primary source of measurement which is the Kistler P650 wheel hub sensor. The secondary drivetrain consists of a similar servomotor as previously mentioned and is connected to a reduction gearbox, followed by a custom hub adapter, and then finally the Kistler wheel hub sensor. The

Kistler sensor utilizes piezoelectric technology among four load cells to measure all forces and moments caused by the wheel-terrain interaction. Test wheels are attached to the wheel hub sensor via the interchangeable universal adapter, which currently can accept three different 6-bolt configurations. The wheel assembly also has the capability to test up to 8 degrees of camber and a toe of 45 degrees; however, for this study both parameters were held rigid at a neutral zero degree angle. The wheel assembly is shown more closely in Figure 3-3.

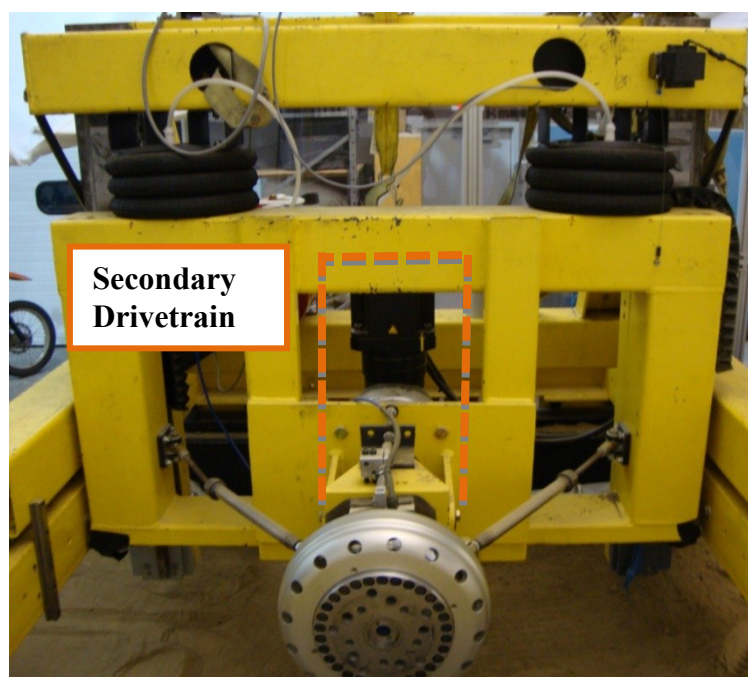


**Figure 3-3. Front view of wheel assembly.**

The Kistler sensor and string potentiometer data are all eventually sent to the LMS SCADAS III data acquisition system and managed by the LMS Test.Lab 8b software on the main Terramechanics rig computer. The SCADAS III has a modular design with several slots that can accept various module types, which for the needs of the rig, are analog input channels. Data from the Kistler sensor go through processing in the Kistler System 2000 On-Board electronics box before being read by the SCADAS III system. A master-slave configuration controls the two drivetrains; this setup is controlled by the PiCPro MMC Limited Edition software which operates in the ladder logic programming language. Information concerning the operation of the rig for beginning and ending a testing session can be found in the appendix of Taylor's thesis [12].

In general, the Terramechanics rig was designed to simulate the parameters of a small passenger vehicle up to a large HMMWV [33]. Thus the load can be set to a wide range with the test wheel diameter varying from 24 inches in diameter to 37 inches. Because of the relatively small enclosed space, the rig was built to run at a max speed of 2 mph. Moreover, recall that the rig runs on

two separate drivetrains; this allows careful control of both motor speeds which can be manipulated to induce longitudinal wheel slip as needed, assuming that the effective rolling radius of the wheel is known. Having this capability allows for the research of tire performance parameters of interest relationship with varying slip.

## **3.2 *Rig Upgrades and Modifications***

Since the initial development of the rig, several modifications were made to get it ready for testing and to cater to the needs of the individual studies performed on the rig. Taylor assembled and finalized motor control and data acquisition of the rig; he then performed his study on wheel parameter effects of a lunar rover wheel in a GRC-1 lunar soil simulant [12]. Taylor's work required a far lighter wheel load than what the rig was originally designed for, so an off-weight system was added to the rig to perform his tests. The carriage, however, continually had issues with maintaining a constant normal load due to wheel sinkage and the passive method of applying a normal load. The second set of testing performed on the rig was administered by Holley on his study of tire traction on ice [34]. This study added higher load capabilities to the rig with the addition of two large, triple-convoluted air springs and confirmed its capability of performing experiments on ice. Holley's work also exposed the weakness in the linkages used to change wheel toe and camber, thus temporarily making these parameters rigid until a new design is implemented. Both studies exposed flaws of the rig that required attention; of which, some of the flaws were addressed in order to ensure accurate and repeatable test results for the work of this document.

### **3.2.1 Active Normal Load Control**

Once preliminary testing began for this study to get familiar with the equipment and plan ahead for future testing, it was very evident that the inconsistent normal load problem had to be addressed. Experimenting on a rigid surface made out of plywood that was embedded within the U-channels (to smooth out the surface between the channels) showed odd variation in the normal load as shown in Figure 3-4. This experiment also highlighted the inefficient, exhausting and large time commitment required to achieve a desired normal load before a test run.

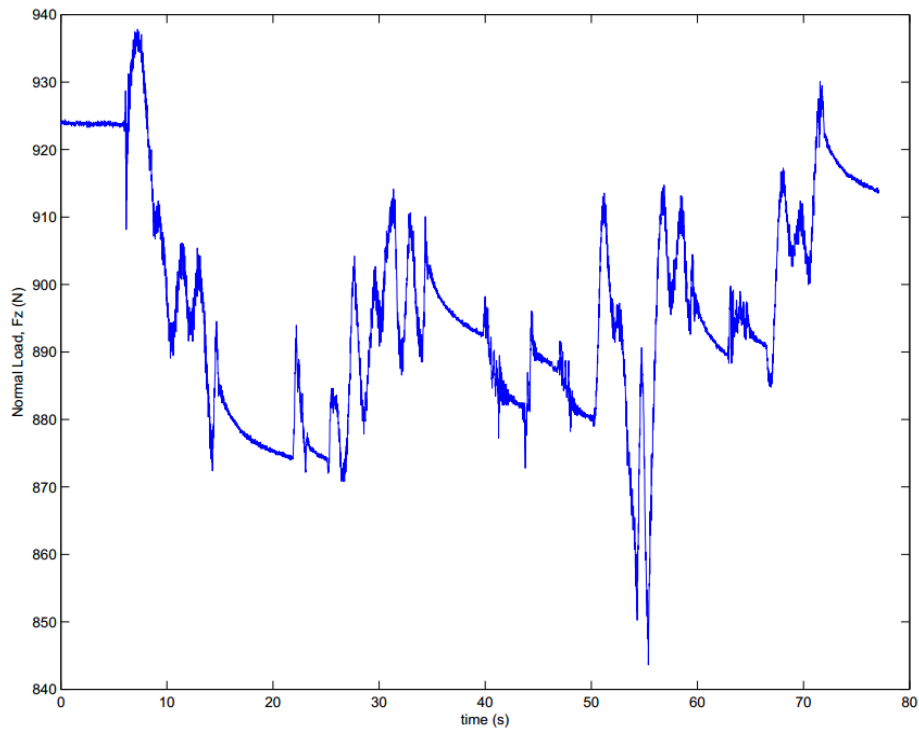


**Figure 3-4. Inconsistent Normal Load on a rigid surface test.**

Viewing this amount of variation on a flat surface was surprising so it was expected that running a similar test on a deformable soil was going to be far worse; therefore, great efforts were put into implementing an active control system for applying normal load. Applying load via pneumatic air springs offers a wide range of load capabilities with the use of minimal and lightweight equipment; thus, the main goal was to find a method of regulating the fluid in the air springs to maintain a constant load.

The Portable Tire Test Rig developed by the Intelligent Transportation Laboratory (ITL) of CVeSS is a good example of applying fluid regulation to maintain a constant normal load on a tire [35]. The Portable Tire Test Rig is essentially an instrumented test trailer that is towed by a vehicle to give a free-rolling test tire a constant longitudinal velocity. The test trailer collects data with a six-axis wheel hub sensor and has active normal load and steering angle control among other features. The test trailer utilizes a pressure regulator and an electronic pressure transducer to control the nitrogen gas in the single air spring used to apply a normal load. Thus the approach of employing an electronic pressure regulator on the Terramechanics rig load control apparatus was investigated.

### **3.2.1.1 Controls Strategy for Implementing Fluid Regulation**

While selecting the appropriate fluid regulation tool to use for normal load control, it was equally important to find the hardware and software needed to perform the control strategy of the normal load controller. The overall control strategy is to use the measured vertical force of the Kistler sensor as an input, manipulate the signal with appropriate gains, and determine the output

signal required for an actuator (e.g. , pressure regulator) to meet the normal load demands; thus for simplicity, a Proportional-Integral (PI) control system was utilized. To employ a PI controller, it was imperative to find capable equipment to handle the demands of the developing normal load control strategy. Naturally, the first approach was to use components that were already compatible with the rig’s LMS hardware; however, after contacting LMS there were no good output signal modules that would fit the project needs and the software was far from intuitive.

A low-cost and effective hardware and software bundle that could meet the needs of the control strategy turned out to be produced by National Instruments (NI). NI was primarily chosen for the relatively simple graphical programming language used in its software program, LabVIEW; moreover, LabVIEW offers near seamless integration with hardware, whether it is an NI product or not. From the hardware standpoint, all that was required was an analog input and output with a relatively high sample rate, so budget-friendly USB-powered products of NI and Measurement Computing (MCC) were compared, as shown in Table 3-1.

**Table 3-1. Comparison of various USB-powered DAQ systems.**

Co.	Product	Analog In Ch.	Res. In [bit]	Sample Rate	Analog Out Ch.	Res. Out [bit]	Update Rate	Digital I/O Ch.	Price
NI	M Series, 6211	16	16	250 kS/s	2	16	250 kS/s	4	\$ 849
	M Series, 6212	16	16	400 kS/s	2	16	250 kS/s	32	\$ 1,079
	X Series, 6341	16	16	500 kS/s	2	16	900 kS/s	24	\$ 1,188
MCC	1208HS-2AO	8	13	1 MS/s	2	12	1 MS/s	16	\$ 599
	2408-2AO	16	24	1 kS/s	2	16	2@500 S/s, 1@1 kS/s	8	\$ 699
	1608GX-2AO	16	16	500 kS/s	2	16	2@250 kS/s, 1@500kS/s	8	\$ 799
	1608HS-2AO	8	16	250 kS/s per ch.	2	16	2@35 kS/s, 1@70kS/s	16	\$ 1,399

The M Series USB-6211 was selected as the best choice due to its numerous available features and comparatively greater software support in LabVIEW. Once the 6211 was purchased, it was easier to start developing a LabVIEW program that would eventually serve as the Graphical User Interface (GUI) for the normal load controller. The basic format of LabVIEW is that the programmer works with two separate windows to make the final Virtual Interface (VI). The VI is the window that the operator would use to interact with the program and view plots or diagrams that are being generated, essentially a GUI. The second window is known as the block diagram which uses various

blocks, known as sub VIs, that perform certain tasks and are all “wired” to each other to carry out the main task of the program. The final VI developed would essentially run the PI control strategy while showing the real-time performance; moreover, the VI gives the operator the choice of changing settings of the controller and choice of collecting data into a Technical Data Management Solution (TDMS) file format for data post-processing. The TDMS format was utilized for its ease-of-use and superb organization of large arrays of datasets. Saving data on LabVIEW during the development stage of the controller allowed faster data processing to improve the PI control performance as opposed to collecting data from LMS. Figure 3-5 shows a screenshot of the latest version of the load control VI.

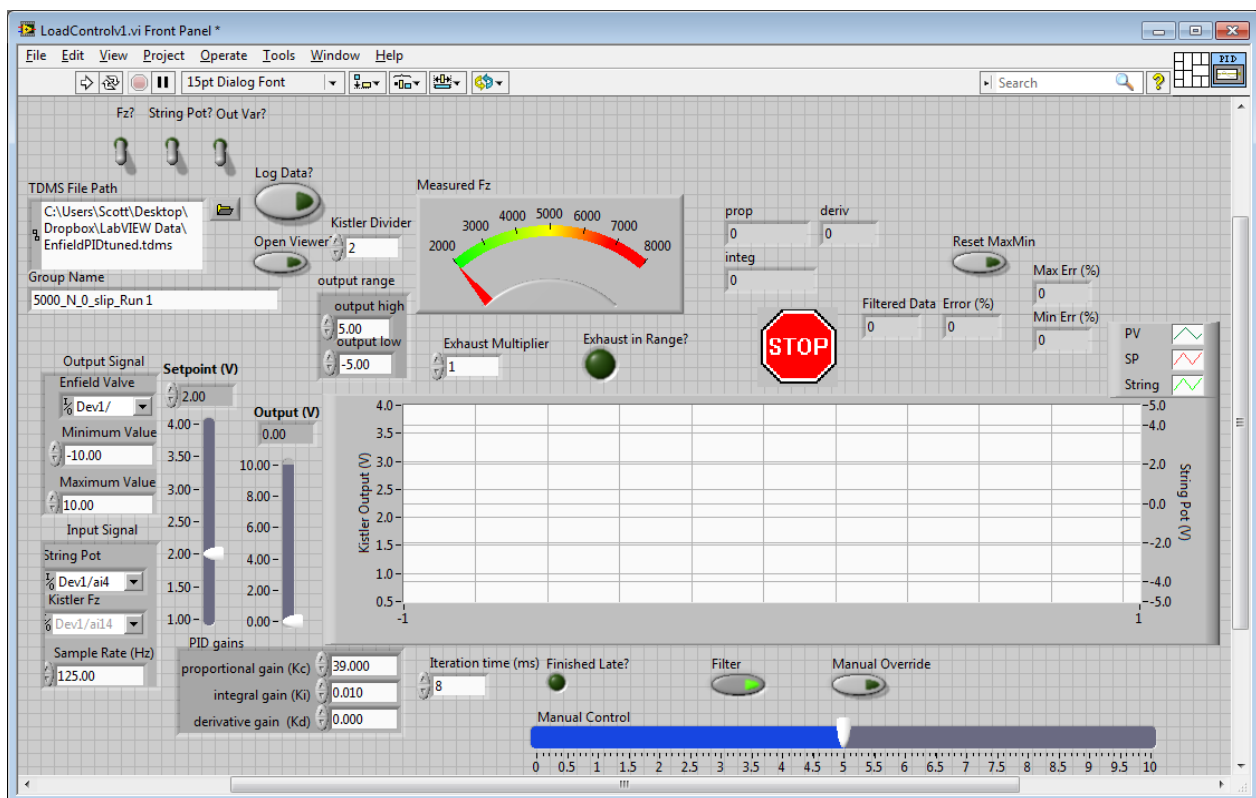


Figure 3-5. Screenshot of the normal load control VI.

### 3.2.1.2 Fluid Control via Pressure Regulation

The main criteria for selecting a pressure regulator are as follows:

- Inlet pressure max 120 PSI
- Outlet pressure max 20-30 psi; commonly 10-20 PSI
- Fast response time; within a fraction of a second
- Input signal under the range -10 – 10 V

The line of pressure regulators produced by Proportion Air (PA) was advertised to fit this criterion according to the local dealer, Equilibar; thus some of their products were purchased to test the

control strategy. The PA electronic pressure regulator that was ordered advertised a flow rate of 34 L/min (inlet pressure at 100 PSI) and was capable of responding to a step input of 90% change in a 1 in<sup>3</sup> volume in under 200 ms [36]. These performance characteristics appeared satisfactory for the pair of triple-convoluted air springs, considering its estimated combined volume of 33-35 L based on its maximum usable stroke length dimensions [37]. Once the pressure regulator was purchased, a Ter-ramechanics rig dedicated air supply line was installed with an air filter and manual pressure regulator to lower the supply pressure, from 120 to 35 PSI, according to the electronic valve’s manual.

Once the pressure regulator was properly installed and connected to LabVIEW, testing began to fine-tune the controller gain values. The first tests administered were a simple step input to see the response time of the system. Applying small increments of pressure change, the system had an astonishingly slow response time of near two minutes, as shown in Figure 3-6.

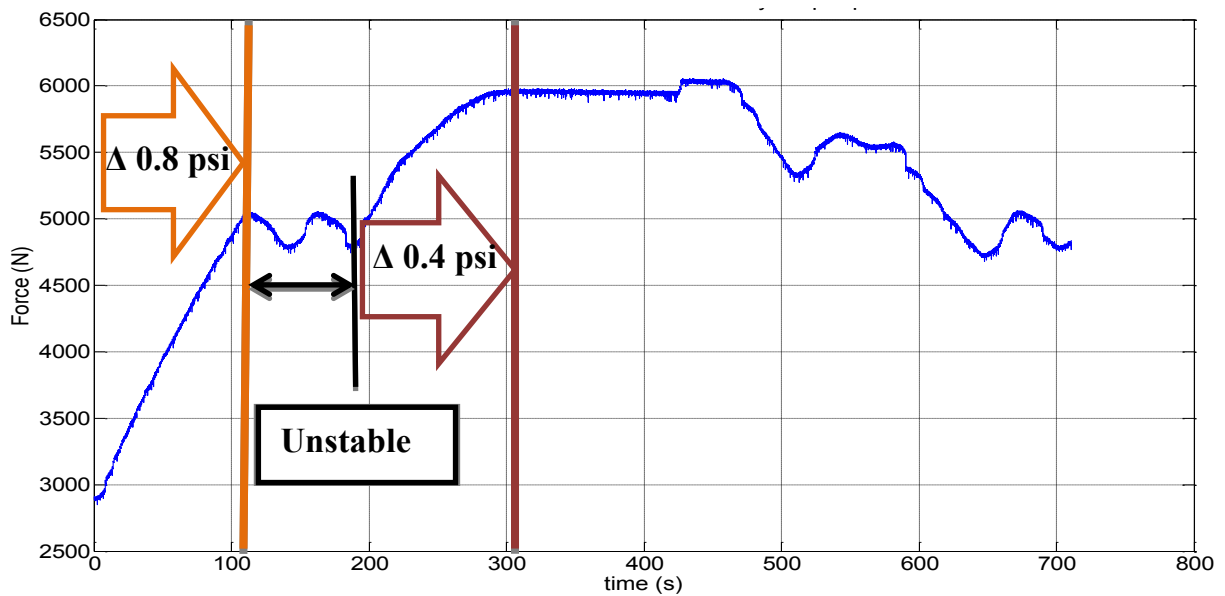


**Figure 3-6. Normal load response to two separate step inputs.**

Despite the changes made on the PI controller gains, the speed of the system was far too slow to maintain a constant tire load while rolling over a deformable surface like that of soil. Figure 3-7 shows a plot of the tire normal load traveling over soft soil from the Home to the Away position and then returning to Home. This figure shows from the beginning that the pressure regulator was unable to maintain the set normal load of 5 kN.

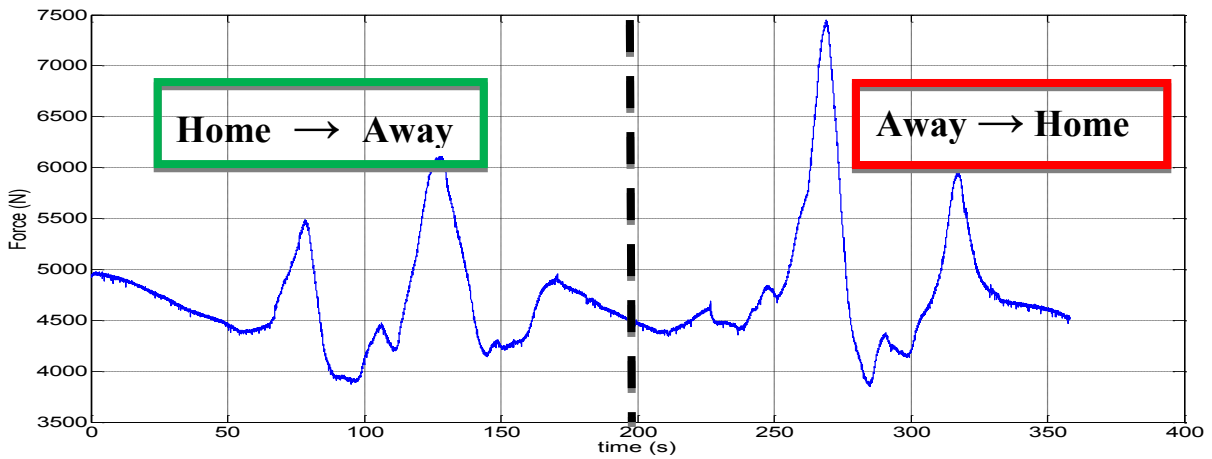


**Figure 3-7. Fluctuating wheel load of tire on soil moving forward then reverse.**

The main cause for the poor performance of the pressure regulator stems from the low pressure differential of the supply air and air in the air springs. The performance characteristics described in the product brochure were all the result of utilizing a supply air of 100 psi so once the supply air pressure was reduced dramatically, the performance of the regulator reduced as well. Following the poor performance of the pressure regulator, it was necessary to return to the original method of applying normal load with the exception of using an electronic actuator instead of manual operation.

### 3.2.1.3 Fluid Control via Flow rate Regulation

Returning to the original method of applying normal load, which is simply supplying the air springs with high pressure air and then removing or adding air as needed, it becomes evident that flow rate control can fulfill the needs of the normal load controller. Flow control will allow the air springs to be exposed to either the high-pressure supply line, ambient pressure, or held neutral, with prompt and precise switching speed among those positions. This can be accomplished by either using two separate open-and-close valves for the air supply line and environment, respectively, or using one valve that is capable of fulfilling the work of both. Additionally, a large valve port size is important for faster flow rates especially considering that the original air hose connected to the air spring were 3/8 inch in diameter but needed to be brought up to the 3/4 inch port fitting of the air springs. Considering the needs of flow rate regulation, the following products in Table 3-2 were reviewed.

**Table 3-2. Comparison of various control valves.**

Brand	Model	Flow rate (L/min)	Port Size (inch)	Shifting Time (ms)	Cost
Asco	FlowtronicsD	100-2000	-	< 200	\$ 1,300.00
Enfield	M1d	1700	3/8	2.8	\$ 570.00
Enfield	M2d	1700	3/8	2.8	\$ 598.60
Enfield	M2s	1700	3/8	2.8	\$ 492.00
OMEGA	PV104	80	1/8	40	\$ 490.00

In review of price and performance, the Enfield M1d was selected as the best answer to the normal load control problem. The M1d is a proportional pneumatic valve which utilizes a bi-directional motor, controlled by integrated on-board driver electronics, to perform very high speed pneumatic switching [38]. Because of the linear bi-directional motor, the M1d can reduce the flow area from fully exposed to neutral for either case of supplying or exhausting air to and from the air springs, respectively; this functionally allows greater flexibility with flow rate control. The valve diagram for the M1d, shown in Figure 3-8, clearly illustrates the flow direction for the five port fittings among the three extreme positions. Actuating the three positions is directly proportional to the command signal range, where the extremes are 0 V and 10 V while the neutral position is 5 V.

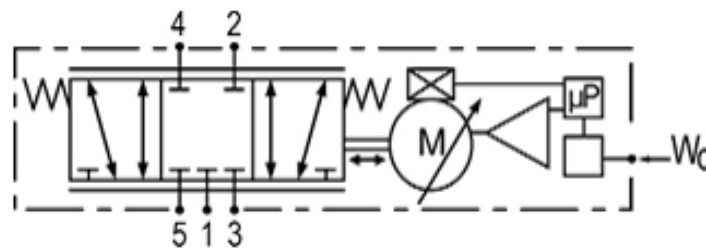


**Figure 3-8. M1d Valve Diagram (ISO 1219) from Enfield Technologies, "M1d Proportional Pneumatic Control Valve " Datasheet, pp. 1-2, 2010. Used under fair use, 2013.**

Once the M1d was ordered, the installation required a few changes to the original air spring configuration. A larger 1/2 inch diameter hose replaced the original nylon 3/8 inch that was connected to the air springs. The hose size upgrade was made to increase the airflow among the air springs. The increased airflow is especially important for when the air springs need to relieve air, which is usually at a low pressure of 15-20 psi. The M1d was installed on the rig carriage, rather than outside the rig enclosure; this position reduces the overall control volume of the air springs and hoses, which helps to ensure rapid air spring pressure changes. The command signal, power, and supply air are routed on the over-head hanger, along with other cables that go to the rig. Towards the end of the rig, a special air filter and manual pressure regulator is installed to the air supply. Figure 3-9 shows the arrangement of the new air hoses and M1d on the rig carriage.



**Figure 3-9. Arrangement of new hoses and M1d valve controller.**

Following the installation and after a few adjustments to the PI controller gains, the M1d was doing a great job of regulating air flow in the air springs and maintaining a constant normal load. When rolling over a prepared soil surface, the normal load control strategy kept the load variation under an average of 3%, as shown in Figure 3-10. When there are a few obstacles, for example a dip or mound of a few inches of soil in the tire path, the load control may vary around 5-10%, but it is quickly able to reduce the variation once back on relatively flat soil. The control algorithm can certainly be improved to handle such obstacles but its current configuration can work fine for the course of this study. A manual for initializing and using the normal load controller can be found in I.A.1.a)Appendix (E) .

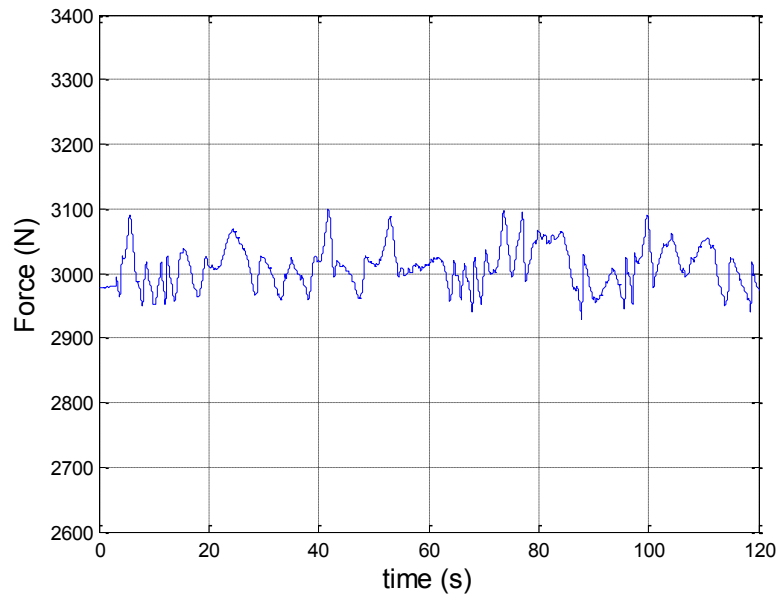


**Figure 3-10. Normal load of a rolling tire under active control at less than 3% variation.**

### 3.2.2 Robust Motor Control

As previously mentioned, the two drivetrains in the rig are controlled by the PiCPro MMC software written in the ladder logic language which is compiled and downloaded to the motor drivers. Due to the uncommon presence of the ladder logic programming language in undergraduate mechanical engineering studies, the students that have worked on the rig’s motor control had no previous experience in the language. Several programs have been made based on some lost, original code to control the rig motors in some form; as a result, all of the programs share nearly 80% of the same code with little to no comments to explain the purpose of various sections. Therefore to ensure safe and robust control of the rig motors, a well-commented, comprehensive, motor control template with multiple error-checking tools was developed.

A program written in the ladder logic language is essentially composed of graphical diagrams which are interconnected with several wires, logic functions and operators. The function blocks and operators are connected to a common power rail and will execute their function given that the initial criterion is met. The common use of the program for the rig is to establish acceleration and speed settings of the two motors, initialize hardware input, and give visual feedback to the operator. The template program developed has been tested meticulously and confirmed with the technical support staff of G&L motion to ensure that desired speeds of both motors are met to an acceptable testing range and that the rig physically stays within the confines of the soil vane. A screenshot of the program is shown in Figure 3-11.

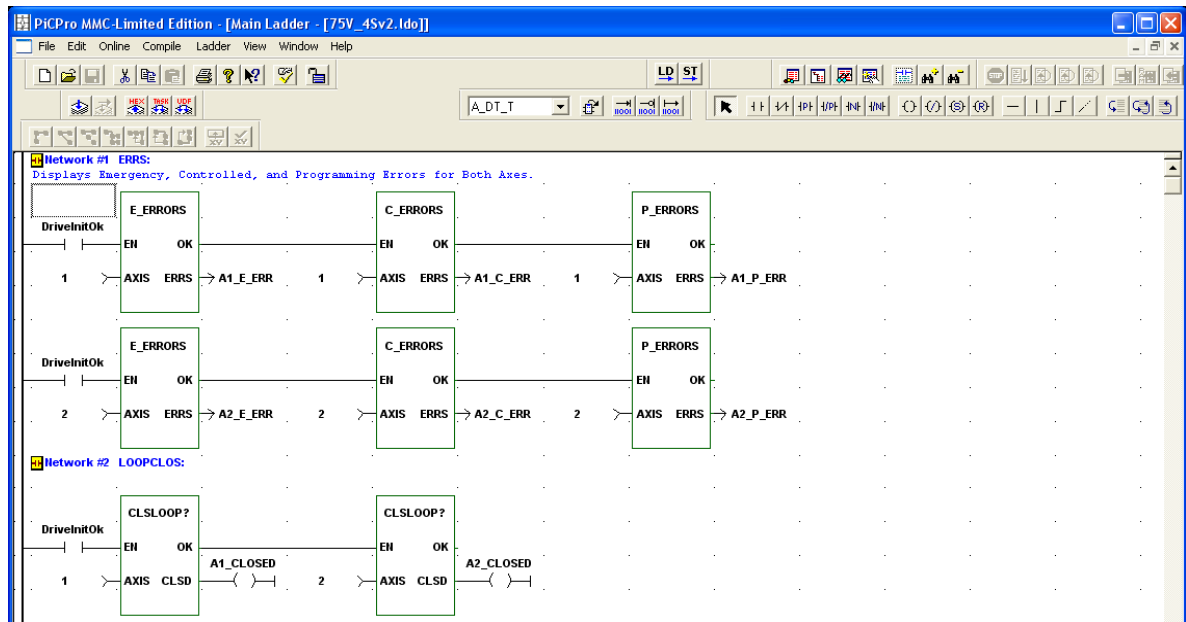


**Figure 3-11. PiCPro ladder logic program.**

Additionally, a good upgrade to the controls was the replacement of the physical handheld controller. The original controller had four buttons: power, emergency stop, and two general inputs; all of which were battered over the years of use and would occasionally not function properly. As the controller was being replaced, two additional hardware inputs were added to give the control program more versatility. The extra inputs helped make the motor control program more automatic and efficient by combining two commonly used programs together, thus reducing frequent download time. A photo of the upgrade is shown Figure 3-12.



**Figure 3-12. Comparison of old and new rig handheld control box.**

### 3.2.3 Automatic Offloading of Wheel Assembly

Throughout the preliminary test work, it was apparent that most required operations were done manually, thus several modifications were executed to reduce test preparation time and make

experimentation more consistent and automatic. One of the big changes for the rig was replacing the manual winch used to offload the wheel assembly. This function is important for replacing the test tire, to keep the test tire suspended in the air for instrument calibration, and when preparing soil for testing. The original method of offloading the wheel assembly required getting on the rig carriage and cranking the lever of the winch until the desired height was reached. The loading and offloading of the wheel assembly required to be adjusted at least 2-3 times per test run; manually doing this process for several testing hours proved to be very exhausting for the operator. The winch was then replaced with a pulley and the WARN RT15, which is an electric winch designed for All Terrain Vehicle (ATV) applications. The electric winch was installed with a rechargeable, truck lead-acid battery to handle the high current demands of the motor. The winch is controlled with an electric switch that has been extended to reach the outside of the carriage so that an operator can control the winch without climbing inside the rig. This addition has greatly reduced time in test preparation and fatigue on the operator. A comparison of the manual and electric winch is shown in Figure 3-13.

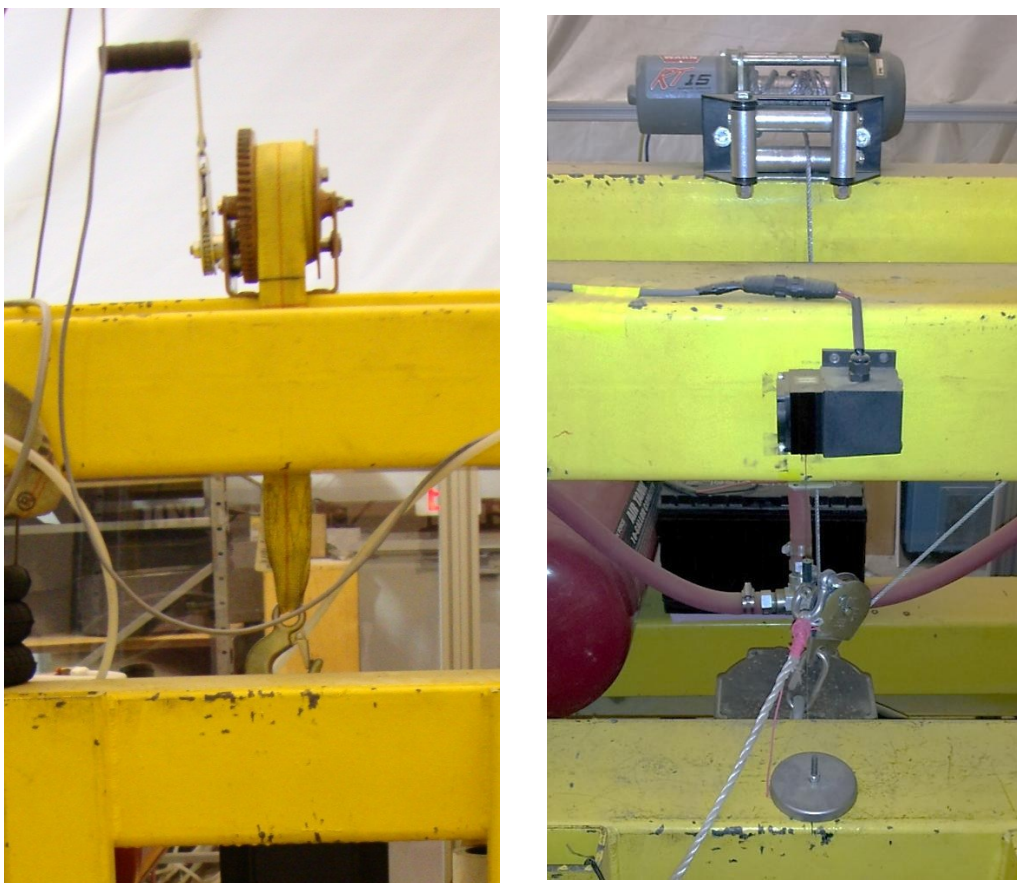


**Figure 3-13.[Left] Original Manual Winch. [Right] Electric Winch.**

The WARN RT15 was selected as a result of being resourceful with lab equipment on-hand. The electric winch was originally purchased to tow an agricultural roller used for soil compaction. The winch is rated for 1500 lb, which is well over the weight of the wheel assembly of approximate-

ly 500-600 lbs. However, the winch was designed for lateral towing, unlike its repurposed use for vertical lifting. Although this application has worked for the course of this study, it should be replaced in the future with a purpose-built vertical loading winch.

### 3.2.4 Rig - Driven Soil Compactor

As noted in the previous section, an electric winch was utilized to compact soil by pulling the winch across prepared soil. This method required using the rig to tow the roller to the Home position, physically getting in the rig to disconnect the roller and arranging the winch cable on to the handle of the roller, then activating the winch to return the roller to the Away position. This process was very time consuming and tiring for the operator. Moreover, considering that the winch was repositioned for offloading the wheel assembly, a Terramechanics rig-driven method of mobilizing the roller was approached.



**Figure 3-14. Agricultural roller along with the original position of the electric winch.**

The rig is able to easily pull the roller to the Home position; however, when the roller needed to be returned to the Away position, the rig had no support of guiding the roller in a straight path. The handle-to-rig contact would create a pivot which would push the roller into an odd direction; thus a new set of handles was machined and installed on the roller. Two arms were installed near the pivot of the roller to act as guide for when the rig was pushing the roller to the Away position. Additionally, two mounts were installed on the carriage so that the guiding arms of the roller could easily be attached or detached from the carriage. Both machined parts are shown in Figure 3-15 and Figure 3-16.



**Figure 3-15. Two views of the new guide arms installed on the roller.**

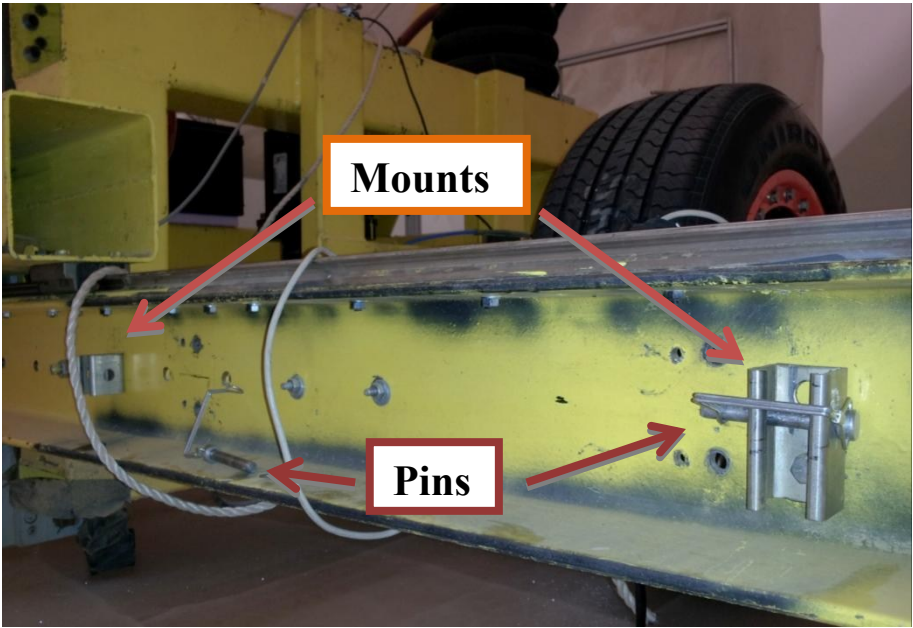


**Figure 3-16. Mounts and pins used to attach roller guide arms to the rig.**

This modification to the rollers has made the soil compaction process much faster and consistent while also covering more ground to compact and reducing operator fatigue.

**3.2.5 Rigidized Leveling Blade**

The blade used for leveling a prepared soil surface originally had the ability of using linear bearings to easily move the leveling blade to any desired height; however, this versatility induced too much flex on the blade and made it difficult to secure the blade at the desired height. The leveling blade is a simple object; it's a wooden board with a steel straight edge supported by two square-shaped, hollow steel beams. The blade would attach to the rig carriage via two linear bearings and was secured in place by two clamps, as shown in Figure 3-17 (b). When soil would accumulate at the

blade, the reaction force would create a moment on the linear bearings which would in turn, flex the entire blade, resulting with a test surface of varying height. This problem was solved by simply removing the bearings all together, machining a slot on the support beams of the blade and placing a steel C-channel with two threaded holes inside each support beam to act as a large nut and firmly secure the blade to the carriage. Figure 3-17 (a) and (c) show the modified blade in detail and how it's fixed on the carriage, respectively.



(a)



(b)



(c)

**Figure 3-17. (a) Detailed view of the modified blade. (b) Old configuration with linear bearings and clamps. (c) New configuration secured on rig carriage.**

Since the modification, the leveling blade rarely needs adjustment and is held at the same height throughout testing which helps to ensure a consistently prepared test soil volume.

### **3.3 Soil Measurements**

In situ soil measurements are important to confirm soil conditions are consistent between test runs. The soil conditions that are frequently measured are the relative soil height, compaction, and moisture content. The instruments used to take these measurements are discussed in this section.

#### **3.3.1 Real-time Soil Height Monitor**

A parameter of interest for tire performance on soil is the wheel sinkage. In this study, it is important to measure the soil height, or relative distance from the top surface of a prepared soil to the center of a rolling test wheel, to measure wheel sinkage. A more detailed description of the novel approach used to measuring wheel sinkage will be explained further in the document. The instrument used to make this measurement has to be nonintrusive to the prepared soil and be located very close to the test tire, thus an ultrasonic sensor was chosen to measure the soil height.

An ultrasonic sensor works on a similar principle as radar or sonar; it sends a high frequency sound wave and listens for the echo to interpret the distance traveled by the sound wave. The sensor purchased to carry out this measurement is the Parallax PING)))™ ultrasonic distance sensor. The PING sensor has a measuring range of 2 cm (0.8 inches) to 3 meters (3.3 yards) and is easy to use with the single transistor-transistor logic (TTL) communication pin [39]. The PING sensor can only provide raw time data in a variable-width pulse, corresponding to the distance measured, so it is controlled with a microcontroller and LabVIEW to make the measurements and organize the data into a TDMS file format.

The Arduino UNO is the microcontroller used to interface with the PING sensor and communicate with a computer over LabVIEW to save the data. The UNO is a versatile microcontroller that is programmed with C and C++, and among the several features of the UNO, the digital input output pins capable of Pulse Width Module (PWM) are used to control and measure the PING sensor. The UNO is also used to interact with a Real Time Clock (RTC) to gather timestamps of when distance data is collected; this allows easy correlation with other data collected at the time using separate instruments. Although the UNO could be coupled with an SD card to be used as a data acquisition system, using LabVIEW instead to save the data gives more flexibility with organizing the data while also reducing the program complexity of the UNO. The PING sensor and UNO are shown fitted in a custom-made mount in Figure 3-18.

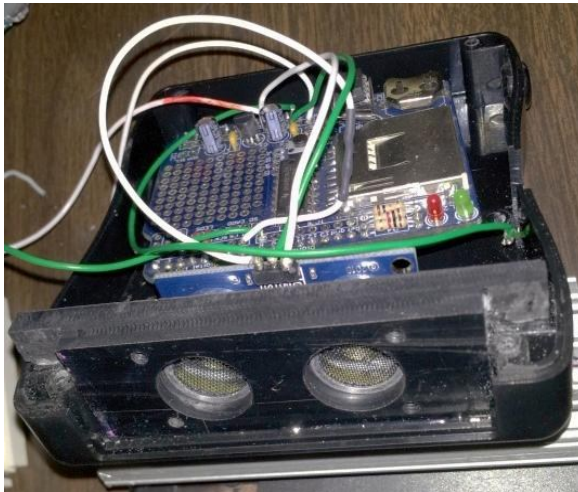


**Figure 3-18. PING sensor and Arduino UNO fitted on the custom mount.**

Although the UNO controls the PING sensor, the entire system is controlled by LabVIEW. LabVIEW communicates with the UNO via serial communication over a USB port; it sends a message to the UNO when it is ready to collect data or terminate communication. Along with organizing data among large datasets, LabVIEW also plots the measurement over time. Figure 3-19 shows the LabVIEW program used to control the system.

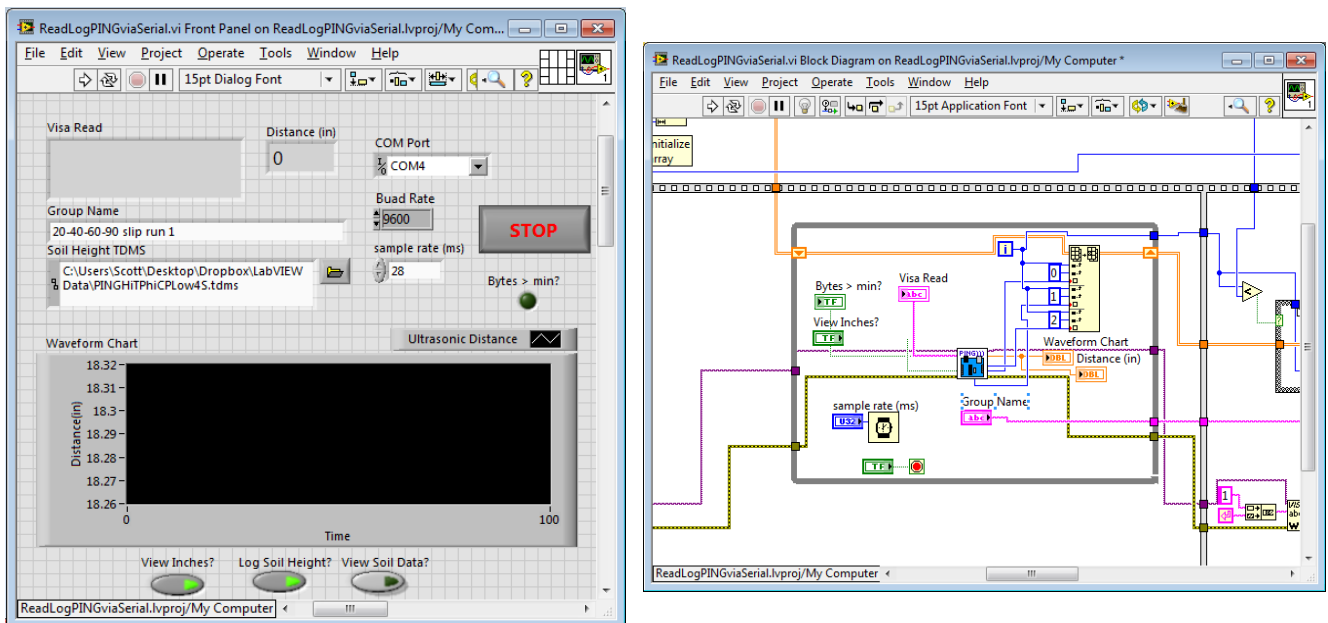


**Figure 3-19. LabVIEW soil height monitor VI [left] and block diagram [right].**

The mount made for the soil height monitor was made to have a slim profile and gives many options for positioning the sensor on the rig. The mount is attached to the rig using 80/20 aluminum bars. The configuration used for tire-soil testing required placing the sensor system next to the tire. A flat steel plate was placed in the Home position of the soil vane for tire loading; this plate provided a

baseline reference for the sensor system to use for calibration. The configuration of the soil height monitor used for the work in this study is shown in Figure 3-20.



**Figure 3-20. Soil height monitor system mounted on the rig for testing.**

### **3.3.2 Cone Penetrometer**

Prior to running a tire over soil test run, measurements of the prepared soil compaction gradient (G) are taken with the Rimik CP40 II cone penetrometer (CPT). These measurements are taken to understand the relative density of the soil and ensure consistent soil compaction between test runs. The CPT essentially uses a load cell attached to a rod and cone of a known surface area to provide cone penetration pressure as the unit is inserted in the soil. The depth of the insertion is measured with an ultrasonic sensor attached to the base of the CPT. These sensors combined give the cone penetration pressure versus sinkage. The CPT base has a display with buttons to allow the operator to adjust settings as necessary and organize the data between large datasets.

The CPT is used by applying a downward, even force on the two handles of the base until the unit has collected data for the range specified in its settings. It will sound an alarm when all the data is collected and then display a plot of the pressure versus sinkage data collected. Depending on the user settings, it will prepare itself for another test run. Before every test run, 6-8 insertions are collected along the length of the prepared soil. Data can be extracted from the CPT by connecting the base to a computer via RS-232 serial port and by downloading the data into a comma-separated values (CSV) file format for further processing.

### 3.3.3 Soil Moisture Content

The moisture content (MC) present in a soil has been observed to drastically affect the tire-soil interaction; therefore, it is important to take constant measurements of the MC and adjust as necessary between test runs. The MC of the soil is measured using a standardized microwave oven heating test [40]. The basic idea of this test is to measure the change in weight of a soil sample that has been heated in the microwave numerous times until the weight change stabilizes. Measuring a constant weight change should indicate that all the moisture in the soil sample has evaporated. This test is done using a simple microwave, a 0.01 g accurate weight scale, and several heat-treated glass vials. These items are shown in Figure 3-21.



**Figure 3-21. Microwave, weight scale and glass vials of various sizes used for MC testing.**

The procedure followed for each test run is to collect 3-4 samples of freshly prepared soil along the length of the soil vane and then measure the weight change of the vials after a series of a few minute sessions in the microwave. This process can take over 10 minutes to get a consistent reading, so to save time, 2-3 runs worth of sealed soil samples can be tested at a time. Once the measurements are noted, the vials are emptied out, cleaned with pipe cleaners (chenille stems), and ready for further testing.

This approach for measuring MC was used over specialized equipment solely for its simple, ease of use. The AVDL has a Vertek dynamic cone penetrometer (DCP) instrumented with Soil Moisture Resistivity (SMR) probes which can give instant MC results; however, the instrument requires two operators and is difficult to manage on the rig due to its size and weight. The SMR probe also only provides one-digit accuracy for MC compared to the tenths place digit accuracy of the microwave method.

## 4 Development of a Tire Deflection Measurement System

This section will elaborate on the design, development, calibration and rough validation of the Wireless Internal Tire Sensors (WITS) used to measure tire carcass deflection when rolling and also in the estimation of tire sinkage.

The primary goal of this study was to acquire tire performance data as a result of maneuvering over various conditions. Drawbar pull capabilities and tire sinkage are very good representative parameters of tire performance; however, the Terramechanics rig lacks the capability of accurately measuring actual wheel sinkage as it can only measure vertical wheel displacement. Therefore, supplemental instrumentation methods were sought out to give the Terramechanics rig wheel sinkage measurement capabilities.

Additionally, the rig lacks rolling radius measurement. This is especially important to the rig as this parameter is required to accurately control wheel speeds to reach desired slips. The method commonly used for rolling radius determination is measuring the travel distance of a loaded wheel after a full revolution on a flat surface, under steady-state, self-propelled conditions, so that it does not experience draw bar pull. This condition is recognized to produce zero slip because there is no drawbar pull. However, by the principle of thrust that the wheel must apply to overcome motion resistance, shearing acting takes place in the wheel-terrain interaction [41]. Therefore although no drawbar pull may be generated, due to the sole presence of thrust, wheel slip occurs [42, 43].

A similar method can be applied to a towed wheel, which would avoid applying a driving torque to provide thrust. However, under a towed condition, the wheel has been observed to produce negative wheel slip, or wheel skid [41, 44]. Both cases above were observed with a rigid wheel. Thus, when factoring in a flexible wheel, such as a tire, rolling radius determination becomes even more difficult.

Therefore, developing a method of measuring tire deflection to estimate rolling radius and supplement wheel sinkage determination was pursued.

### 4.1 Design Considerations

Following the literature review, common technologies used to take tire deflection measurements are magnetic, piezoelectric, ultrasonic, microelectromechanical systems (MEMS), and general optical sensors. The no-contact instruments were favored considerably in this study to avoid interference with tire deformation, so ultrasonic and optical sensors were reviewed.

Due to the relatively small path for tire-soil testing in the rig soil vane, getting more than one sensor in the tire was vital to provide a high resolution of data collected at the contact patch, so cost per sensor was of great importance.

Considering the unique application for a deflection measurement system in this study, no commercial systems were found to meet the requirements and budget. Therefore a small, lightweight and power efficient microcontroller was needed to handle the unique controls and data acquisition for the required large number of sensors.

Lastly, an easy and reliable method of communicating with the sensor system is desired for activation and data retrieval. Methods commonly used for communicating with an instrumented tire are either a slip ring or radio link.

A slip ring can ensure hardwired, reliable communication but can be very costly as slip rings alone are expensive and increase in cost depending on the revolution speed and number of wire connections. Additionally, insuring a sealed method of feeding data and power wires through the wheel to communicate with the sensors is also a costly, and usually custom, requirement.

However, a wireless system avoids such costs and material needs, in exchange for program complexity, possible loss of data through communication, and the requirement for a remote power supply. Deciding which of the two methods were to fit the purpose of this study was strongly reviewed and eventually, the final development geared towards making the sensor system wireless.

In summary, the design considerations for the tire deflection system are as follows:

- Use of no-contact sensors, ideally either optical or ultrasonic
- Relatively large and inexpensive array of sensors required for vast amount of data collection of the contact patch
- Microcontroller required to handle controls and data acquisition of the sensors
- Wireless method of communication to handle system activation and data recovery

## ***4.2 List of Materials***

Popular hobby websites and electronic component distributor web stores were great resources to find the materials required to meet the design considerations and keep costs low. The electronic hobby sites were especially helpful in determining which sensors and microcontrollers had a large following to ease familiarization of the electronic and program coding.

Choosing the sensor to make the deflection measurements eventually came to a decision between the SHARP GP2Y3A001K0F wide angle distance measuring sensor and the PING)))™ Ultrasonic Distance Sensor. Both were found to differ slightly in cost and appeared to be able to give ac-

curate measurements required for the deflection sensor system. The capabilities and shortcomings of each sensor were strongly reviewed before deciding on which to use for deflection measurements.

The SHARP GP2Y3A001K0F distance measuring sensor is an integrated unit composed of a position sensitive detector (PSD), five infrared emitting diodes (IREDs), and a signal processing circuit [45]. This unit is capable of measuring distance between 4 to 30 cm with little to no issues attributed to desired object detection reflectivity, environmental temperature, and operation duration due to the administered triangulation method used by the integrated circuit. Due to the five IREDs used by the sensor, it has a wide angle measuring range of 25°. The outputs of all IREDs go to a single analog voltage output. The sensor has a small volume of 40 x 20 x 15 mm and only requires an average supply voltage of 5 V with typical current consumption of 30 mA.



**Figure 4-1. SHARP GP2Y3A001K0F wide angle distance measuring sensor fitted to an early mount prototype.**

The PING)))™ ultrasonic sensor is the same unit that was presented in the previous chapter and was instead decided to be used solely for soil height detection. This decision was made based on the wide angle measuring range, lower cost, durability and reliability of the SHARP sensor. Unbeknownst to the original material search, the PING sensor was later discovered to be very sensitive to noise, especially when close to the rig wheel motor.

The Arduino Mega 2560 R3 was found to be a versatile microcontroller that could handle all the control logic required for the sensors and efficiently serve as a data acquisition unit. This is near identical to the UNO discussed in the previous chapters and differs by having more analog inputs and digital input/output (I/O), larger flash memory, and three additional hardware serial ports, among various other added features. The Arduino UNO was originally considered for the task but was eventually considered to have too few analog inputs and was recycled to be used for the soil height reader.

Due to the near similar physical layout that the Mega shares with the UNO, most specialty circuit boards, often called shields, designed for the UNO were also compatible with the Mega. This provided the opportunity to easily add extra features to the Mega without having to build a unique

circuit board. As a result of this expandability, the Adafruit Data logging shield was selected to handle saving data collected from the sensors to an SD card for permanent storage. This data logging shield also has a real-time clock (RTC) chip to provide UNIX timestamps, which is a commonly used time reference defined by the seconds elapsed since the Coordinated Universal Time (UTC) dating to January 1<sup>st</sup> 1970, not including leap seconds. The RTC would aid in synchronizing data between the tire sensors and the rig which also uses UNIX timestamps.

While in the design stage of the tire sensor system, the decision to go completely wireless had not been confirmed; nonetheless, wireless modules were reviewed and the module determined to fit the application best was the XBee® Series 1 Radio Frequency (RF) module. This module runs the Institute of Electrical and Electronics Engineers (IEEE) standard 802.15.4 protocol which supports the modules low-cost and low-power, point-to-point or star topology capable networks [46]. It is a transceiver, functioning as both a receiver and transmitter. It has an indoor range of 100 ft (30 m), with a transmission power of 1 mW (0 dBm), transmitting (TX) and receiving (RX) current draws of 45 and 50 mA, respectively, at 3.3 V. It can also perform simple analog-to-digital conversion, digital I/O, and I/O line passing, which turned out to be a very useful feature to interact with the tire sensors. This module was preferred over other radio technologies, such as Bluetooth and Wi-Fi, because of low power consumption, low cost, good transmission range, and ease of use. By default the modules are configured to simply serve as direct wire replacements but can be configured to operate in a complex network. Because of the wide market of Arduino compatible shields, an XBee-specific shield was available to easily connect the XBee directly to the Mega.

The Arduino Mega, Adafruit data logging shield, XBee series 1 RF module, and XBee shield are shown in their near final design in Figure 4-2.

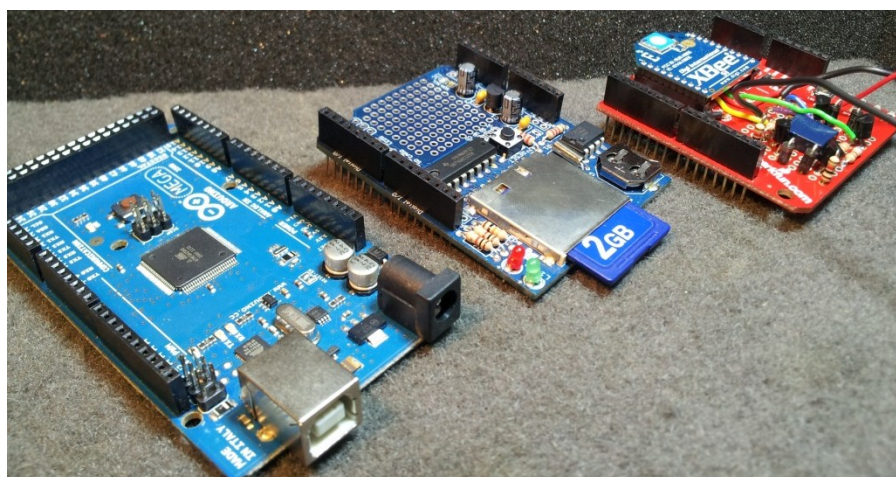


**Figure 4-2. Pictured on the left is the Arduino Mega, center is the data logging shield with an SD card, and on the right is the XBee shield fitted with an XBee series 1 RF module.**

The estimated initial cost for the sensor system totaled to about \$500 and is shown in detail in Table 4-1.

**Table 4-1. Estimated cost of the originally purchased materials**

Main Components	Purpose	Voltage Supply	Price per Unit	Qty.	Total
<b>Sharp Distance Measuring Sensor (GP2Y3A001K0F)</b>	4-30 cm sensing range	4.5 ~ 5.5 V	\$ 34.65	9	\$ 311.85
<b>Arduino Mega 2560 R3</b>	Perform computations	7 ~ 12 V	\$ 79.95	1	\$ 79.95
<b>Triple Axis MEMs Accelerometer - MMA7361</b>	accelerometer for sensor selection	3.3 V	\$ 11.95	1	\$ 11.95
<b>XBee Series 1 chip antenna module</b>	Transmit/Receive data	3.3 V	\$ 22.95	1	\$ 22.95
<b>XBee Series 1 wire antenna module</b>	Transmit/Receive data	3.3 V	\$ 22.95	1	\$ 22.95
<b>XBee Explorer USB</b>	XBee interface to PC	N/A	\$ 24.95	1	\$ 24.95
<b>XBee Shield</b>	XBee interface to Arduino	N/A	\$ 24.95	1	\$ 24.95
<b>SD Card Shield</b>	Data-logging	N/A	\$ 14.95	1	\$ 14.95
<b>Miscellaneous Electrical Components</b>	Circuitry demands, brackets, etc.	N/A	\$ 150.00	1	\$ 150.00
<b>Total</b>			\$ 387.30		\$ 499.55

Although not part of the original design, an accelerometer was purchased to aid the microcontroller in efficiently selecting a sensor to take measurements and keep random data collection at a minimum. This will be further explained in the upcoming subsections.

### **4.3 Familiarization of Electronics**

The single greatest challenge of developing the deflection measurement system was becoming familiar with the electronics and programming required to ensure efficient data collection, prompt control strategies, and robust performance under heavy testing demands. The main tasks to achieve these goals are as follows:

- Learn the microcontroller programming language and how to interact with the sensors, shields, and XBee module
- Ensure proper use of the SHARP distance measuring sensor to collect accurate deflection measurements
- Develop control strategy to collect and save measurements

### 4.3.1 Microcontroller

The Arduino lines of microcontrollers have very powerful computing capabilities for its size and are commonly used to solve many controls and data measurement problems for countless mechatronic applications. Understanding the programming language of the microcontroller is fundamental to ensure its proper and efficient use to handle rapid, accurate measurements of the tire deflection in soil demands of the study.

The Arduino Mega is programmed with the open-source Arduino IDE software. The programming language used in the software is essentially a collection of functions developed in the C and C++ languages, and because of this background, most commands from either language can be used in the programming of the microcontroller. An example of the software and code used in the final program is shown in Figure 4-3

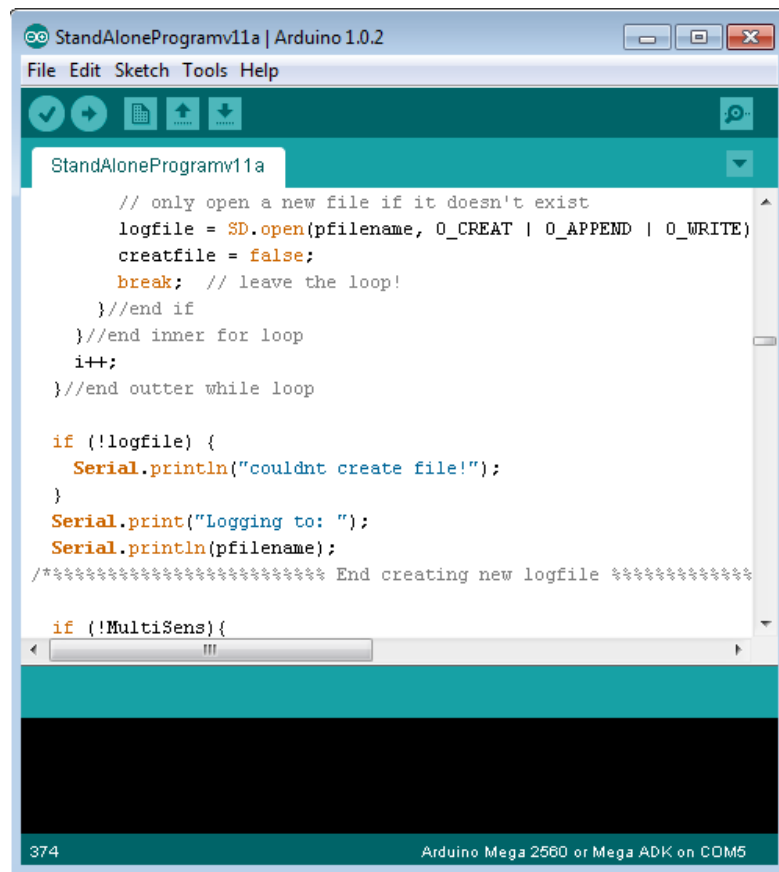


**Figure 4-3. Screenshot of the Arduino programming software.**

The basic tasks for the Mega is to interface with the distance measuring sensor, take desired measurements, save the collected data to the SD card in the data logging shield, and repeat until told otherwise. The communication aspect of it makes no difference whether the system was to be wired or wireless. This versatility is possible because of the transmitting/receiving methods of the XBee that simply connect to the same communication lines (TX and RX) required for a Serial connection,

which is the process of sending data one bit at a time, sequentially, over a specific channel. Serial communication is how a machine communicates with the Mega to download new code and view the programmed output of the Mega, and is one of the common methods that the Mega can use to interact with other devices.

The data logging aspect of the Mega was important for prompt data collection and organization of large datasets. The basic interaction between the Mega and the data logging shield would be to retrieve a timestamp from the RTC chip, collect a data point, and repeat until the system had a sufficient amount of data to save to the SD card. Frequent writes to the SD card are both computationally intensive and power demanding, so keeping the SD writes fairly spaced out was a design consideration for the final program. To reduce the amount of input from the operator when the system would be in use, the Mega would need to be programmed to automatically generate a unique file name to distinguish and organize large data sets.

### **4.3.2 Distance Measuring Sensor**

The SHARP GP2Y3A001K0F was selected because of its wide measuring range which could also be used to profile the tire contact patch instead of just measuring the deflection. Soon after receiving the sensor, it was quickly discovered that it is not as routine as initially anticipated. Understanding how to use the sensor and ensure its accurate distance measuring capabilities was imperative to the tire sensor system design.

The sensor has a wide measuring range because it utilizes five individually-spaced IREDS to take measurements within the  $25^\circ$  range which indicates that each IRED is separated by  $5^\circ$ . Because there is only one PSD and analog output for the sensor, only one IRED can be used at a time. When the sensor is activated for use or when switching between IREDS, a specific timing algorithm must be followed so that the sensor does not collect noise.

The basic methodology for using the sensor begins with sending a digital signal to activate the sensor and a separate digital signal to choose which of the five IREDS to use for measurement, each of which having their own digital input. Within a time span of approximately  $16.5 \pm 3.7$  ms the first measurement is taken; however, collecting the measurement immediately will result in an unstable output. An additional delay of 5 ms maximum is required before a clear signal is provided of the first measurement. Once the IRED is active, it can take continuous measurements within each  $16.5 \pm 3.7$  ms window of opportunity, idle for a maximum of 5 ms, then collect the earlier made measurements and repeat. The entire process is repeated if another IRED is selected for measurement, where the change must occur within a minimum duration of 5 ms. The chart sampled from the sensor datasheet[45], in Figure 4-4, clearly demonstrates the timing method to follow for data collection.

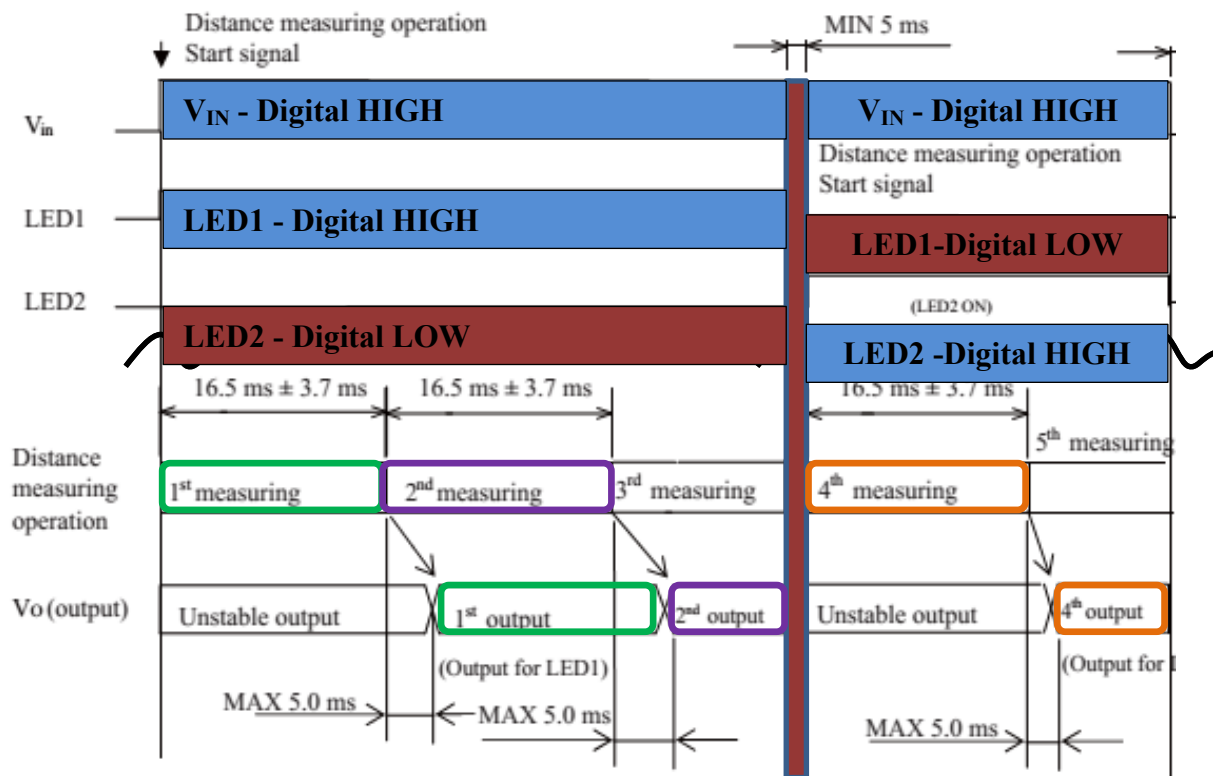


**Figure 4-4. Timing chart for proper use of the sensor from SHARP, "Wide angle Distance Measuring Sensor Unit," GP2Y3A001K0F Datasheet, 2006. Used under fair use, 2013.**

The timing chart for proper IRED usage in Figure 4-4 also iterates that only one IRED can be activated at a time to take measurement. The same process can be repeated for all IREDs or one IRED can remain constantly measuring. If the timing schedule is ignored the sensor will continuously output noise while also providing the measured distance from the target. An example of this case is shown in Figure 4-5.

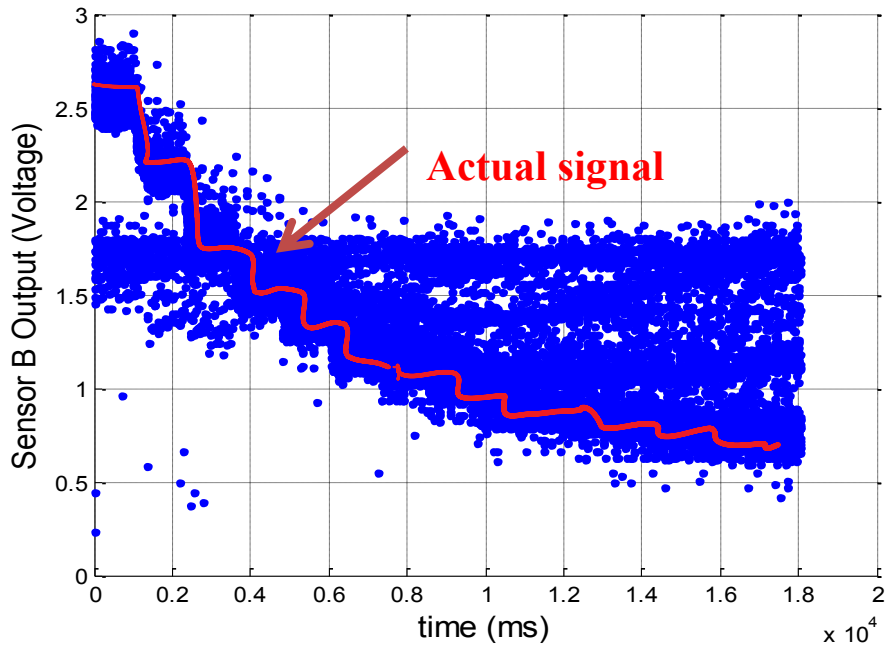


**Figure 4-5. Voltage output of a sensor measuring a moving surface while ignoring the timing schedule.**

When following the timing schedule, the sensor output turns out more precise, as shown in Figure 4-6, where the sensor is measuring the distance of an object moving in 1 cm increments.

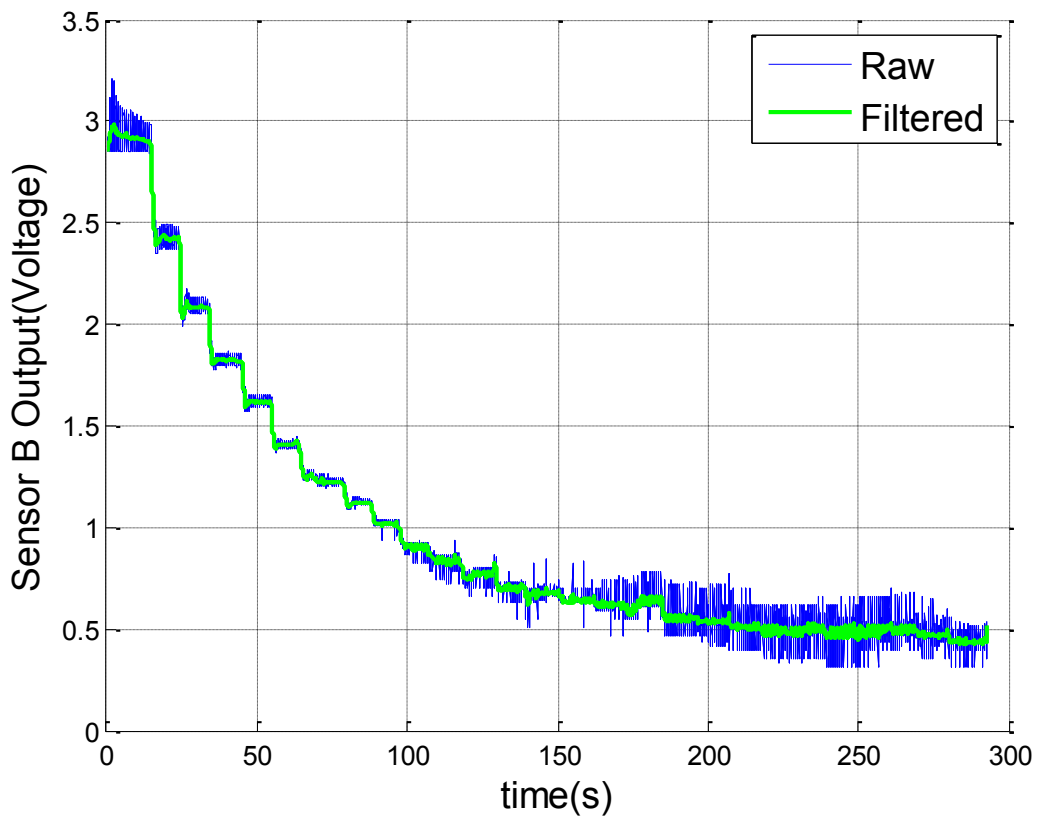


**Figure 4-6. Raw and filtered voltage output of an object moving in 1cm increments.**

The resolution of the voltage-distance relationship is also very evident in Figure 4-6. The initial measurement represents the object standing the minimum 4 cm distance away from the sensor. As the object is distanced out of measuring range the voltage relationship follows a decaying pattern. Once the object is about 15 cm away from the sensor (occurring at the 150<sup>th</sup> second of Figure 4-6), the change in voltage is very small in comparison with the first 15 cm. Because of this decrease in voltage-distance resolution, a bracket would be needed to elevate the sensor from the inner wheel so that the measuring range can stay around the 3V to 0.75 V measuring range, which is equivalent to a maximum distance of 20 cm.

Considering the timing schedule that must be followed for clear sensor measurement, arranging the sensors in a consecutive order along the inner circumference of the rim can allow ample amount of time for each IRED, of each sensor, to take a few samples when the IRED is perpendicular to the tire contact patch, thus providing optimal coverage. Following this approach with eight sensors equally spaced around the wheel rim would yield the design represented in Figure 4-7.

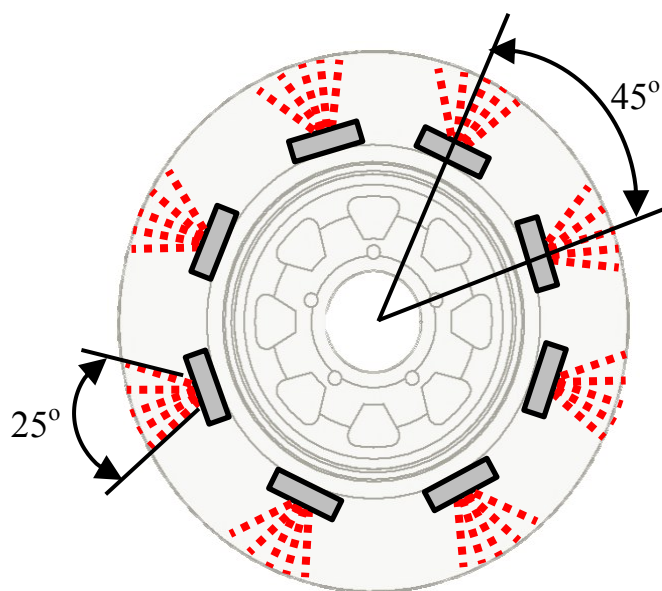


**Figure 4-7. Original sensor wheel arrangement diagram.**

Because tire deflection in the radial direction is of high priority for rolling radius and sinkage estimations, no attempt was made to rearrange some sensors to measure deflection in the lateral direction. This can be reserved for future research interests.

### **4.3.3 Proof of Concept Test**

A small false wheel was made for code development purposes and to provide a proof of concept for how the sensors can be mounted to a tire rim and used to measure tire carcass deflection. The instrumented false wheel is shown in Figure 4-8.

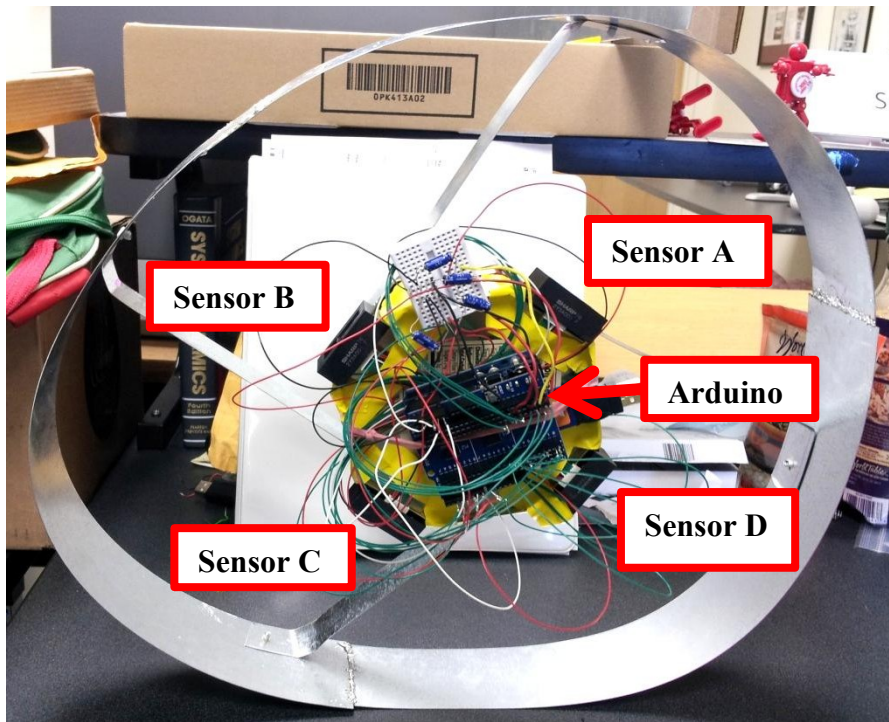


**Figure 4-8. Proof of concept false wheel**

The false wheel is made of very thin sheets of aluminum, which allow it to deform like a tire. The “hub” of the false wheel is instrumented with four of the SHARP sensors along with the Arduino microcontroller to monitor changes in the belt of the wheel. Different conditions were applied to the false wheel such as loaded, unloaded, rolling, and bouncing, which were measured by the sensors. For simplicity, only the center IRED of each sensor was used to measure deflection. A test run of both bouncing and rolling of the wheel resulted in the output shown in Figure 4-9.

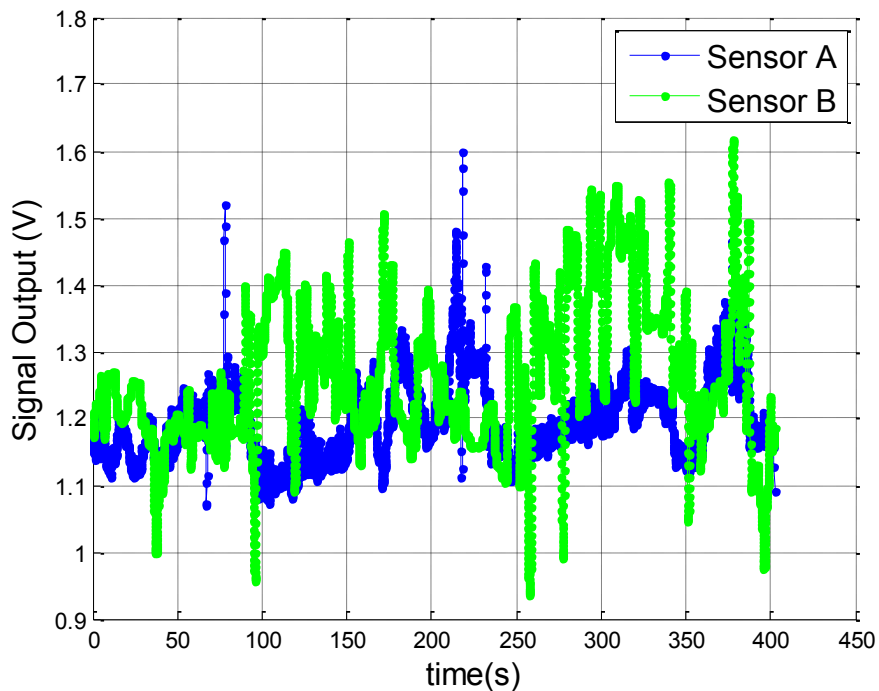


**Figure 4-9. Results from bouncing and rolling the false wheel, sensors A and B**

As expected, given the flimsy structure of the aluminum false wheel, the sensors recorded various changes in magnitude in the belt of the wheel. The changes can be compared with the initial distance measurement which is representative of the wheel's undeformed radius. The peaks in the output indicate the smallest distance measured by the sensor which would correlate to direct contact patch measurement, as this would be the only point of the tire with the least amount of distance from the rim.

#### **4.3.4 Sensor Selection Control Strategy**

Considering that the Mega needs to follow a timed schedule for distance measurements and that results need to be logged to an SD card, a control strategy that yields frequent contact patch measurements was in need of development. The initial control algorithm tested was to simply activate a sensor and its specific IRED, take a few measurements, then repeat. After a fair amount of measurements were collected, the data could then be written to the SD card and the entire process continues to repeat while also switching between IREDs and sensors. This approach was adequate for prototyping the control algorithm and performing some preliminary test work on a false wheel; however, measuring deflection at the contact patch occurred only by chance, while a lot of irrelevant information was collected. Therefore, a smarter method of selecting only a sensor and IRED in view of the tire contact patch was pursued.

One method of detecting contact patch position for deflection measurements is taking continuous samples of all sensors to see which sensor is relatively close to facing the contact patch. This concept can work; however, it would induce a computational draw on the system as the Mega would have to constantly take samples of each sensor and IRED with 1/40<sup>th</sup> of a chance of being useful before being able to collect contact patch data. The sensors can also occasionally output noise, which can throw off the detection of the contact patch. Therefore, using a motion sensitive sensor, such as an accelerometer, can provide reliable data that the microcontroller can use to make intelligent decisions on which sensor and IRED to use for measuring carcass deflection at the contact patch.

An accelerometer simply measures the accelerations experienced by the device; if kept still or at a constant speed, the only acceleration it will measure is gravity. The measure of gravity serves as a perfect reference for determining an accelerometer's change in position, so a triple axis accelerometer was purchased to serve as a reference for the Mega. The MMA7361L is a capacitive, micromachined accelerometer that includes various features such as signal conditioning with a low-pass filter, temperature compensation, and selectable acceleration sensitivity, among others. It was a suitable choice for the task due to its low acceleration sensitivity.

The concept use for the accelerometer is to determine the relative position each sensor has with the device, as it rotates with the wheel, and use this information for selecting the sensor that is approaching the contact patch. This way, as a sensor is approaching the contact patch, the IRED closest to the contact patch can begin measuring; as the sensor moves along the deflected region, the IREDs are constantly being switched to maintain direct measurement of the carcass deformation.

This decision-making is very straightforward for the Mega to handle, as it can make a decision on which sensor to use for measurement once it has converted the accelerometer vector into an angular position. The accelerometer can also supply important information about the tire that is not currently being monitored. This includes integrating the accelerometer data to obtain the angular velocity of the wheel and observing the offset of the device to determine the camber angle of the wheel.

#### **4.4 *Sensor Rim Attachment Methods***

Attaching the sensor system to the rim of the wheel proved to be a design challenge. It was of good value to keep the sensor system adaptable to a wheel rather than making one specific wheel built for the sole purpose of instrumenting the sensors. The sensor attachment method also involved determining how to instrument the wheel, such as, whether to attach the sensor prior to or post tire installation. Three methods were explored before deciding on the final attachment method.

##### **4.4.1 *Wheel Strap***

TPMS sensors usually are fixed to a wheel by attachment directly to the tire valve or to a stainless steel strap that fastens to the small, inner circumference of the rim. Fastening the wheel strap prevents the sensor from moving inside the wheel. This amount of rigidity is desired for the tire sensors, so a steel strap was purchased to attempt this method of sensor-rim attachment.

To attach the sensors to the rim, simple mounts made of a soft aluminum sheet were cut and drilled so that the sensors could easily be screwed onto the mounts that could feed through the strap. The method of tire installation attempted for this design was to fit the sensors to the rim, assuming that the sensor profile was low enough to avoid interaction with the tire installation. However, this was not the case as the tire bead hugged the rim very closely during the installation and damaged a few of the sensor mounting points. The strap also was difficult to fasten while the sensors were in place because as the strap was being tightened, the slack of the strap pointed outward and interfered with the mount of the nearest sensor.

#### 4.4.2 Hook and Loop Fastener

Following the failure of the of the TPMS strap, the next approach taken was instrumenting the wheel post tire installation and attaching the sensors with hook and loop fabric, commonly referred to as Velcro. This method would avoid damaging the sensors during the tire installation and would require attaching the sensors by mating the hook and loop fasteners glued to both the wheel and sensor. Attaching the sensors to the rim was difficult as the space clearance is very small; however, the real challenge of this method came from sealing the final bead of the tire. An example of installing the tire and sensors using an electro-pneumatic tire changer from a local auto shop is shown in Figure 4-10. The shaft that is depressing the tire sidewall in Figure 4-10 was fundamental to the attachment of all sensors due to the little clearance space available between the bead and outer rim of the wheel.



**Figure 4-10. Tire installation and instrumentation with an electro-pneumatic tire changer**

The issue commonly faced when sealing the final bead of the tire came from the backlash that would occur once sealed. The entire sealing process was done very delicately to prevent damage to the sensors and as a result of the slower method, the tire and tire changing machine would experience more resistance than with a normal tire installation. Once the final bit of the bead was ready to pop in place, the pop would deform the tire momentarily inward and usually knock a sensor out of its position in the process.

This method of installing both the tire and sensors was often very difficult and tedious work, usually resulting in a sensor put out of place. Because of the need for a professional electro-pneumatic tire changer, frequent trips to the local auto repair shops for iterative trial-and-error designs was not feasible. Furthermore, the hook and loop fasteners did not provide a rigid connection with the sensors, resulting in the sensors' measuring line-of-sight to sway off the axis normal to the inner tire carcass. Lastly, the aluminum mounts made for the sensors to mate with the rim were too flexible and would most likely offset the measuring line-of-sight of the sensors.

#### 4.4.3 Custom Mount

In review of the failed attempts to find a rigid sensor-rim attachment, the criteria to follow for the new and final method are listed below:

- Simple procedure for changing the tire manually at AVDL
- Rigid and elongated mount for the sensors
- Firm and flush attachment to the rim

Meeting the three requirements listed above were fulfilled by purchasing manual tire changing equipment and a bead lock wheel, fabricating leveled mounts out of hard-plastic, and utilizing 3M™ Dual Lock™ Fasteners for the mount to rim attachment. The custom mount and new fastener are shown in Figure 4-11.

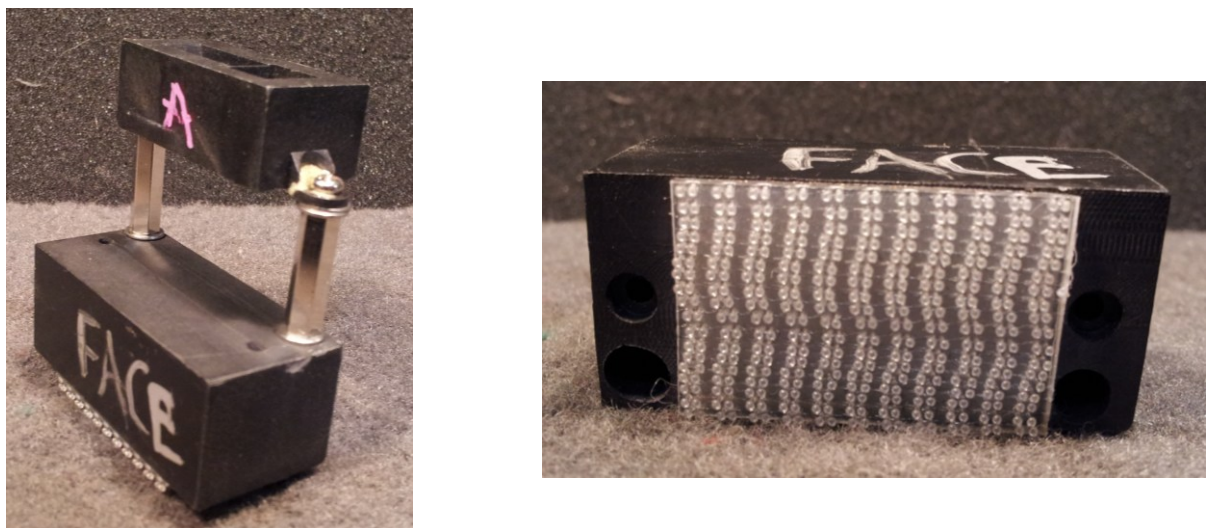


**Figure 4-11. Custom mount (left) and new fasteners (right).**

A standard manual tire changer was purchased so that the tire instrumentation can be done more delicately whereas the installation was often rushed when installing the tire at a local auto repair shop. Although the manual tire changer itself is fitted with a bead breaker, a tool used to remove the tire bead seal with the rim, it was quickly found to be too weak to loosen the seal of the off road

test tire, so a more industrial strength bead breaker, driven by a worm screw, was also purchased for that task.

Using a standard steel wheel for instrumentation was not only troublesome to seal the final bead of the tire but also offered little room to instrument the wheel post first tire bead installation, so a bead lock wheel was purchased to solve both problems. A bead lock wheel is essentially a basic wheel that has one of the rim lips sheared off to weld a flange that has several tapped screw holes. An exterior lip with a corresponding number of screw holes is then used to secure the final bead of the tire, such that the bead is locked between the flange and exterior lip. This wheel was designed to secure the tire bead under very low inflation pressure, a condition often preferred in off-road applications. Conveniently, the welded flange has a shorter diameter than a conventional steel wheel lip; this provides more space to instrument the wheel. Both the tire changer and bead lock wheel are shown in Figure 4-12 and are in the process of being inflated, following sensor instrumentation.



**Figure 4-12. Bead lock wheel fitted on to the manual tire changer.**

The orange straps pictured in Figure 4-12 are tightened around the tire for precautionary purposes, in case of a tire blow out; this is possible if the bolts fastening the exterior lip to the rim flange are not torqued properly.

The mounts previously made for the sensors consistently had too much flex, so mounts fabricated out of hard plastic were made to give the sensors a more rigid base and add height to the sensors so that its measuring range has a higher voltage-distance resolution. A long brick of hard plastic was fabricated with a mill to ensure leveled dimensions of the mounts and to keep each mount nearly the same size. These mounts were attached to metal spacers and then finally attached to the sensors to give an added overall height of over 2 inches. The added height provided clearer data while also keeping the sensors at a safe distance from the inner tire carcass.

A new set of fasteners called the 3M™ Dual Lock™ Fasteners were purchased to provide a reliable, firm attachment between the sensors and rim. The new fasteners are composed of several small, mushroom-like plastics, which interlock with an audible “SNAP” between two strips to give a very secure connection. When interlocked, the fasteners become one flat and smooth piece, which is perfect for the sensor mount to adhere to and remain flush with the rim.

Making all the changes described in this subsection provided a relatively easy and secure method for attaching the sensors to the rim and was carried to the final design of the sensor system.

#### ***4.5 Quarter-Car Rig Validation Test***

Once the Mega was running a simple program to collect and log deflection data with the tire sensors, it was time to perform a validation test using the Performance Engineering Research Lab’s (PERL) Quarter-car rig. The Quarter-car rig is a rig made to fit various tire and suspension systems, which react to a ground input controlled by a hydraulic actuator. This rig was developed to investigate various suspension types and configurations among other countless areas of research. However, for the interest of this validation test, a rigid suspension will be used so that the only deformation occurring is at the contact patch. The Quarter-car rig fitted with the rigid arm attachment and test tire is shown in Figure 4-13.

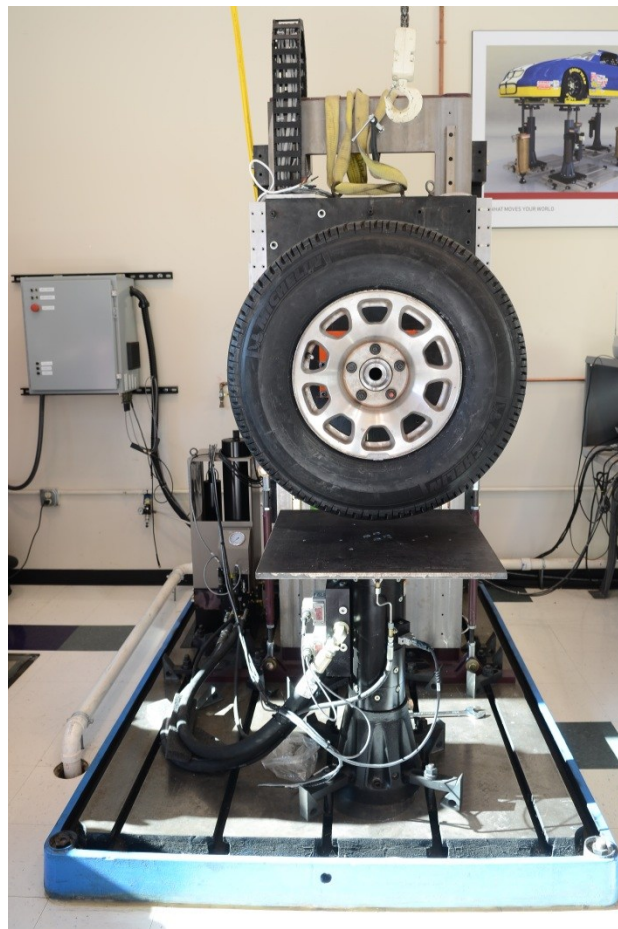


**Figure 4-13. PERL Quarter-car rig fitted with the rigid arm attachment and test tire. Photo courtesy of Anake Umsrithong.**

The hydraulic actuator of the rig has very precise control and can run several types of programs to simulate multiples conditions, such as a sinusoidal wave or ramp input, meanwhile collecting force and linear displacement data. The displacement and force response measured by the actuator was fed into a data acquisition system so that it could easily correlate with the tire sensor data in the analysis. Correlating the displacement data of the rig with the deflection measured by the sensors can validate how well the sensors are measuring the overall deflection and aid with understanding to what degree the tread elements deform, which is generally assumed to stay rigid in this study.

The validation experiment began with slow and steady step inputs for all functioning sensors. Four of the five sensors instrumented were collecting deflection data flawlessly, so all of the tests were administered on only those four functioning sensors. All tests would begin by elevating the hydraulic actuator so that it is was just touching the tire tread elements and not deforming it; this would serve as the baseline reference so that the input applied by the actuator is the actual deflection of the tire. Once set, the tire would be rotated to situate the desired measuring sensor normal to the contact patch. The test procedure administered to the sensors is as follows:

- Begin test with 4-5 increments of 10 mm.

- As the tire was observed to deflect substantially, deflection was reduce to 5 mm for a few more increments, then a few more times with increments of 3 mm
- Retract the actuator rapidly reduce for a short period
- Slowly return actuator to the baseline reference height.

The response for one of the sensors in a step input is shown in Figure 4-14.

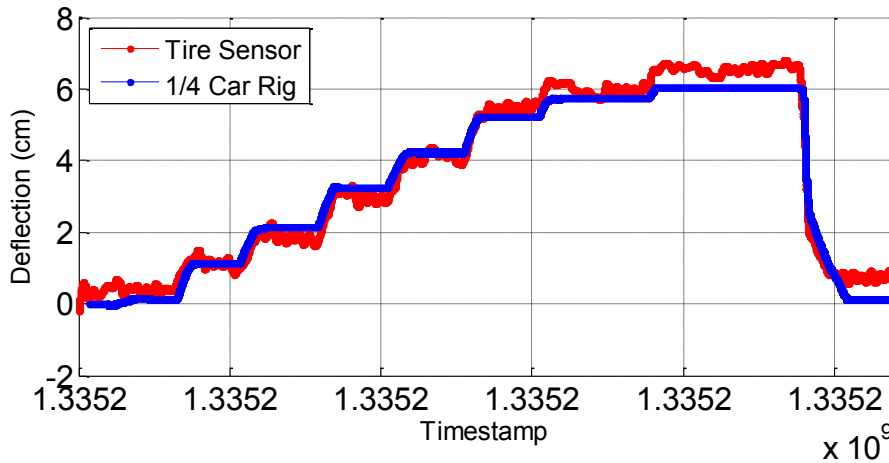


**Figure 4-14. Deflection reponse of the tires sensor and Quarter-car rig to a step input.**

The response of the tire sensors in comparison to the Quarter-car rig in Figure 4-14 shows that the tire sensors measure a near identical deflection response to the input displacement.

Sinusoidal waves of varying amplitude and frequency were used as input to the hydraulic actuator to investigate how the sensor system reacts to a dynamic input. The sensor that was consecutively measuring deflection with the highest resolution was utilized for these tests. The combination of amplitudes and frequencies tested are detailed in Table 4-2.

**Table 4-2. Sinusoidal wave properties applied as input by the Quartr-car rig.**

Amplitude (mm)	Frequency (Hz)
5	¼, ½, 1, 2, 3, 5, 10
10	3 & 10 (short bursts)

The deflection response of a tire sensor in comparison to the displacement input of a 5 mm sine wave at ¼ Hz by the Quarter-car rig is shown in Figure 4-15.

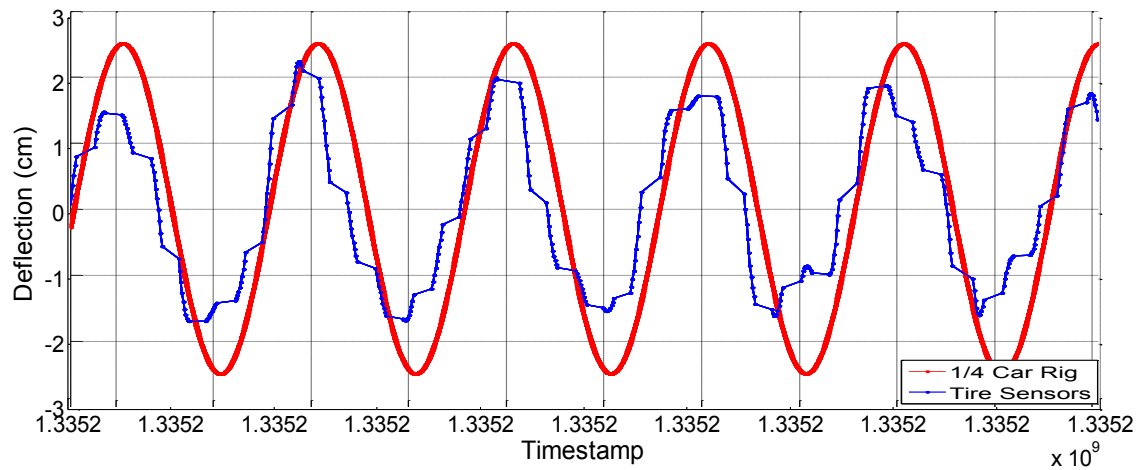


**Figure 4-15. Deflection response of the tire sensor and Quarter-car rig to a 5mm sine wave at  $\frac{1}{4}$  Hz.**

In the sinusoidal wave input, the tire sensor system does manage to measure the response of the input sine wave, but is not able to match the 5 mm amplitude of the wave, as it appears to miss the peak amplitude by 0.5 to 1 mm. This response is suspected to be attributed to several factors. The 2<sup>nd</sup> prototype mounts were used in this test which were not very well secured to the rim surface and were more than likely measuring the deflection at an offset. Moreover, these tests were administered while air was leaking out of the tire, so the tire carcass stiffness was expected to vary due to the wheel being repeatedly inflated throughout testing. The carcass stiffness can affect the deformation of the tread elements, which may have occurred during the tests. This is a result of the failed attempt to seal the wires being fed through the wheel to communicate directly with the sensors. Lastly, the wheel as a whole was observed to be moving in the vertical direction in response to the sinusoidal inputs when it should have been kept rigid. The wheel displacement observed is a result of the rigid arm connected to the wheel, undergoing bending during the testing. The rigid arm attachment is shown in Figure 4-16.



**Figure 4-16. Rigid arm attachment for the test tire on the Quarter-car rig. Photo courtesy of Anake Umsrithong.**

## 4.6 Wireless Implementation

After many failed attempts to seal the communication and power wires feed through the wheel, it was decided that to avoid the detrimental issue of an inflation pressure leak, the sensor system would need to go completely wireless. Making this decision requires that the tire sensor be completely standalone in that aspect of data collection, communication with the operator, overall review of saved onboard datasets, and transmission of datasets to the user with little loss of data over transmission. Additionally, the sensor system must have a reliable power source. Ensuring that these requirements are met for proper wireless functionality will be discussed in the following subsections.

### 4.6.1 Wireless Communication

Giving the operator digital logic and text command capabilities was of the highest priority for making the sensory system wireless. Because the XBee can be easily used to replace communication wires, the communication aspect of the system was not too difficult to implement. However, increasing the capabilities of the Mega program was required in order for it to handle several possible inquiries from the operator. The most important requests would be to tell the system to begin collecting data, to ask the system for a review of the data in storage, and to transmit saved data at the operator's request. The operator XBee and digital logic button circuit is shown Figure 4-17.

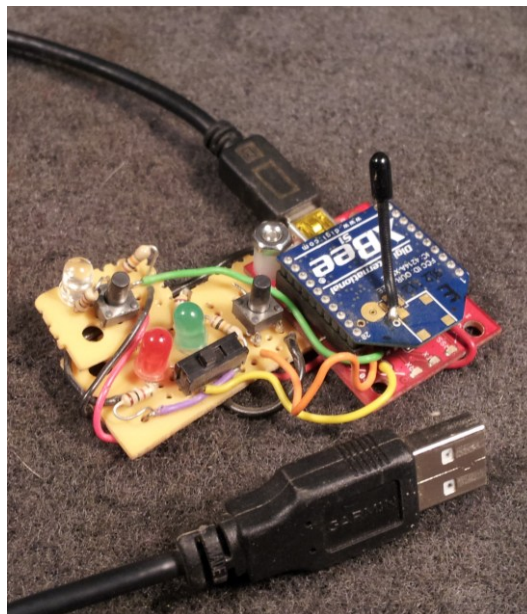


**Figure 4-17. Operator XBee and digital logic button circuit.**

The first step in making the system standalone is to make the Mega capable of fulfilling all the needs of the operator. Prior to implementing wireless capabilities, if the sensor systems were to be activated for data collection, the operator would send a simple string command and the program

would continue with the desired action. If the operator were to instead ask the system to focus on one sensor, rather than all, the Mega program code would require a slight edit; then, it would be recompiled and downloaded to the microcontroller. This cannot be done wirelessly so the need to develop a comprehensive, yet simple menu for the operator to view upon activating the system was of great importance. The programming logic and functions created to meet this requirement will be elaborated in a later subsection.

Once the programming logic was set, the operator would interact with the Mega by sending a number corresponding to the desired action, between 0-7, and the Mega would execute accordingly. Occasionally, the XBee of the Mega would not receive the message of the XBee connected to the operator's computer; this has been noted to usually occur when the operator XBee has been previously disconnected from the commanding computer. The use of digital logic proved to be a fairly reliable method of communication for instances of when the XBee will not respond to a text input.

The XBees are capable of Input/Output (I/O) line passing; this allows simply passing a digital signal between the XBee modules. Therefore, additional logic was added to the Mega code to receive digital signal inputs from the XBee to execute specific functions accordingly if text input was not responding. The signals to be sent from the operator are signals generated by a physical button that is connected to the operator's XBee. Pressing the button activates the Mega logic to wait for additional digital signals. Every additional depression of the button will be counted to represent the action to execute from the Mega main menu. This same concept is applied to controlling a relay that will supply power to the entire system.

#### **4.6.2 Power Supply**

Because of the wireless approach of the tire sensor system, great emphasis was placed into developing an efficient battery power supply so that the system can be used reliably and extensively between battery changes. In designing the power management system, four major components were fundamental to ensure efficient use of the battery supply, and are as follows:

1. Physical sensor to provide digital logic
2. Relay-logic circuit
3. Battery supply
4. Mega-XBee digital logic

The physical sensor component is what initializes the tire system to begin communication with the operator. The physical sensor is essentially a tilt switch that is connected to 3V battery supply. The tilt switch is oriented on the Mega such that when the wheel is rotated to a particular position, within the 2<sup>nd</sup> and 3<sup>rd</sup> quadrant of the wheel, it makes contact with the battery supply and acts as a 3V digital HIGH switch. This signal is what is used to trigger an H-Bridge relay circuit which

bridges the connection between the tire sensor system and the reserved battery supply. The H-Bridge relay circuit is placed on the data-logging shield to conserve space, as shown in Figure 4-18.

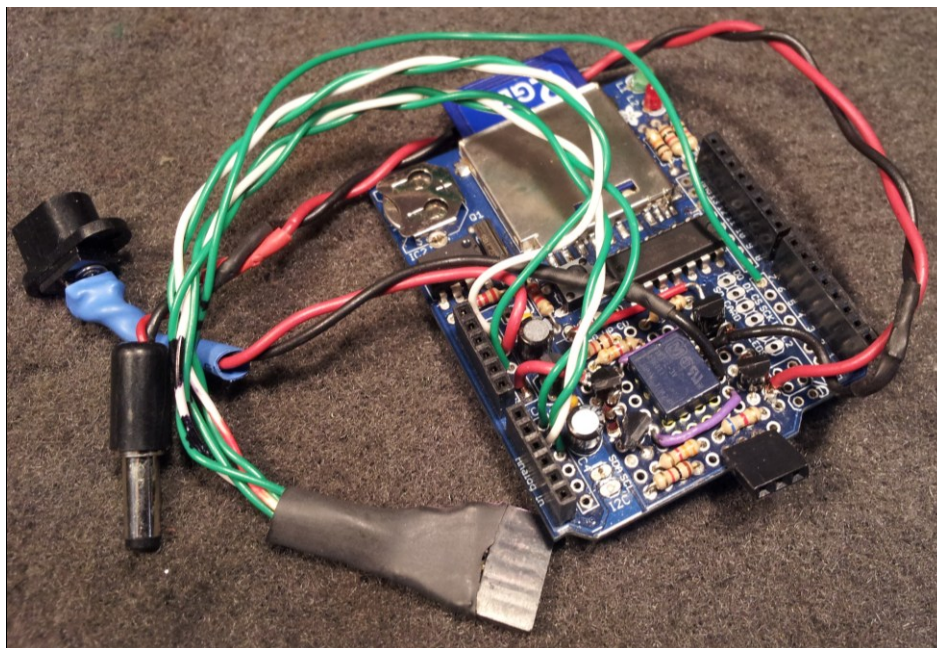


**Figure 4-18. H-Bridge Relay circuit used to power the sensor system.**

The battery supply consists of two pairs of six AA battery packs connected in parallel to provide an output voltage of 9 V. The Mega has an inlet voltage pin that accepts an input voltage between 7-12 V, so the 9V can be connected to provide power to the system. Although this is an easy, routine method of supplying power, a good portion of the power is wasted by the Mega's inefficient onboard linear voltage regulator. Therefore, to bypass the onboard voltage regulator, a 5V power supply can be connected to the 5V supply pin of the Mega. Employing this method requires a clean power supply because this input voltage path circumvents the Mega's overvoltage protection circuit. Therefore, a step-down switching regulator circuit was developed to accept the raw 9V of the battery and efficiently regulate the power to a clean 5 V supply to power the sensor system. The voltage regulator and battery pack is shown in Figure 4-19.



**Figure 4-19. Battery pack and voltage regulator used to power the sensor system.**

Once the system is powered on, the Mega's XBee module checks to see whether the operator has sent a command to communicate with the Mega or to see if a digital signal was sent to power off the system; otherwise, it idles until a response is received. If the operator would like to power off the system, the wheel will need to be rotated such that the tilt switch is within the 1<sup>st</sup> and 4<sup>th</sup> quadrant of the wheel. If not, the XBee and tilt switch will continue activating the H-Bridge relay circuit continuously until either the XBee or tilt switch power supply drains from frequently switching the relay. The tilt switch has the appearance of a small battery and is attached to the XBee shield as shown in Figure 4-20.

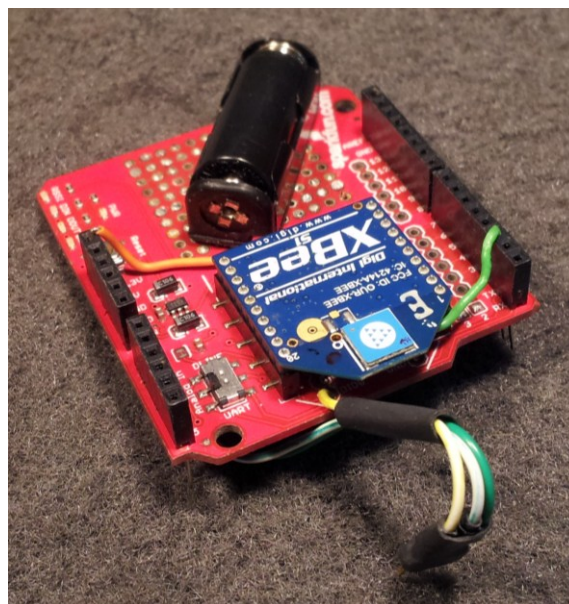


**Figure 4-20. XBee shield fitted with the tilt switch.**

The operator is able to power the system on or off by sending a digital HIGH or LOW signal to the Mega XBee using a physical one-way switch and I/O line passing. An additional push button is also connected to the operator XBee module to activate the reset pin on the Mega. Resetting the Mega simply terminates the running program in of the microcontroller and reinitializes the code.

#### ***4.7 Tire and Wheel Calibration***

Tire and wheel calibration was required to ensure that the tire carcass deflection measured by the system truly represented the deformation of the tire. Thus, the calibration required measuring the thickness of the tire tread and determining the relative position of each sensor to the wheel center and to the instrumented accelerometer.

Measuring the tire tread thickness, or more specifically, the distance between the inner liner of the carcass and the outside tread element extremity in contact with the ground, was a simple process. The thickness was measured by fixing one of the SHARP sensors on a bracket that pointed the sensor normal to a ground reference where data was collected. While keeping the sensor-bracket configuration intact, the bracket was moved to the rimless tire to place the sensor inside the tire and measure the inner carcass at the unloaded contact patch. Measuring the difference between the two determined that the tread thickness was approximately 2 cm.

Determining the relative distance of each sensor to the wheel center and accelerometer required instrumenting the wheel without a tire and placing it on the rig where it can remain suspended in the air at a known position. Beneath the suspended wheel was the baseline steel reference plate. The wheel was then spun at a slow rate to determine the point at which a sensor is completely normal to the plate, indicated by a maximum in the data. The distance between the wheel center and reference plate was measured by a ruler. Combing the sensor-plate data and the ruler-plate measurement gives the unique relative distance each sensor has with the center of the wheel. This data would also correlate with the accelerometer data collected at the time to give the relative position of the sensor to the accelerometer. Figure 1-18 shows this test being administered.



**Figure 4-21. Calibration test to determine the relative distance each sensor has to the wheel center and instrumented accelerometer.**

#### ***4.8 Final Design and WITS Capabilities***

Following the comprehensively redesigned Mega programming code, implemented wireless capability including power, validation and calibration, the final design of the tire sensors which go by the name of the Wireless Internal Tire Sensors (WITS) was complete and ready for testing the design of experiment for this study. Figure 4-22 shows the final diagram of the WITS, where eight sensors are equally spaced, each of which only using three of the five available IREDS. The reduction in IREDS was done because the added measuring range was not necessary considering how fast the wheel spins while testing.

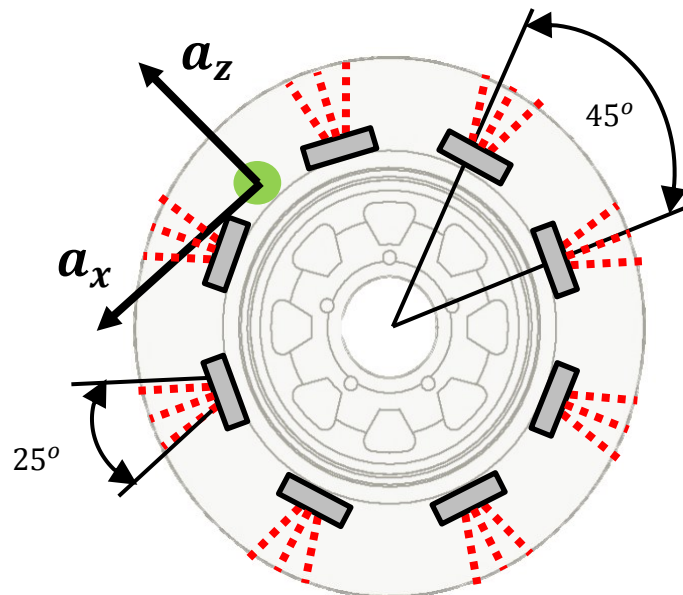


**Figure 4-22. Diagram of the final WITS arrangement inside the wheel.**

The ideal program to run on WITS during data collection was to let the accelerometer handle the measurements, as it is able to select the sensor approaching the contact patch and use it to collect data as it passes over the contact patch. The accelerometer control strategy follows an input text file, which details the angular position of each sensor and the ratio of the sensor's center IRED measuring range to the other IREDs of the sensor. Utilizing a text file allows the operator to make improvements to the code without having to reprogram the microcontroller. The sample rate can also be edited by the operator by using the same input text file of the accelerometer, titled ACCLRNGE.txt. The system can be commanded using either text commands sent through the operator's computer or digital signals set by the push button connected with operator XBee. The menu summary of the WITS system during activation is as follows:

- Collect data from all sensors –in random order
- Collect data from one sensor – user defined
- Accelerometer chooses sensors based on:
  - Code definition
  - Code definition, specifying IRED
  - ACCLRNGE.txt
  - ACCLRNGE.txt, specifying IRED
- Read/Define Sensor angular positions and Sample rate
  - i.e. , edit ACCLRNGE.txt
- Read SD contents – request file

Data collected by WITS is saved in a comma-separated value (CSV) format and can be easily ported to MATLAB for analysis. Every file written in the onboard SD card is of the format: “WITS\_XXX.CSV”.

An example of the output of the sensors is shown in Figure 4-23

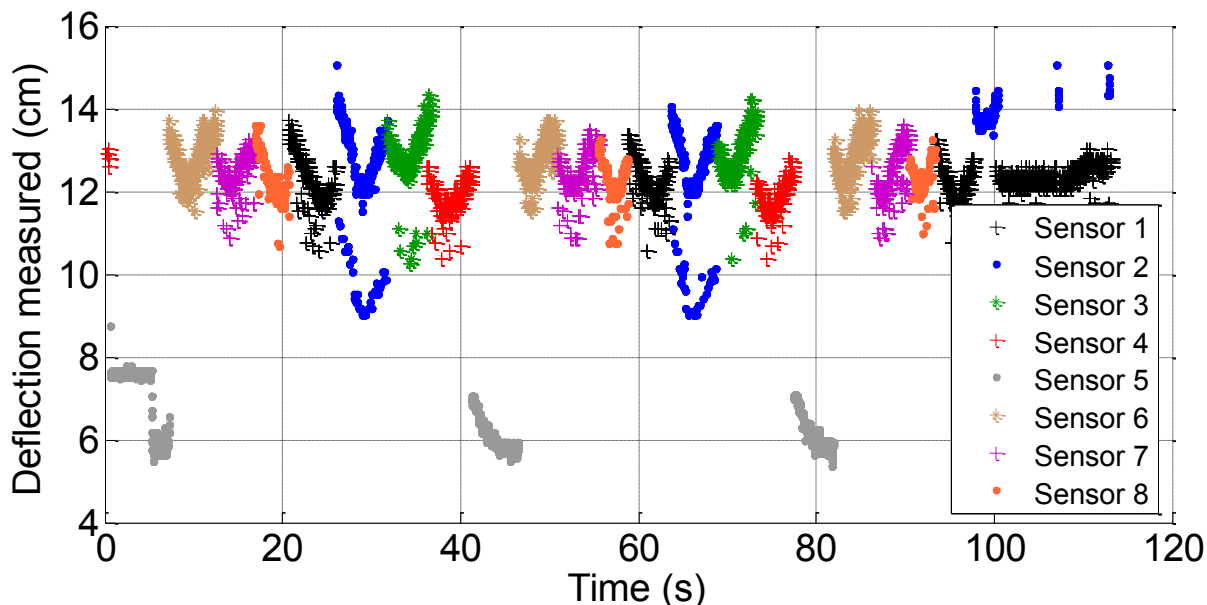


**Figure 4-23. WITS output from measuring the deflected tire radius in a test run of the DOE.**

The outputs of all eight individual sensors instrumented in the tire are shown in Figure 4-23. The valleys shown in the data of each sensor represent the sensor measuring the tire carcass deflection at the contact patch. It is at this point that data is sampled and used to estimate the rolling radius of the tire in the specific test run. The deflected radius measured is consistent for most of the sensors with the exception of sensor 5 (colored grey in Figure 4-23).

The final design of main WITS circuit boards are shown in Figure 4-24, which consist of the Arduino Mega, SD shield, XBee shield, and accelerometer. The optical sensors are attached to the wheel and connected with the wire harness which ultimately connects to the sensors to the Mega. The diagrams for all the circuit connections between boards and sensors and notes about the WITS use can be found in Appendix (D).



Figure 4-24. Main WITS circuit boards fully assembled in their final circuit design and connected to the accelerometer.

### 4.9 Determination of Tire Sinkage

The main motivation for developing WITS was to measure wheel sinkage. Sinkage determination is estimated from the synchronizing of data between WITS, the string pot data related to the wheel displacement, and overall soil height. The diagram shown in Figure 4-25 explains the need for the three sensors.

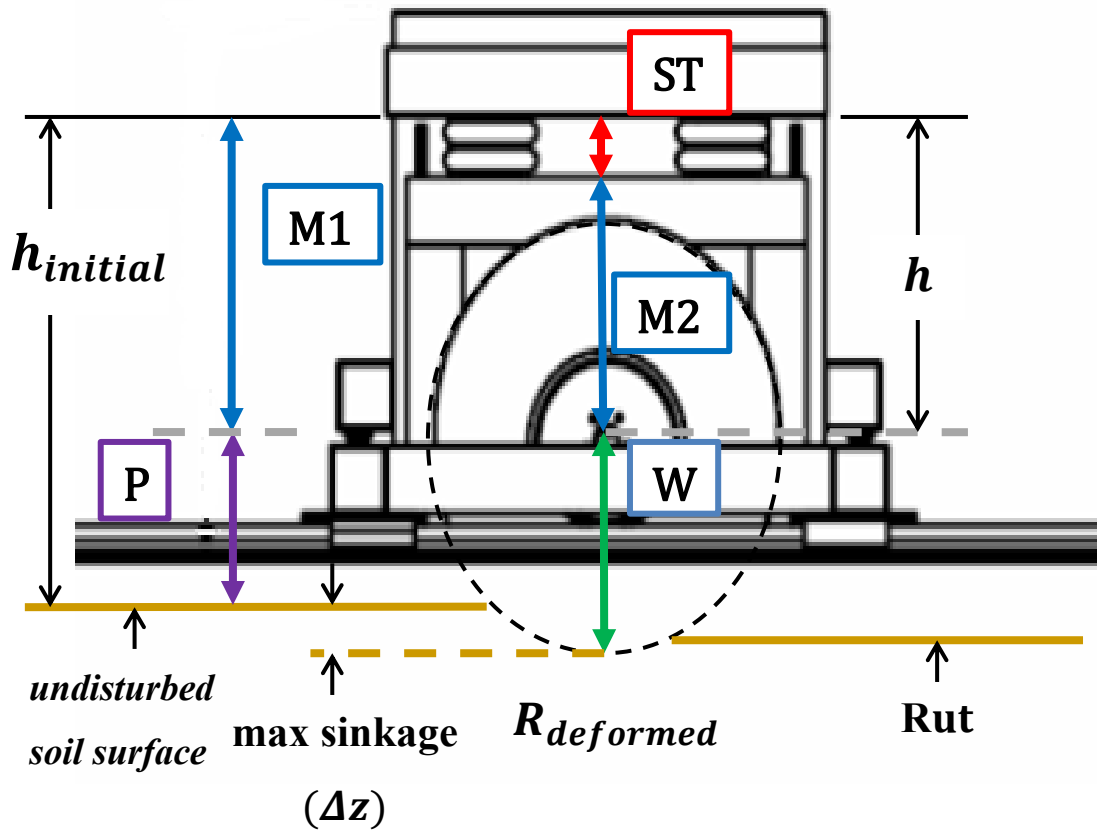


Figure 4-25. Diagram for sinkage measurements

To determine the max sinkage, the absolute difference must be taken between the undisturbed soil height and sum of the wheel displacement and tire deformation. This is shown below:

$$\Delta z = (h + R_{deformed}) - h_{initial} \quad (4.1)$$

$$h = ST + M2 \quad h_{initial} = M1 + P \quad (4.2)$$

Where  $h$  is the sum of the string pot measurement and constraint,  $M2$ , which is the distance between the wheel center and the top bar where the string pot is attached. The  $h_{initial}$  represents the distance between the measuring surface of the PING sensor and the same top bar ( $M1$ ) attached to string pot.  $R_{deformed}$  is the results of the WITS system, and  $M1$  and  $M2$  are measurements that were collected with the PING sensor. Because there is no form of measuring the tread element deformation, the tread is assumed to stay rigid in sinkage estimation.

A calibration of the sensors involved with this method of sinkage measurement was done on the baseline reference plate. This test resulted in an overall variation of 0.6 inches which is an acceptable level for this study. The variation is suspected to be attributed to measurement error, tread deflection, and the need to further validate the final WITS form.

## **5 Experimental Soil**

This section will discuss the experimental soil, soil preparation procedure, and laboratory testing administered on the soil for the purpose of soil property identification.

### **5.1 Soil Retrieval**

At the start of this study, the AVDL had used a silica-based lunar soil simulant of well-known properties for terramechanics testing [12]; however, to achieve variable real-world soil conditions, a sandy loam was selected as the ideal test soil for this study due to its flexibility in consistency depending on moisture content. The challenge of attaining a soil of sandy loam consistency was dependent on what the state of Virginia had to offer due to expensive interstate shipping costs and cross contamination concerns of soil foreign to Virginia.

A company known as Egypt Farms Inc. was discovered to have a sandy loam soil and offered to donate it to the lab in the interest of the study, yet with the exception of transportation costs. Egypt Farms Inc. is known for preparing custom soil mixes for golf courses, athletic fields, commercial landscapes, etc., and had conveniently opened a new distribution center in the western part of Virginia within the past few years. Although the donation was gratefully welcomed, it was important to take full advantage of the full 25-ton freight shipping cost of approximately \$ 1064.25. It was imperative to calculate the depth of soil needed so that the Terramechanics rig soil vane would not interfere with testing before making the final order of soil.

Following the results of the tire sinkage estimates explained in the subsection below, 7-8 tons of sandy loam soil was ordered and placed in the Terramechanics rig soil vane to be used in this study.

#### **5.1.1 Rough Tire Sinkage Estimation**

An allowable tire sinkage depth range of 4.0-12.5 inches, depending on the desired moisture content, was determined to be adequate in allowing a tire to sink within a sandy loam without any outside interferences of the Terramechanics rig. Because the soil vane can change from a depth level of 10-22 inches from below the top of the soil vane, the amount of sandy loam necessary can range from 6-9.4 tons with a density of 120 lb/ft<sup>3</sup>. This density was used as reference from the previous lunar soil simulant study on the rig [12]. This amount of sandy loam mass was determined to allow testing on a moisture content of approximately 15-51%. The amount of soil and predicted allowable levels of moisture content calculated were based on key assumptions made in a sinkage analysis; therefore, the actual minimum mass of sandy loam may vary but is expected to be within range of the estimations made.

The method of calculating the tire sinkage for tire rolling over sandy loam revolves around the use of a form of Bekker's pressure-sinkage equation:

$$p = \left( \frac{k_c}{b} + k_\phi \right) z^n \quad (5.1)$$

Where  $p$  is pressure,  $b$  is the smaller dimension of the contact patch (width in a rectangle area or the radius of a circle),  $z$  is the sinkage, and  $n$ ,  $k_c$ , and  $k_\phi$  are pressure-sinkage parameters.

The pressure-sinkage parameters used in the estimation of Table 5-1 were obtained from a table collection in Wong's text [3]; the table includes the values of the parameters for numerous terrain profiles. For sake of comparison, two terrain profiles of different moisture content were gathered from Table 5-1 below.

**Table 5-1. Terrain Profiles obtained from J. Y. Wong, *Theory of ground vehicles*, 4th ed. Hoboken, N.J.: Wiley, 2008. Used under fair use, 2013.**

Terrain	Moisture Content (%)	$n$	$k_c$ ( $kN/m^{n+1}$ )	$k_\phi$ ( $kN/m^{n+2}$ )
Sandy loam	15	0.7	5.27	1515.04
Upland sandy loam	51	1.1	74.6	2080

During the time of obtaining a test soil for this study, neither a test tire nor the intended test parameters had been selected, so the following parameters of a tire [3], shown in Table 5-2, were used in the max sinkage estimation.

**Table 5-2. Known tire parameters obtained from J. Y. Wong, *Theory of ground vehicles*, 4th ed. Hoboken, N.J.: Wiley, 2008. Used under fair use, 2013.**

<b>Vehicle</b>	Light truck tire
<b>Normal load</b>	3000-4000 lb (13.3-17.79 kN)
<b>Tire diameter</b>	20-22" (50.8-55.9 cm)
<b>Inflation pressure</b>	14.5-29 psi (100-200 kPa)

Because the tire is flexible, unlike a rigid wheel, when loaded, Bekker's equation can instead use the sum of inflation pressure ( $p_i$ ) and pressure due to carcass stiffness ( $p_c$ ) to represent pressure [3]. However, because pressure  $p_c$  is difficult to determine, as it varies with tire specific properties, inflation pressure and normal load, another method proposed by Bekker, utilize the average ground pressure ( $p_{gr}$ ) of a tire on a hard ground which is represented by the sum of  $p_i$  and  $p_c$ . These tire

parameters are usually proprietary information, so a tire of known properties in the literature was used.

The example tire used in the estimation was the 11.00R16XL tire; this tire has a diameter of 97.5 cm (38.4 in) and width of 28 cm (11 in) [3]. Although the example tire differed from the actual tire used in the study, it could give a rough estimate for the tire sinkage. The estimated sinkage results of the example tire would then be correlated with a smaller tire, as an assumed ratio of the tire diameter.

The average ground pressure of the 11.00R16XL tire can be obtained from Figure 5-1, which shows the relationship between inflation pressure and average ground pressure as it varies with normal load.

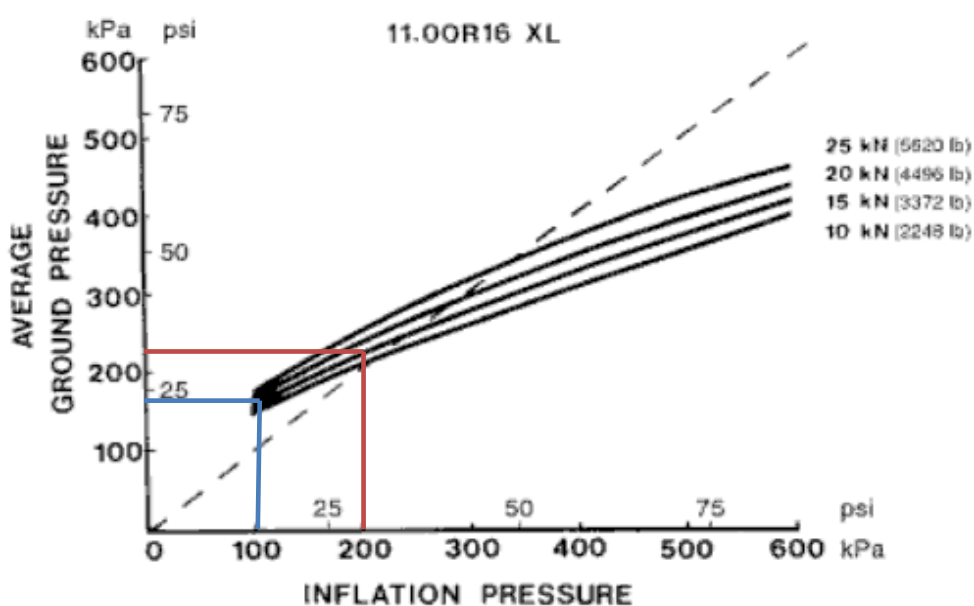


**Figure 5-1. Average ground pressure as a function of inflation pressure and normal load for the 11.0R16 XL tire, obtained from J. Y. Wong, *Theory of ground vehicles*, 4th ed. Hoboken, N.J.: Wiley, 2008. Used under fair use, 2013.**

For a constant normal load of 15 kN, an average ground pressure of 180 kPa and 220 kPa for an inflation pressure of 100kPa and 200kPa, respectively, were obtained from Figure 5-1. The inflation pressures were selected to be relatively low as this an interest of the study. Because these calculations were made to estimate the max sinkage of the tire and to determine the amount of soil required for testing, an assumption was made to relate the average ground pressure of the 11.0R16 XL tire to a smaller tire by the ratio of their respective diameters, which was of a 38.39 inch diameter tire to the 21 inch diameter tire used in the rigid wheel estimation. The ratio of the contact patch to the average ground pressure is set equal for the two tires in order to solve for  $p_{gr}$  of the tire of interest. The parameters used for computing the average ground pressure of the 21 inch diameter tire are shown in Table 5-3, along with the estimated average ground pressure.

**Table 5-3. Revised parameters for calculating tire sinkage of a deformable tire.**

Parameter	38.39 inch Dia. Tire	21 inch Dia. Tire
Contact patch length, $l$ (cm)	27.94	20.32
Contact patch base, $b$ (cm)	35	25.4
$p_{gr}$ at 100 kPa (kPa)	180	95.0
$p_{gr}$ at 220 kPa (kPa)	220	116.1

With the average ground pressure of both tires, terrain profiles presented in Table 5-1, and Bekker's equation, the max sinkage was estimated and presented in Table 5-4.

**Table 5-4. Tire Sinkage results for a flexible wheel.**

Moisture Content (%)	15		51	
	95	116	95	116
Avg. Ground Pressure (kPa)	95	116	95	116
$z_0$ for a 21in Dia. tire (m)	1.87	2.49	5.22	6.26
$z_0$ for a 21in Dia. tire (inches)	0.73	0.98	2.05	2.46
$(5 \times z_0)$ for 21 in Dia. (inches)	3.68	4.90	10.27	12.32

In Table 5-4, the final row lists the sinkage results as a multiple of five; this was added as a target due to a tire industry recommendation of multiplying the tire sinkage by a factor of five when testing on deformable soils. This is to ensure that no outside obstacles, such as the Terramechanics soil vane, interfere with the tire-soil interaction.

### 5.1.2 Amount of Soil Needed

The tonnage amount of soil required for the rig was computed assuming the sandy loam soil would have a density of 120lb/ft<sup>3</sup>, similar to the lunar soil simulant experiments previously performed on the rig.

The volume of the rig's soil vane can vary between two height levels; although the entire soil vane can be filled to give a third level of depth, that amount of sand would most likely be unnecessary. The first level allows a depth of approximately 20 inches measuring to the top railing of the soil vane. The second level allows a depth of 10 inches measuring to the top railing of the soil vane. Approximately 2-3 inches can be removed from both level depths so that no sand can fall from the top of the soil vane during testing.

The calculated minimum depth needed to prevent the soil vane from interfering with the tire-soil interaction of a 21 inch diameter tire was estimated to be between 4-5 inches with a moisture content of 15% or 11-12.5 inches with moisture content of 51%. If a low moisture content of 15-

30% is of interest, the max depth of sandy loam would be approximately 8 inches, so only the second level would need to support the soil. However, if a higher moisture content of 51% and up is of interest, the first level of the soil vane will be needed to support the soil for a minimum depth of 12.5 inches. The soil vane top surface area is 25 ft x 6 ft, so between the depths of 8 to 12.5 inches the sandy loam would occupy a volume of 100 to 156.3 lb/ft<sup>3</sup>. Therefore, approximately 6 to 9.4 tons of sandy loam would be required for the relatively low and high levels of moisture content.

## ***5.2 Soil Preparation Procedure***

One of the most important aspects of tire-soil testing is the conditions of the test soil. Over a period of time in tire-soil testing, the soil will deform and compact in unique patterns which will hinder the tire performance between test runs. Therefore, to reduce variation in tire performance and maintain consistent conditions, a repeatable soil preparation procedure must be employed prior to running a test. Five steps are involved in the procedure developed to prepare the soil and will be explained in detailed.

The main task of the first two steps of the procedure is to loosen the soil and remove it of any stresses that were induced from prior tire-soil interaction. The first step is to loosen the soil with a shovel. Because the depth of the soil was maintained between 7-8 inches, the shovel would be used to penetrate through the soil until it would reach the soil vane, then it would be lifted at an angle to relieve the soil of prior stresses. For the 3 ft wide by 16 ft long path of soil used in testing, the shoveling would be done three times along the width of the path and would be repeated between every 6-8 inches of the test path length. Once done, an electric tiller is used to further loosen and reduce any clumps of compacted soil to fine sand. The electric tiller used is shown in Figure 5-2.



**Figure 5-2. Tiller used to loosen the soil.**

The tiller is passed along the length of the soil path three times. It is important that the shoveling is done because the blades of the tiller are about 6 inches in diameter and cannot reach the total depth of the soil test path.

The main task of the third and fourth step is to level the soil surface in preparation of compaction. The third step requires raking the soil mounds, left by the tiller, smooth.



**Figure 5-3. Raking soil smooth**

Raking the soil smooth also helps to find voids of soil that need to be filled prior to passing the leveling blade. The smooth soil surface is then leveled in the fourth step with the leveling blade attached to the rig. Using the rig ensures that the soil height is level and consistent along the length of the soil test path.

Leveling the soil requires bringing the rig from its Home position to the Away position; once it has crossed that path, it can be attached to the agricultural roller to begin the fifth step of compacting the soil. The compaction step simply requires bringing the roller from the Away position, to the Home position, then returning the roller to the Away position of the rig, thus concluding the soil preparation procedure followed for a low level of compaction. The estimated time to complete this procedure is approximately 25 minutes. The entire trip of the roller results in a cone index reading of  $4.4 \pm 0.4$  kPa. This cone index gradient represents the first compaction level used in the final design of experiment. An example of the cone penetrometer test results for such a condition is shown in Figure 5-4.

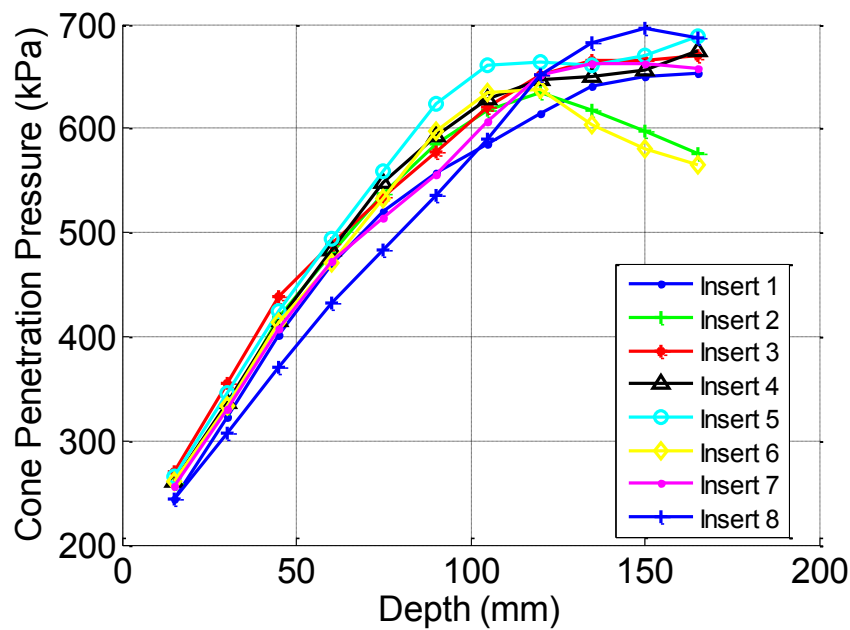


**Figure 5-4. Cone penetrometer test results for a low level of compaction.**

The various insertions shown in Figure 5-4 represent the separate cone penetrometer insertions collected at different lengths of the prepared soil path for one test run. The cone penetrometer measures a linear resistance for the first 4 inches of the prepared soil and either plateaus or decreases in resistance for the final 3-4 inches of the soil depth. This shows to what depth the soil preparation procedure affects the soil.

Moving the roller for an additional two trips, results in a high compaction level as shown in Figure 5-5. The additional trips add approximately 5 minutes to the soil preparation procedure.

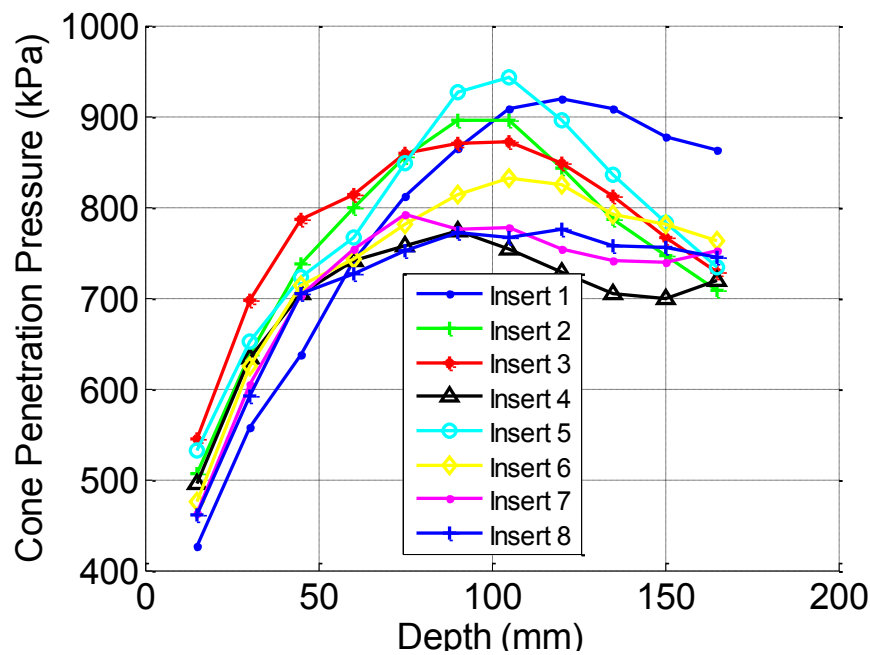


**Figure 5-5. Cone penetrometer test results for a high level of compaction.**

The additional two roller trips result in a nonlinear cone index gradient past the first 2 inches of the soil depth. The multiple insertions along the path of a single test run show that the results differ past 3 inches, which show the limitations of the soil preparation procedure.

### 5.3 Laboratory Testing

The only methods of soil measurement possible at the AVDL are the cone index and moisture content, both of which describe a condition of the soil from a trafficability standpoint, rather than providing a property of the soil. Therefore, in efforts to characterize the sandy loam soil and understand its properties under common test conditions administered at AVDL, a series of laboratory experiments were performed by a contracted geotechnical engineering company, Schnabel Engineering.

In collaboration with an associate of Schnabel Engineering and Jody Priddy, a Ph. D candidate of the Geotechnical Engineering Program in the Civil & Environmental Engineering Department of VT, laboratory tests were administered to characterize the soil composition, determine moisture-density relationship, and shear strength of the sandy loam soil.

Prior to performing soil laboratory tests, Schnabel Engineering conducted a nuclear density gauge test on prepared soil at AVDL to determine the average wet and dry density of the soil and overall moisture content. This density test was performed on soil that resulted in a cone index of  $4.4 \pm 0.4$  kPa. The nuclear density test revealed the results of Table 5-5 and measured at an average moisture content of 2.6%.

**Table 5-5. Nuclear density (lb/ft<sup>3</sup>) test results.**

Density( pcf)	
Wet	Dry
100.5	98
97.3	94.8
96.8	94.3
95.6	93.2
95.2	97.7
101.6	99

For general identification purposes, basic characterization of the soil type by Unified Soil Classification System (USCS) [47] and Department of Agriculture basic textural classification (USDA) [48] were conducted. In terms of USCS, the “sandy loam” soil used in this study was found to be more of a silty sand. Under USDA classification, the soil was classified as loamy sand. USCS classifies soils based on their performance characteristics as an engineering construction material, determined using grain size distribution and plasticity characteristics, whereas the USCS classifies based on texture and grain size.

A test known as the Standard Proctor compaction test [49] was conducted to determine optimum moisture content-density relation of the soil. This test revealed that the soil was able to exhibit a maximum dry density of 120.3 lbs/ft<sup>3</sup> at a moisture content of 8.8%. There was an initial interest in including a change in moisture content in the design of experiment; however, it was quickly discovered that maintaining and measuring the moisture content of the soil was a difficult and tedious process.

To measure the internal shear strength of the soil, a triaxial compression test [50] was administered. This test was conducted while the soil was unconsolidated and undrained. The analysis of this test follows the Mohr-Coulomb failure criterion and revealed that the soil has an internal friction angle of 17 degrees and cohesion of 1.4 psi. These are parameters commonly used for modeling the plasticity of a soil.

## 6 Design of Experiment

This chapter will go over the parameter selection for the design of experiment, the procedure followed for each test run, the reflection of the initial design of experiment, and the final design of experimented utilized for this study.

### Parameter Selection

Choosing test parameters that are commonly found in real-world conditions and can be replicated in the Terramechanics rig were the primary focus in developing the design of experiment parameter matrix. Parameters utilized were to range between tire and soil parameters that, in theory, are expected to have a drastic effect on the tire-soil interaction. In review of the rig's capabilities, the tire can be tested at various slips and normal loads; these toe and camber angles were held constant at neutral zero angles. To give the normal load controller ample time to react to soil height variation, a speed of 7.5 cm/s was selected as the constant longitudinal speed of the carriage. The tire inflation pressure can be easily adjusted to an accuracy of 0.5 psi. The main factors that influence soil properties are the moisture content (MC) and compaction. Therefore, the main parameters of interest for the design of experiment are wheel slip, normal load, tire pressure, soil compaction and moisture content.

Considering that five parameters were to be investigated, the number of levels for each had to be chosen within a reasonable range that would show respective parameter effects and keep test runs at a realistic number. At least two levels, termed level one and two, for each parameter, were to be tested. Bearing in mind that tire performance varies greatly with wheel slip, especially in the lower slip region, eight slips values were selected to be tested. Due to the non-linearity in drawbar pull at low slip, most levels were to belong in the lower slip region than compared to the high. Moreover, as high slip percentages are of interest to the military, at least 90% slip was also to be tested.

#### 6.1.1 Test Tire

The selection of the actual test tire and tire parameter levels were inspired by an actual full-sized instrumented off-road vehicle. Having a similar test setup for the rig as that of a full-size vehicle offers the tremendous opportunity to correlate test data as the rig is limited to test at low speeds. Fortunately while shopping for an ideal off-road tire, Dr. Schalk Els of the University of Pretoria (UP) South Africa acquired Michelin-brand tires, purchased in United States, to test on his Land Rover Defender 110 [51] and suggested the AVDL purchase the same so we can correlate test results in the future. Thus, the LT235/85R-16 Michelin LTX A/T 2 E tire was selected as the test tire for this study.

To minimize variability of tire structure due to age and origin, the Michelin LTX tires were purchased. Two identical Michelin tires were purchased so that one tire could be dedicated to testing on the rig while the other was used for further laboratory testing to collect tire structure specific parameters. According to the U.S. Department of Transportation (DOT) code stamped on the tire sets of UP and AVDL, both were deciphered to have been manufactured in the same facility while differing by only ten weeks of age. Figure 6-1 shows the tread pattern of the tire.



**Figure 6-1. Michelin LT235/85R-16 LTX A/T 2 E test tire tread pattern.**

Considering that the same tire as UP would be used in this study, it was natural to choose the Defender’s wheel load and common tire pressure as a baseline test level. The data received from UP indicated that the measured normal load for the left-front tire of the test vehicle, while vacant, is 505 kg (1113 lb.) with a tire pressure of 200 kPa (29 psi). Further details of the instrumented Defender are shown in Table 6-1. It’s important to get the vehicle weight for that particular wheel due to the fact that the rig is normally calibrated as the left-front tire of a vehicle. This is further explained in the **Error! Reference source not found.**for operating the rig.

**Table 6-1. Specifications of the instrumented Land Rover Defender 110.**

Wheel Specific Weights (kg)	Left	Right
Front	505	596
Rear	608	590
Combined Weight	2299	
Tire Pressure (all)	200 kPa	

For the sake of testing at an additional level that intuitively seemed to increase tire performance, the second level of both parameters were chosen to be approximately 10-20% higher for normal load and lower for the tire pressure. Simply put, the second level for normal load and tire pressure would be 1349 lb (6 kN) and 26 psi (180 kPa), respectively.

### **6.1.2 Soil Parameter Levels**

The soil parameter levels were selected based on our lab capability of achieving them in a repeatable manner, in a reasonable amount of time, by one person. Recall from the soil preparation procedure detailed in Section 5.2, that soil compaction is achieved through the use of an agricultural roller. One method of increasing the compaction level would be to add weight to the roller, such as through the addition of water. However regulating change in the weight of the roller would become difficult due to the unsealed, odd shape and size of the roller for weight measurements. Leakages could also happen and a randomized design of experiment would be difficult to achieve. Thus, using the roller for an extra two trips turned out to be an easier and more consistent method of applying a higher level of soil compaction.

One trip of the roller consists of bringing the roller from the Away to the Home position, then returning the roller to the Away end of the soil vane; one trip results in a compaction gradient of  $4.4 \pm 0.4$  kPa. With the addition of two trips, the compaction gradient raises to  $6.5 \pm 0.9$  kPa. It should be noted that although this method does change the soil compaction in a consistent manner, the resulting compaction is dependent on soil moisture. Thus, the actual compaction process is what is controlled in the experiment, rather than the soil compaction level, although cone penetrometer tests are being used in order to ensure consistency in soil compaction.

The water content dependency of soil compaction is the actual inspiration for the chosen levels of moisture content. The first level of moisture content was established after Schnabel Engineering visited the AVDL twice to conduct in situ soil condition measurements of prepared soil. During each visit, the soil was prepared with two different levels of compaction, where the entire length of the soil vane was compacted with the roller and one half of the soil was further compacted with a tamper. Once it was found that the tamper made no difference to the soil compaction the soil moisture was increased per the advice of Schnabel Engineering. The added moisture will allow the soil to become more cohesive and thus maintain a compaction level. After applying a small amount of water to the soil, the new initial level of moisture content was brought up to an average of 2.6%. Following the laboratory soil testing done by Schnabel Engineering, the highest achievable density of the soil was found to occur at 8.8% MC, thus this value became the second parameter level for moisture content. More details about these values can be found in the Section 5.3.

### 6.1.3 Initial Design of Experiment

Following the selection of the previous subsections, the initial design of experiment parameter matrix is shown in Table 6-2. Testing one slip value per run was the path to take in this design of experiment due to the small amount of consistent drawbar pull data recorded within each test run. From this parameter matrix, following a full factorial design would require 128 trials plus an additional two runs per trail for statistical purposes, totaling to 384 runs. Considering that each test run requires an average of 30-40 minutes to administer, the full factorial design was too unrealistic, so a more concise two stage design of experiment was pursued. The two stage design would require the initial stage of testing be done on the extremities of each parameter and determining those of which make the biggest impact on the results. The second stage would then go into further testing that focuses primarily on the parameters which have greater influence on tire performance as a result of the findings from stage one.

**Table 6-2. Initial design of experiment parameter matrix.**

Parameter	Levels							
	1	2	3	4	5	6	7	8
Slip (%)	0	5	10	15	20	40	60	90
Normal Load (kN)	5	6						
Tire Pressure (psi)	29	26						
Soil Compaction (kPa/mm)	4.4	6.5						
Moisture Content (%)	2.6	8.8						

## 6.2 Experimental Procedure

A consistent experimental procedure was followed for each test run to stay time efficient between runs and reduce experimental error and fatigue on the operator. For an ideal day of testing, the listed steps were followed: 1) initialize and warm up all equipment, 2) prepare soil as needed, 3) ready all instruments, 4) collect data, then repeat steps 2-4 per run while occasionally administering step 1 in between every few runs. These steps will be further described in this section.

The first step includes the initialization of the rig equipment, test tire, and soil for a full day of testing and warming it up for the first run. This starts by turning on all the rig computers and supplying power to the rig motor controllers as detailed in the appendix of Taylor’s thesis [12]. At this point, communication and functionality of the Wireless Internal Tire Sensors (WITS) system in the tire is confirmed, if not, the tire is to be dismounted and batteries are either replaced or recharged.

Once the tire is mounted on the Kistler sensor, the rig is set to warm up by spinning the tire at 2 rad/s for 15-20 minutes. This is required as the piezoelectric sensors in the wheel hub are sensitive to time and temperature changes. Once the rig has had time to warm up, the Kistler sensor is calibrated to be ready for testing. This step is actually done in conjunction with step two, so that while waiting for the rig to warm up, the soil can be prepared as needed, for example, when adjusting the desired moisture content. The calibration step is repeated after every few test runs as the operator can see from the Kistler laptop emulator that the sensor readings tend to drift.

Once a day of testing has begun, the second step becomes the first step in the iterative experimental process. The main objective of this step is to prepare the soil according to the procedure detailed in Section 5.2. This procedure is followed while adjusting the moisture content (MC) to help guarantee consistent water distribution. Once the soil has been prepared, the soil compaction resistance is measured with the cone penetrometer and 2-3 samples of soil are collected and sealed for later MC testing. The MC can vary throughout a day of testing so it is frequently measured and adjusted every four, or so, runs.

The third step requires readying all the sensors of the tire and rig for data collection. First the tire is rotated to trigger the WITS system to confirm communication; the wheel is then lowered to the Home steel plate and freed from the winch. In efforts to reduce the computational load on the main rig computer, the operator's laptop, positioned on the carriage, is used to communicate with the WITS system and soil height reader. Therefore, while the WITS system connectivity is confirmed, the same is done for the soil height reader. Because the soil height reader is hardwired to the host computer, connectivity remains secured after the first connection is confirmed. Returning back to the rig computers, the procedure for applying a normal load **Error! Reference source not found.** is followed and set to the desired load. Once the slip speeds are adjusted in the motor control program and the data acquisition program is armed, the rig is ready for a test run.

After all instruments are readied for testing, the fourth step is to set the rig in motion and collect data. This starts out by setting the LMS software to collect data, and setting the WITS system and soil height reader to collect data. The rig is next activated to conduct the test run. With a longitudinal speed of 7 cm/s to roll past a prepared path of over 4 meters, the rig takes over a minute to collect data. To be time efficient, some of the soil samples can be weighted and put in the microwave to measure the MC while still supervising the rig. Once the rig has reached the Away end of the soil vane, the data acquisition for the rig, WITS and soil height reader is completed and saved. The normal load program is then terminated and the wheel is raised with the winch high enough to be above the soil. As the carriage is returned to Home, the wheel is rotated so that the WITS system is in a position that the ball trigger can remain in the OFF position to conserve battery power.

Once a single test run has been administered, repeating steps 2-4 should suffice for most of the data collection. After a few runs, the Kistler data tends to drift a fair amount, so the sensor is recalibrated as mentioned in step 1.

In summary, the experimental procedure used in this study is as followed:

1. Initialize and warm up all equipment.
  - a. Turn on all computers, programs, and power supply to rig.
  - b. Confirm functionality of WITS and replace batteries if needed.
  - c. With the tire mounted, warm up the sensor by spinning the wheel at 2 rad/s for 15-20 minutes.
  - d. Just before collecting the first set of data, calibrate the Kistler sensor while the wheel is spinning, follow the procedure detailed in the appendix of Taylor's thesis [12].
2. Prepare soil.
  - a. Follow soil preparation procedure detailed in Section 5.2.
  - b. If first test of the day, confirm MC, readjust as needed and repeat the soil preparation procedure.
  - c. Collect cone penetrometer data and 2-3 soil samples for MC testing.
3. Ready all instruments.
  - a. Activate the WITS system and lower the wheel onto the initial test platform.
  - b. If not done already, confirm connectivity with the soil height reader.
  - c. Return to rig main computer and apply the desired normal load according to the procedure detailed in Appendix (E).
  - d. Confirm the appropriate slip values are set for the test run.
4. Collect data.
  - a. Set LMS software, WITS, and the soil height reader to begin collecting data
  - b. Activate rig to conduct test
  - c. While rig is running, measure MC of soil samples using the microwave heating method.
  - d. When rig completes run, stop and save data collection.
  - e. Raise wheel above soil level and return the carriage to the Home position.
  - f. Rotate wheel to keep WITS in an OFF position.
5. Repeat steps 2-4 per run while occasionally administering step 1 in between every few runs.

### 6.3 Reflection of Initial DOE

Once a good amount of data was collected, it was important to see how the data was looking for the first stage of testing and what parameters would require most attention on the second stage of testing. However, in review of the data, the parameters had either a drastic effect or none at all, especially after looking at data past 5% slip. After closer review of the wheel speed data for a full set of testing, it became very evident that the rig was not applying the desired slip changes past 5% slip. It also became clear that the soil moisture content was difficult to regulate and had a big impact on the tire-soil performance.

#### 6.3.1 Inconsistent Slip Change

Quickly after testing one slip value per run, it became evident that this method would take too long to complete the design of experiment, so introducing a slip change halfway through the test path was investigated. This method appeared to be working fine according to the motor control program (PiCPro) and some of the test results as shown in Figure 6-2, where a slip change of 0 to 5 % occurs between the 72nd and 74th seconds, with all parameters set to the first level.

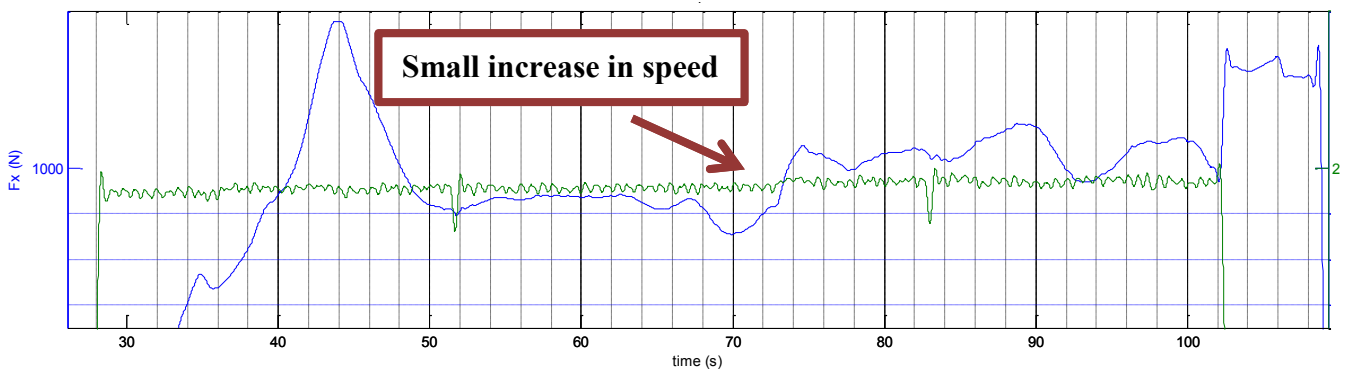


**Figure 6-2. Test run of a 0-5% slip change with all parameters set to level one. Blue curve represents the measured longitudinal force. Green curve represents the speed of the wheel.**

However, the slip change did not appear to be consistent for other slip changes, primarily in the higher slip ranges and occasionally in the lower range. Upon further review of all the 24 runs collected for the level 1 condition of the DOE, it appeared that the rig made no slip changes past 5% slip. This can be seen in Figure 6-3 as the measured wheel angular rate for all runs is plotted against the ideal angular rate of the wheel for an average speed of 7.5 cm/s and estimated radius of 37 cm.

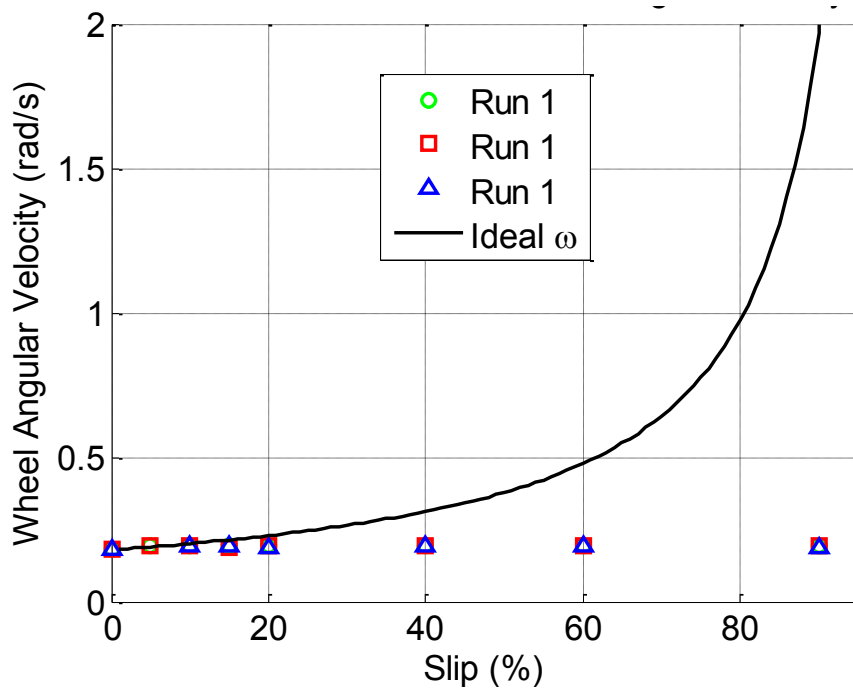


**Figure 6-3. Comparisons of ideal and measured wheel angular velocity collected for three runs under the level 1 condition for all parameters.**

As a result of seeing no slip change past 5%, a simple benchmark test was done to investigate wheel speed variation with the wheel loaded versus unloaded. For a more comprehensive plot, the test was set to change between eight slip values rather than two. This is not how an ideal test run would be administered but it can still provide meaningful wheel speed data. As shown in Figure 6-4, the motor control cannot maintain a slip change past 5% slip.

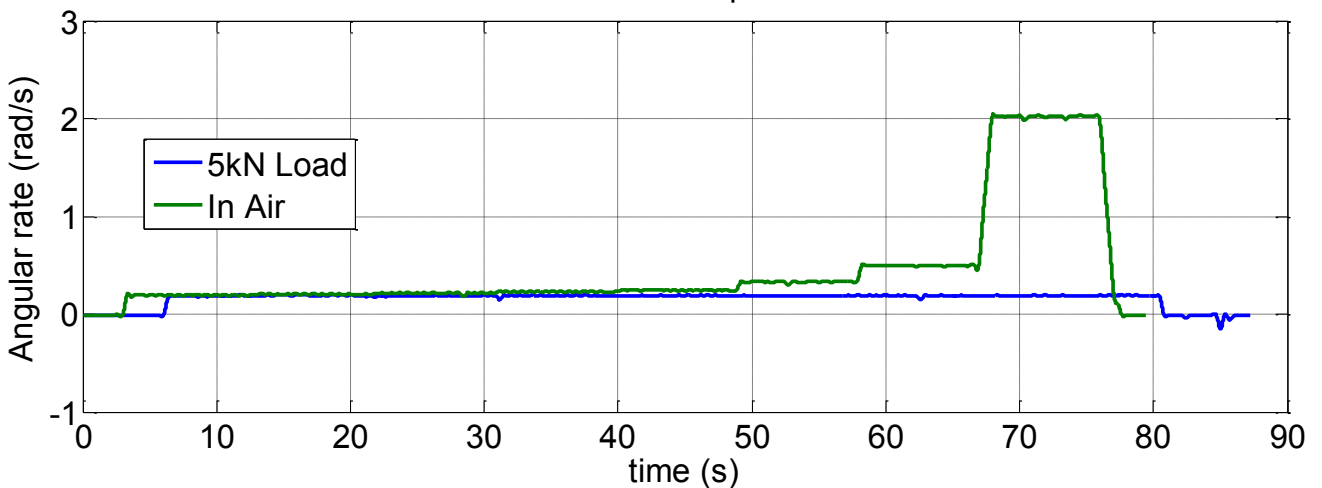


**Figure 6-4. Angular rate comparison of a wheel crossing a 4 meter soil path while applying 8 slip changes (0-5-10-15-20-40-60-90%) with either a loaded or unloaded wheel.**

Upon further review of the code used to control the motors, a low limit on the current draw of the wheel motor was found to be the culprit of the inconsistent wheel slip problem. Once this value

was changed in the code, the motor was able to achieve the desired slip with little error. This is a result of the code modifications discussed in Section 3.2.2.

### 6.3.2 Small and Large Impact of Parameters

Although the data collected from the initial stage of the DOE does not account for slip higher than 5%, the relative parameter difference between data is evident. The parameter found to have a prominent effect on the tire-soil interaction is the moisture content of the soil. Not only did the MC have a great effect on tire performance but it was also difficult to maintain constant. Figure 6-5 shows the normalized drawbar pull versus slip comparison of two runs collected under the condition of all parameters held to level one with the moisture content raised to level two.

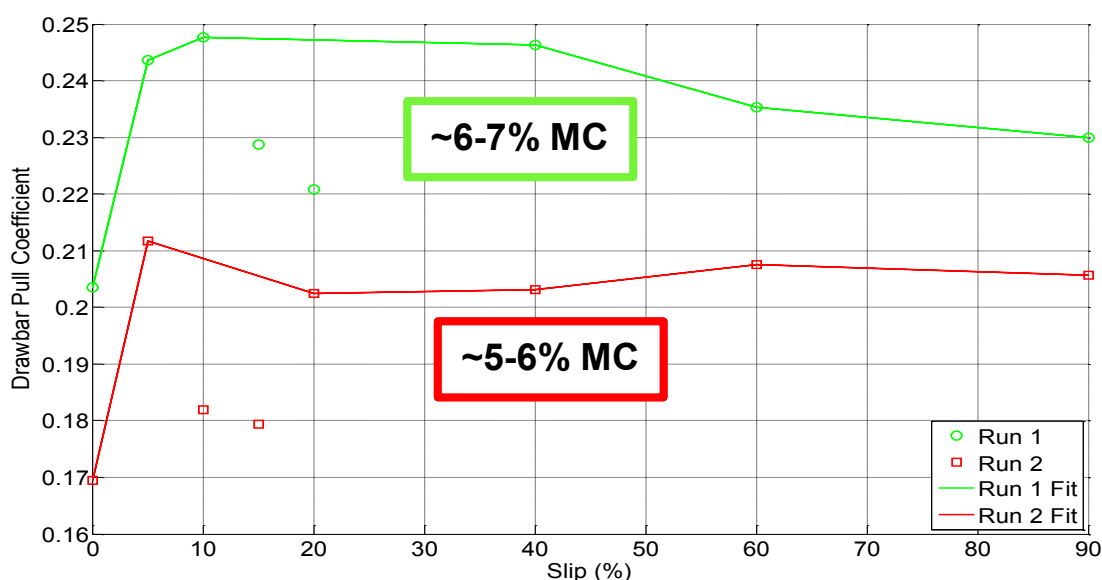


**Figure 6-5. Comparative plot of the normalized drawbar pull vs slip collected of two runs under the level 2 MC condition. Outliers are a result of separate days of testing.**

Figure 6-5 not only shows the difficulty of achieving and maintaining a constant MC but also shows the sensitivity of the tire performance as the result of a change in fraction of MC. Although the goal of the second level MC was 8.8%, achieving this level was found to be very difficult and time consuming, which led to the resulting 5-7% MC condition recorded. The process of adjusting the MC was found to not be as straight forward as anticipated, thus resulting in hours' worth of effort to readjust MC before being able to continue with a test run. However, when 8.8% moisture content was measured from initial soil preparation, after measuring more samples taken during testing, it would turn out that the 8.8% was a false reading due to uneven water distribution. The varying MC is not only a result of disproportionate water application to the soil but also from evaporation and drainage as a result of repetitive compaction from soil preparation and tire testing. Because of the difficulty and inconsistency of the high level MC, testing a second level of MC was abandoned in the

second stage of the design of experiment. These results also influenced purchasing a higher accuracy weight scale and a vast amount of glass vials to collect soil samples for every run, rather than every few runs as done originally. Testing with an additional moisture content level will need to be revisited in the future but with a faster method of MC testing and thorough process of regulating the applied water.

A parameter that was found to have little impact on the tire performance was the inflation pressure. The little difference observed is believed to be the result of the small 10% change in tire pressure for the second level. This can be seen in the comprehensive plot of Figure 6-6 displaying normalized drawbar pull response versus slip of all parameters tested in five different conditions. The curve termed “Lvl 1” indicates that all parameters were held at the initial level and “Lvl 2 [Parameter]” indicates when one parameter is changed to the second level while all else were kept at the first level.

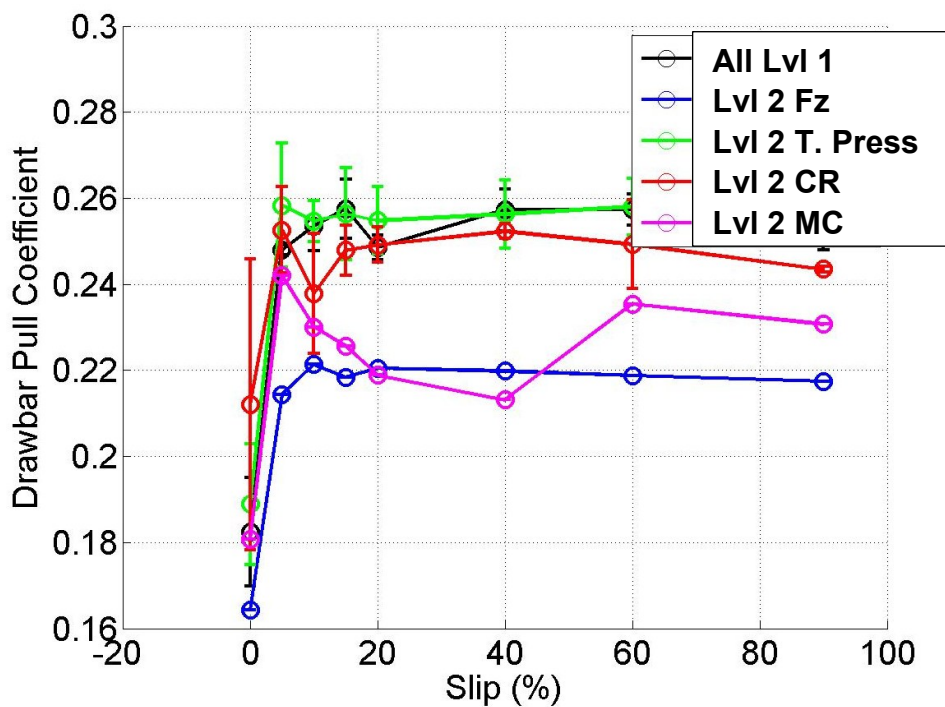


**Figure 6-6. Comprehensive plot displaying the impact of several parameter changes on the normalized drawbarpull response.**

Figure 6-6 shows the near nonexistent difference of a small pressure change when comparing the drawbar pull response of the second level of tire pressure (green curve termed “Lvl 2 T.Press”) to the response of all parameters kept at the initial level (black curve termed “All Lvl 1”). This result influenced the decision to try a smaller inflation pressure for the second stage DOE. Also note the large variation in the drawbar pull response related to a higher, yet inconsistent MC show in Figure 6-6.

## 6.4 Final DOE

Learning from the results of the initial DOE helped to develop the second stage DOE which was utilized for the data collected and presented in this document. Following the modification of the motor control program to allow slip changes past 5% slip, the final DOE would include data collected while applying four slip changes per run, rather than the previous one to two slip changes. This change would not only drastically reduce the time and effort required to collect data per condition but would also reduce variability in moisture content between tests. With the initial DOE, testing one condition would take between 2-3 days of testing thus giving the MC of the soil plenty of time to evaporate and drain throughout testing. However with the final DOE, testing one condition would take less than a day of testing.

Applying four slip changes within a single run is not expected to make a grave impact on the tire performance because the tire will have at least one meter of prepared soil to travel between slip changes. This assumption is taken as a result of the work of Woodward who confirmed that for a distance of 0.5 to 4.8 meters traveled by a loaded, treadless pneumatic wheel on a lunar soil simulant had no effect on the tire performance [7].

Additionally, considering the effects of moisture content and inflation pressure, respectively, these parameters were changed in the final DOE. MC was ruled out of the DOE to focus primarily on parameters that were easy to change and test in a randomized order. The tire pressure was reduced by over 30% to an inflation pressure of 20 psi.

Furthermore, after the first few test runs, it becomes evident that the tire would sink significantly in the soil when spinning at 90% slip. Having a great depth of sinkage conflicts with the boundary layer of the sinking tire; therefore to reduce tire sinkage, the highest slip value was lowered to 75%. All the described changes to the final design of experiment are shown in Table 6-3.

**Table 6-3. Final design of experiment parameter matrix.**

Parameter	No. of Levels	Range	
		L1	L2
Slip %	8	0 – 5 – 10 – 15 – 20 – 40 – 60 - 75 (or 90)	
Normal load (kN)	2	5	6
Inflation Pressure (psi)	2	29	20
Compaction Resistance (kPa/mm)	2	4.4 ± 0.4	6.5 ± 0.9

## 7 Experimental Results and Discussion

This section will discuss the results of the final design of experiment. The main responses analyzed are the drawbar pull performance and sinkage of the tire. The section will begin with discussing the filtering and data processing applied to the raw data collected. The analysis of the responses with respect to one parameter level change of the DOE and several parameters level changes (two to three parameters) of the DOE will follow. Then, a graphing statistical approach will be presented on the effects and interactions of the parameters in the DOE.

### 7.1 Data Processing Method and Baseline Analysis

Each test run collected in this study was organized with the LMS Test.Lab software used for data collection and an experimental journal kept in Excel. The data collected in LMS was extracted into a bulk text file and then ported into a data structure for further analysis in MATLAB.

The experimental journal organizes the WITS file names, cone penetrometer and moisture content data and provides the randomized order to collect data within each respective condition of the DOE. The journal also provides the wheel speed values used as input for wheel motor control. The wheel speeds per condition of the DOE were considered unique under the assumption that each DOE condition would induce a change in the wheel rolling radius. Therefore, prior to performing a full set of testing for a specific DOE condition, a low slip test run was done at a wheel speed considered to provide a near-zero slip scenario. The tire deflection data collected from the low slip test would then be analyzed to determine the rolling radius that would be used for the tests run of a specific DOE condition.

The overall analysis for both the drawbar pull and sinkage data was done in MATLAB. Data noise from the Kistler sensor was filtered out with a low pass filter prior to the analysis. A fourth order Butterworth digital low pass filter was applied with a cutoff frequency of 2 Hz, this filter was observed to adequately clear out noise and maintain the integrity of the signal. From this point onward, the data between each run was plotted against each other to determine when the wheel reached steady-state between slip changes and was consistent among the runs. Data is then sampled from the steady state region and is processed further to provide the results of this study.

Figure 7-1 gives an example of the normalized drawbar pull collected for the DOE condition of all parameters held to level one. Note that the normalized drawbar pull, also known as the drawbar pull coefficient, is used in the analysis because it is a commonly used response to determine tire performance and can compensate for slight normal load differences between runs.

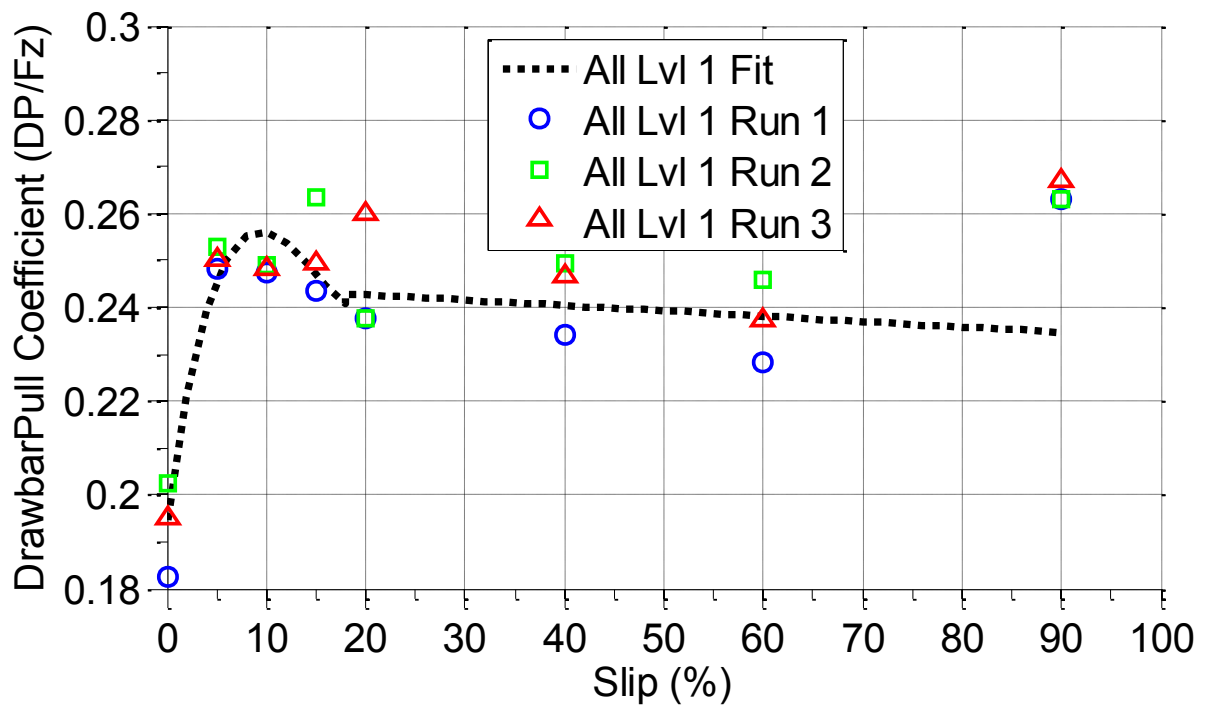


**Figure 7-1. Drawbar pull response vs. slip for all level one parameters of the DOE.**

The commonly observed trend of the drawbar pull coefficient versus slip is evident in Figure 7-1 and has a fitted curve to estimate the overall drawbar pull response. Note from the plot that at 90% slip, the data spikes past all other data points collected, this is in response to a drastically reduced normal load. The reduced normal load is a result of the normal load controller having difficulty adjusting to the rapidly sinking carriage as the test tire reached 90% slip. As a result of this test run, the eighth slip level was changed from 90% to 75% slip for all other test conditions. Another concern for testing at such a high slip level is factoring in the boundary effects of the soil vane due to the sinkage depth of the tire. Similar plots to Figure 7-1 for all the DOE conditions can be found in 0.

The samples collected from each slip level of all runs used to determine the drawbar pull coefficients are also used to determine the wheel sinkage. The data from the string pot measuring wheel carriage displacement is synchronized with the WITS and soil height reader data using UNIX timestamps collected from all three systems. Because the WITS real-time clock sensor lags over time, synchronizing via the timestamp does not hold true results. Therefore, the measured longitudinal force of the wheel and the accelerometer are compared to determine the moment when the wheel would start to move, thus giving an accurate synchronization of the two sensor responses. As a result of the soil preparation procedure, a mound of soil tends to be collected behind the leveling blade which would then produce an obstacle for the wheel to pass over before reaching the prepared soil, this mound conveniently confirmed the time synchronization of the Kistler sensor and soil height reader. However, because the prepared surface is at a constant level, only a small sample of the soil surface is required to know the relative distance from the wheel center so data synchronization is not of

grave importance. A collection of the string pot, WITS and soil height reader (PING) data is shown in Figure 7-2.

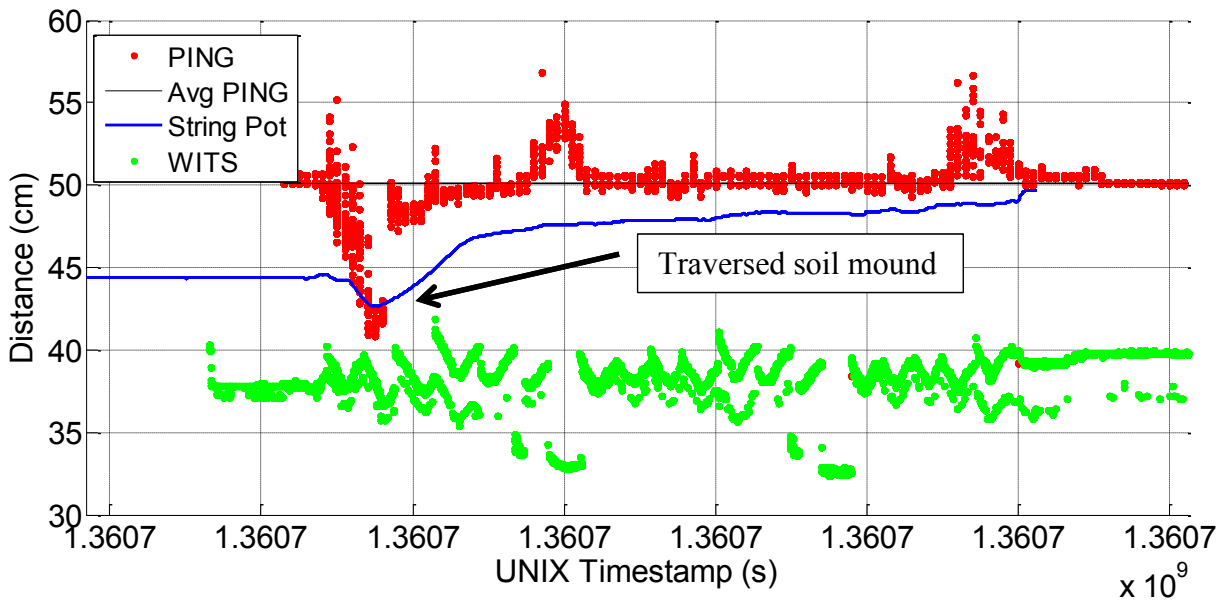


**Figure 7-2. Test run of 4 low range slip changes displaying string pot, WITS, and soil height(PING) measurements**

From Figure 7-2 the data for the overall soil height and tire deflection measurements that occur in parallel with the string pot samples are combined with known constants to ultimately give the measured real-time sinkage. Note the variation of the soil height past the soil mound; this is a result of measuring the soil deformation on the side of the tire as the wheel is plows through the soil. Despite the false average soil height data collected, placing the soil height reader next to the tire is favored to allow for measurement of the rig Home position, flat steel plate as a reference and method of calibration.

Averaging out the data for all the sensors between each slip change provides a close, measured estimate of the max wheel sinkage as shown in Figure 7-3.

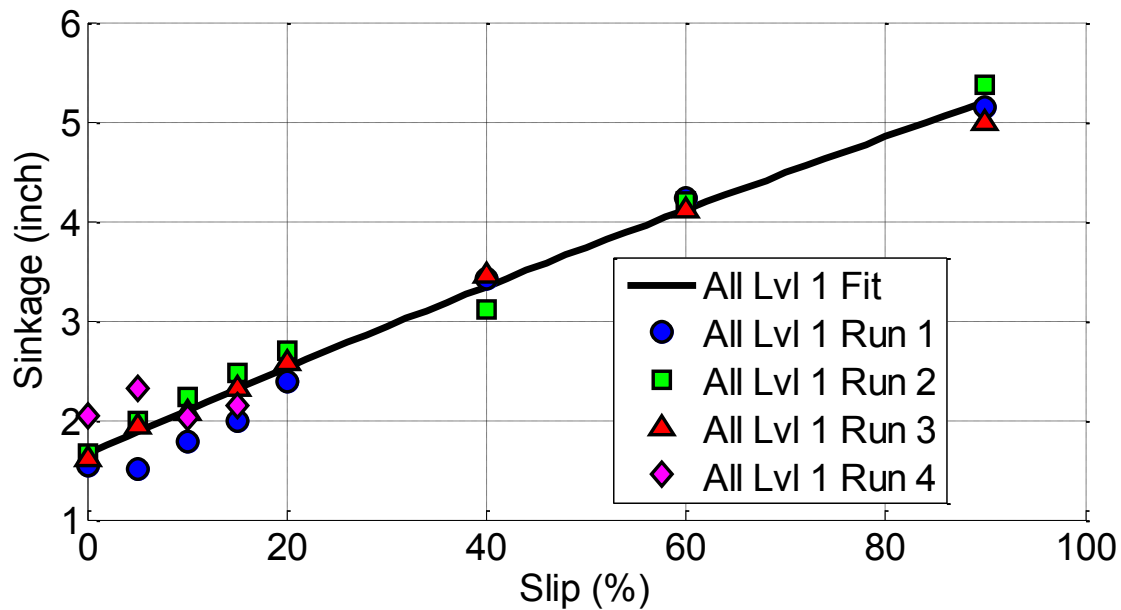


**Figure 7-3. Sinkage measured for the DOE condition of all parameters held to level one.**

Figure 7-3 shows the raw data and fitted curve for the measured wheel sinkage of the DOE condition for all parameters held at level one. This scenario follows a very consistent linear trend throughout the tested slip range. Recall that the average depth of the prepared soil is just over 7 inches so when undergoing 90%, the wheel is less than 2 inches from touching the rigid U-channels beneath the soil. Because of this large depth, the U-channels are suspected to have interacted with the undisturbed boundary layer of the soil and affected the max sinkage, hence the reasoning for reducing the final slip level to 75%. Similar plots to Figure 7-3 for all conditions of the DOE can be found in Appendix (C).

## **7.2 Comparative Analysis of One Parameter Change**

This section will review the drawbar pull and sinkage response of the tire as a result of changing only one parameter of the DOE to the second level while keeping all other parameters constant at the first level. The three parameters to change individually are the normal load from 5kN to 6kN, the tire inflation pressure from 29 psi to 20 psi, and the soil compaction from a cone index of 4.4 kPa/mm to 6.5 kPa/mm. The results of these parameters changes will be compared with the DOE condition of all parameters held at the first level which will act as a baseline reference to observe how each parameter affects the tire performance. Figure 7-4 shows the drawbar pull raw data and curve fits for all single parameter changes of the DOE.

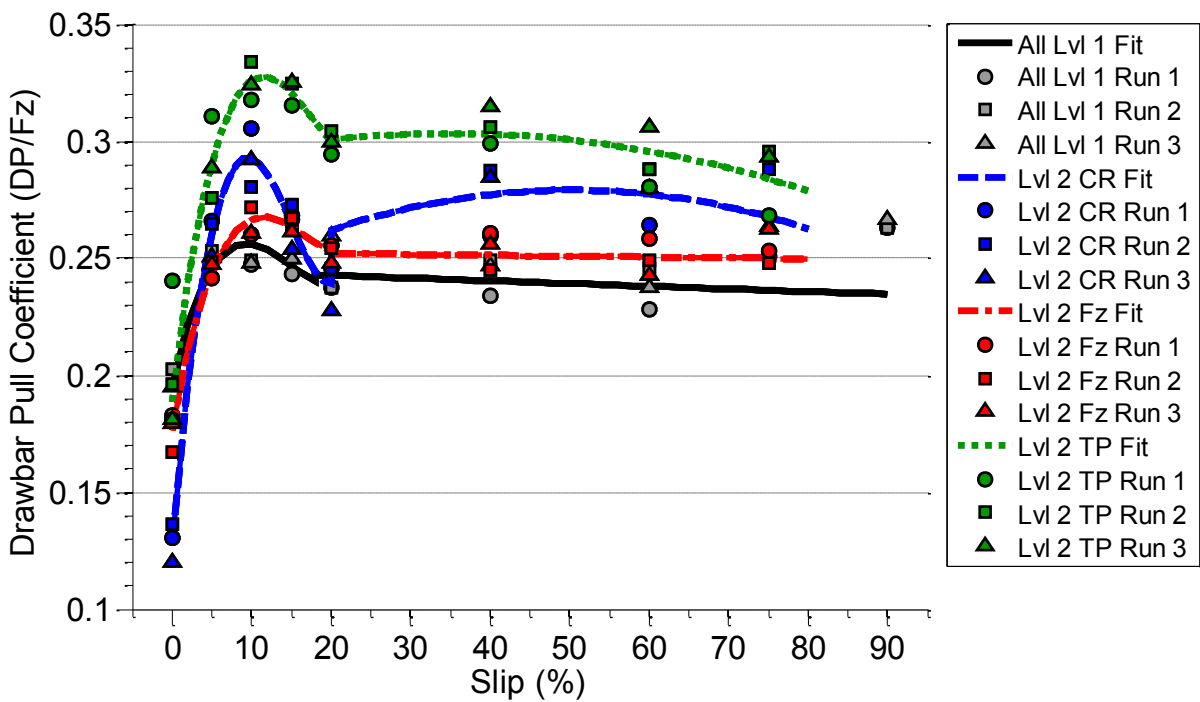


**Figure 7-4. DP coefficient vs slip response to individual parameters changes of the DOE. The black curve represents the level one condition for all parameters. The blue, red, and green curve represent the second level of inflation pressure, normal load and compaction resistance, respectively.**

In review of this plot, the drawbar pull results for each condition are fairly consistent and follow the expected trend versus slip. All conditions were observed to achieve the peak drawbar pull at, more or less, around 10% slip. The condition observed to achieve the highest peak and overall drawbar pull is for the lowered inflation pressure of 20 psi. This condition has a tremendously positive impact on the tire performance, unlike the original second tire inflation level of 26 psi.

The compaction resistance level of 6.5 kPa/mm followed with the second highest peak in drawbar pull. However, once approaching 20% slip, the drawbar pull reduces to a magnitude similar to the first level condition, then in the higher slip range returns to a higher magnitude. This behavior is speculated to be a result of either the experimental method used for applying slip changes, the fact that only the first 2 inches hold a consistent soil compaction, or both. Coincidentally, following this test condition, the motor control algorithm was changed from applying the initial slip condition at the start of the test, to applying zero slip at the start and then switching to the initial slip condition once the tire has reached the prepared soil. The reason for this change was to keep the baseline steel platform in the rig Home position stationary because starting a test run at 20% slip would apply a torque strong enough to kick the steel plate past the measuring range of the soil height reader. Although the intention is unrelated, this change may have prevented similar test results from other conditions. This midrange slip region should be retested to confirm its source of reduced drawbar pull performance.

Interestingly, the 6kN second level of normal load resulted in a higher drawbar pull coefficient. This is believed to be a result of the normal load further compacting the soil as the wheel rolls, thus

providing a more rigid terrain for greater traction. This condition also maintained a steadier drawbar pull in the high slip region in comparison with the other conditions.

A consistent response to note for all conditions displayed in Figure 7-4 is the apparent drawbar pull measured at the zero slip condition, which is expected to be either nonexistent or negative. This is mainly attributed to a slight miscalculation of rolling radius which provides a false wheel speed to maintain the intended slip value. The motors also tended to have a small amount of error when applying the desired speeds at a given load. However the data is not expected to be too far off from the intended slip values presented, as the overall trend of the curves show true differences between slip changes and are consistent with related literature. The accuracy of the rolling radius determination can be improved by performing a more thorough validation test of the WITS sensor system with the latest sensor bracket configuration.

To observe the relative difference in drawbar pull magnitude between slip values, the data presented in Figure 7-4 is shifted so that the zero slip condition provides zero drawbar pull, this is shown in Figure 7-5.

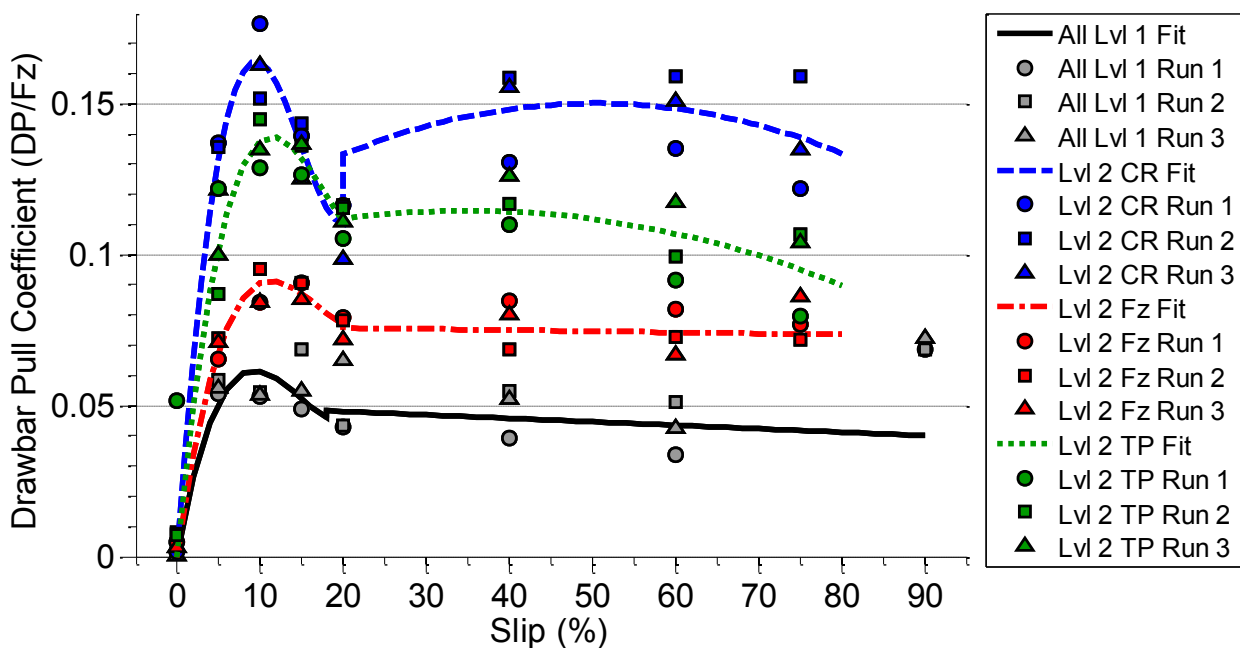


**Figure 7-5. DP coefficient vs slip response to individual parameters changes of the DOE, with the zero slip conditions shift to a zero DP coefficient response. The black curve represents the level one condition for all parameters. The blue, red, and green curve represent the second level of inflation pressure, normal load and compaction, respectively.**

The individual changes in parameters still maintain a higher drawbar pull response than the initial condition of all parameters held to the first level. However with this adjustment the data from the second level compaction has a greater relative difference in magnitude between slip values. This can be attributed to a better estimate of the rolling radius, thus providing a more ideal response of the tire performance in a zero slip condition. This plot also demonstrates the large impact that the changes in

parameters make in the drawbar pull performance; for example, although the higher compaction level affected mainly the first few inches of prepared soil, the tire still managed to perform better.

Figure 7-6 shows the measured sinkage response of the tire as a result of individually changing the parameters to the second level.

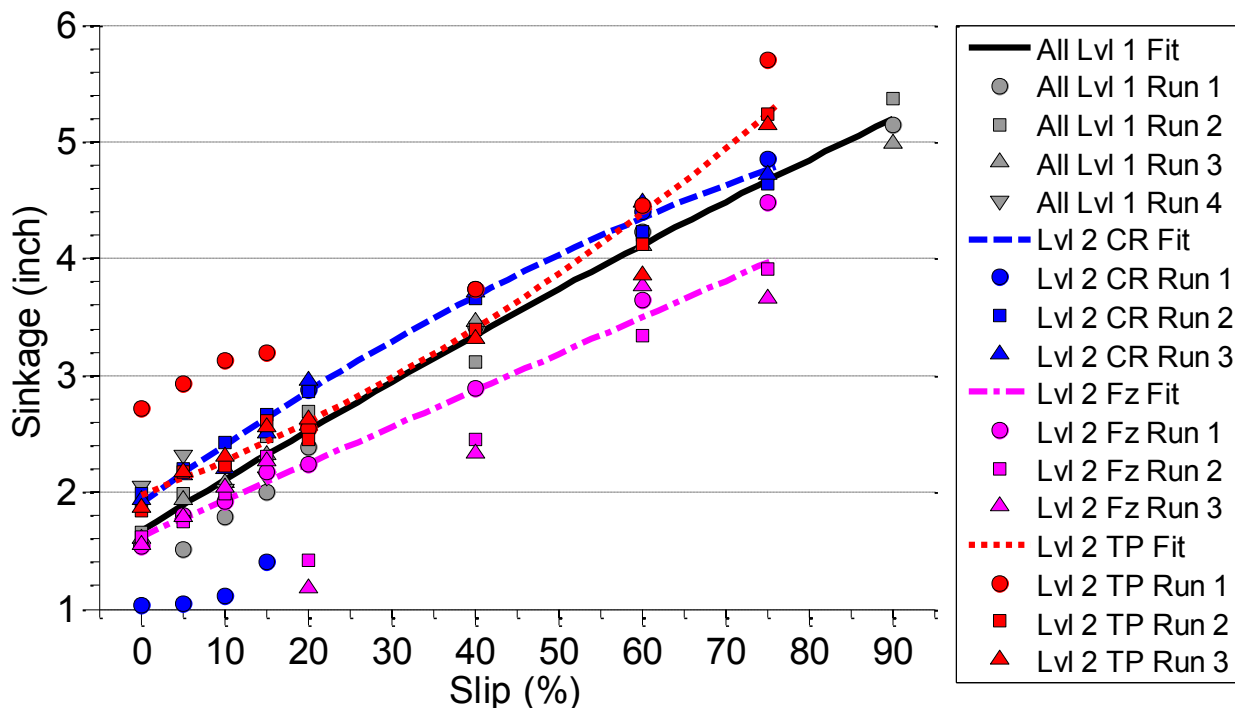


**Figure 7-6. Wheel sinkage vs. slip response to individual parameters changes of the DOE. The black curve represents the level one condition for all parameters. The blue, magenta, and red curve represent the second level of compaction, normal load and inflation pressure, respectively.**

Although the condition of all parameters held at the first level tested at a high slip of 90% slip, the second level inflation pressure of 20 psi resulted in a comparable sinkage depth and even achieves a higher depth in one run. The trend observed in this condition also follows a slight exponential pattern, which is speculated to be the result of interacting with the looser soil once passing the 2-3 inches of prepared soil depth. It has also been observed in the literature that for a specific normal load and inflation pressure combination, particularly when both are reasonably low, the average ground pressure can be less than the tire inflation pressure, which can result in a greater sinkage depth [3].

The second compaction cone index level of 6.5 kPa/mm also resulted in a larger sinkage depth than the level one condition up until 75% slip. The data actually follows an identical trend to what was measured with the cone penetrometer, which would initially measure a linear response with a high amount of resistance for the first few inches, then resistance would increasingly shallow out as the depth increased, this is shown in Section 5.2.

The second normal load level of 6 kN experienced the least amount of sinkage. This condition also followed a more linear sinkage response with increasing slip. The results of this condition fortify the speculation that because of the increase in load, the soil is being further compacted while the wheel rolls over the prepared terrain, rather than displacing more soil in either direction to sink deeper.

### 7.3 Comparative Analysis of Several Parameter Changes

Following the design of experiment, the remaining four conditions of testing two and all parameters at the second level simultaneously will be presented in this section. The conditions specifically are the: normal load and inflation pressure, normal load and soil compaction, inflation pressure and soil compaction, and all three parameters. The baseline reference condition of all parameters held to the first level will be presented as well. This comprehensive plot is shown in Figure 7-7.

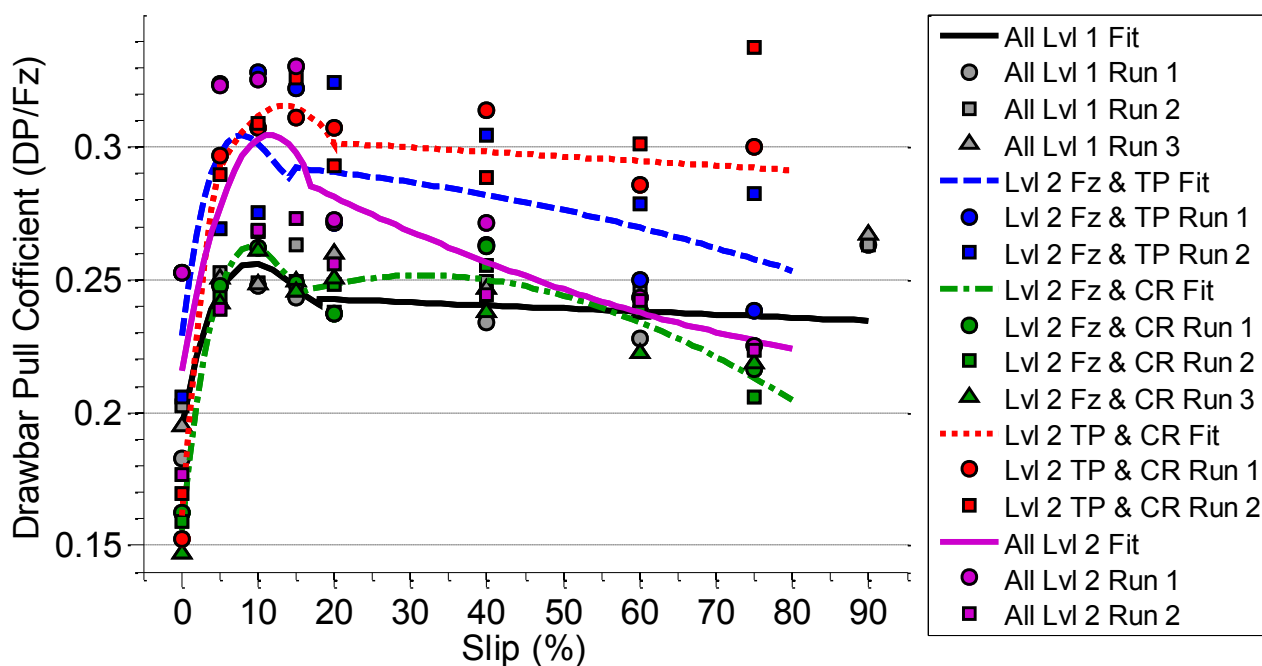


**Figure 7-7. DP coefficient vs slip response to several parameters changes of the DOE. The black curve represents the level one condition for all parameters. The following second level parameter combinations and their representative color are: blue, for normal load and inflation pressure; green, for normal load and compaction; red, for inflation pressure and compaction; and magenta for all parameters at the second level.**

The parameter combination of second level inflation pressure (20 psi) and compaction resistance (6.5 kPa/mm) is observed to have achieved the highest drawbar pull. This further confirms the positive impact inflation pressure has on the tire performance. The combination also avoids the abrupt dip in drawbar pull performance at around 20% slip as previously observed with the higher compaction level alone.

Note from the plot that the combinations of inflation pressure and soil compaction, normal load and inflation pressure, and all parameters held to the second level, all have two runs rather than three like all the other conditions. For the second level condition of inflation pressure and compaction resistance, the first collected run of data had a very odd response which appears to be the result of control error from performing the experiment. The results of that run did not hold any conclusive findings so it was withheld from the final analysis. In review of the other runs for the same condition, the drawbar pull response was consistent enough to see the general trend.

However, in review of the normal load and inflation pressure combination and the condition where all parameters are at the second level, a fair amount of variation is observed between the only two runs collected. The variation of the response for these conditions is believed to result from irregularity in the soil compaction, which is more evident in the plots that show the results for each condition alone, found in the 0 . At the time of testing these two conditions, the unused lane of soil in the soil vane was being removed between test runs. The loss of the soil is believed to have made an inconsistent and negative impact on the boundary layer of the prepared soil due to the fact that there were no soil support along the plane of soil in parallel with the rolling tire. Nonetheless, a trend is observed among the two conditions but the fitted curve is not expected to be a true representation of the tire performance.

Interestingly, both conditions of the normal load and inflation pressure combination and all parameters at the second level, behave similarly on their rise to the peak drawbar pull coefficient. In the higher slip range, both decrease at a steeper rate than the other conditions. The condition of all parameters set at the second level in particular displays a very acute decrease and intersects the baseline reference curve at 60% slip. These two curves show that there must be an interaction with the normal load to cause the drastic decrease.

The combination response of the second level normal load and soil compaction share the very same qualities as the responses of these parameters raised individually. The response is a small factor greater than the baseline reference, and similar to the individually raised normal load response. Once 15% slip is reached, the response decreases swiftly and momentarily intersects with the curve for all parameters at level one, before increasing again, similar to the individual response of the compaction resistance at a higher level. However, similar to the other conditions that contain a higher normal load, the drawbar pull decreases rapidly after 40% slip and intersects the baseline curve at 60% slip.

To have a better view of the overall data and observe the relative difference in drawbar pull magnitude between slip values, the data presented Figure 7-7 is again shifted so that the zero slip response matches a near nonexistent drawbar pull, as shown in Figure 7-8.

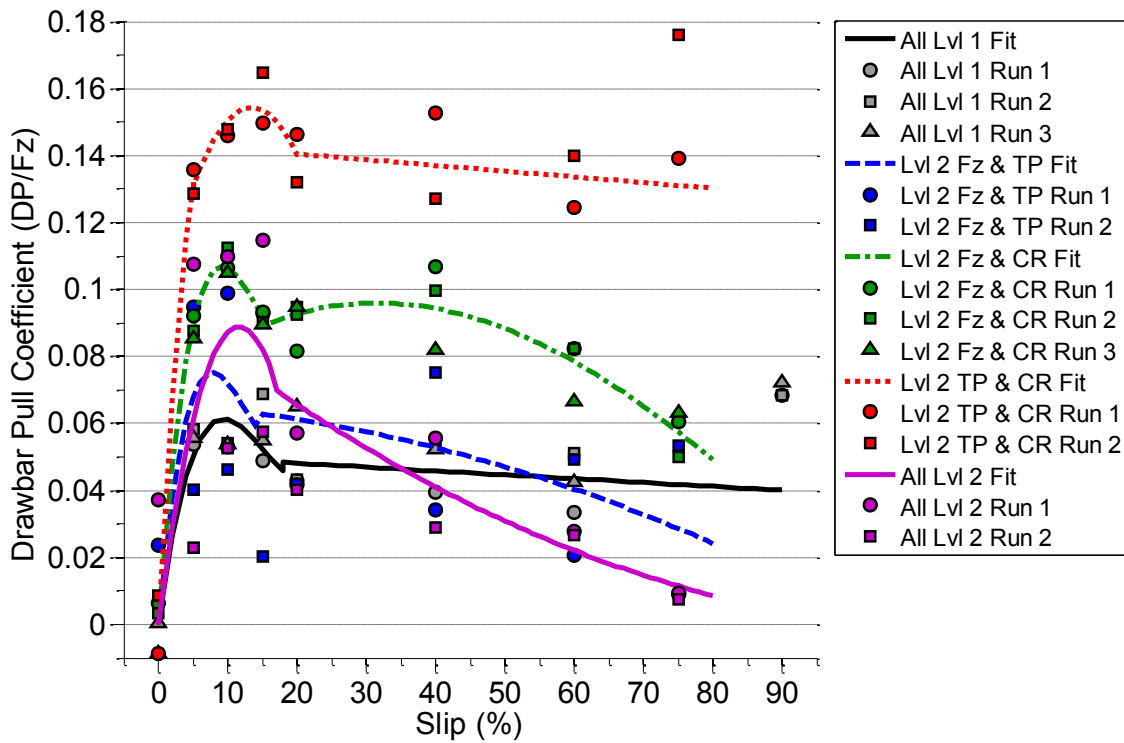


**Figure 7-8. DP coefficient vs slip response to several parameters changes of the DOE, with the zero slip conditions shift to a zero DP coefficient response. The black curve represents the level one condition for all parameters. The following second level parameter combinations and their representative color are: blue, normal load and inflation pressure; green, normal load and compaction; red, inflation pressure and compaction; and magenta for all parameters at the second level.**

Similar to the previous plot, the second level combination of inflation pressure and soil compaction has a greater relative difference in the lower slip drawbar pull response and maintains a higher magnitude than the other conditions. Again, the relative difference between the plots depends on how well the rolling radius was measured for each condition so that a true zero-slip condition is measured. Figure 7-8 also gives a better view of how the second level combination of normal load and soil compaction drawbar pull response has the abrupt decrease from 10-15% slip then follows an increase from 15-40% slip before going into a descent in the higher slip region.

The max sinkage response of the multiple parameter level conditions is shown in Figure 7-9.

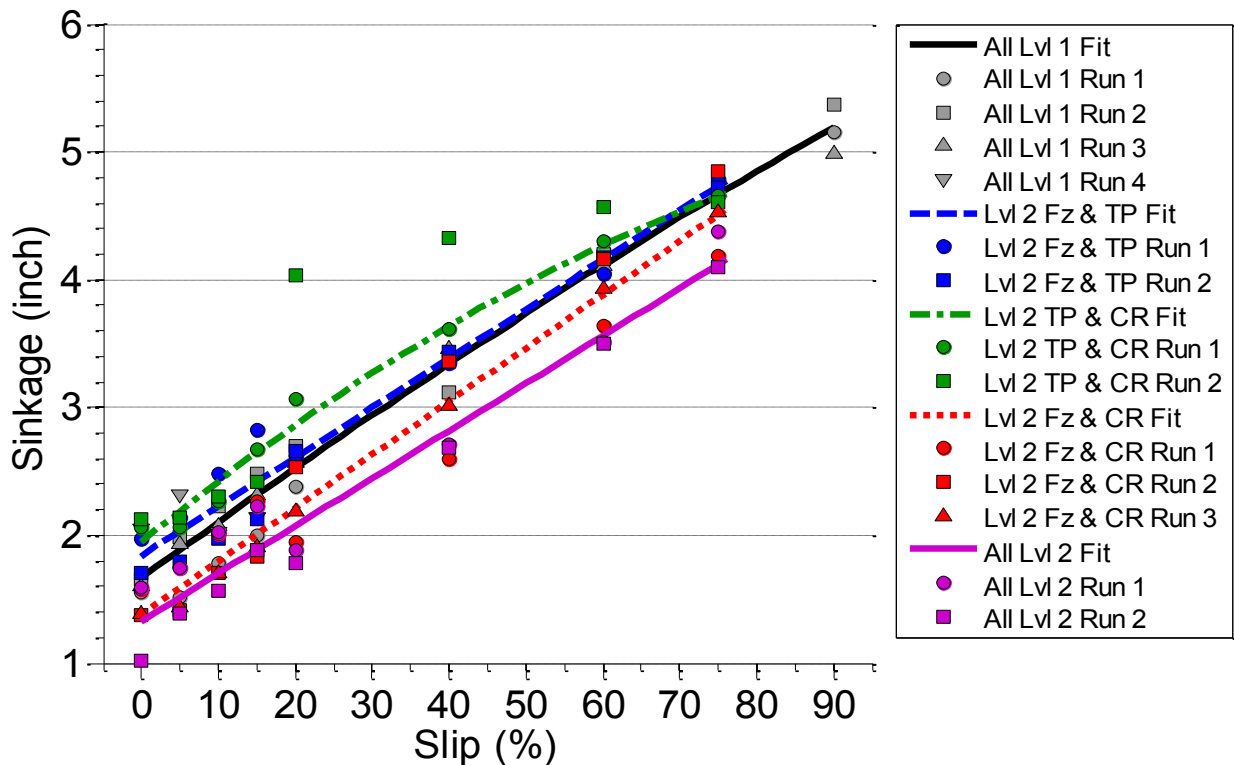


**Figure 7-9. Wheel sinkage vs. slip response to several parameters changes of the DOE. The black curve represents the level one condition for all parameters. The following second level parameter combinations and their representative color are: blue, normal load and inflation pressure; green, inflation pressure and compaction resistance; red, normal load and compaction resistance; and magenta for all the parameters held to the second level.**

Similar to the second level individual responses of the inflation pressure and soil compaction, the combination of the two resulted with the greatest sinkage depth among all other conditions until 75%. However, unlike the individual response of the lower inflation pressure, which met the sinkage depth of the baseline condition at 90%, the interaction of the higher soil compaction resulted in a shallower sinkage depth and also followed a similar nonlinear trend past 20% slip.

In Figure 7-6, the individual response of the high normal load resulted in the least amount of sinkage among the other conditions; when combined with a lower inflation pressure, known to sink, the two parameters interact to reach a sinkage similar to the baseline condition. The curve for the two parameter combination follows the response of the low inflation pressure in the lower slip region, yet as the slip increases, the normal load appears to aid in reducing the overall sinkage.

The second level combination of the normal load and soil compaction also displays a strong interaction with the higher load as the response measures a shallower sinkage than the pure level one condition. The combination response shares a more linear trend similar to the individual response of the higher soil compaction, yet with the interaction of the higher normal load, the response is shifted to a lower overall sinkage depth.

Combing the second level of all parameters, 6kN normal load, 20 psi inflation pressure, and cone index of 6.5 kPa/mm for soil compaction, results in the least amount of sinkage among the pa-

parameter conditions. The individual response of the higher normal load and the second level combination of all parameters, both result in nearly the same max sinkage at 75% slip. However the pure second level condition appears to start with the least amount of sinkage, at just over 1 inch, in the lower slip region and follows a linear trend in parallel with the pure level one condition.

It is interesting to see that despite experiencing the most sinkage, the second level combination of the inflation pressure and cone index, overcome the increased resistances of the soil and still manage to attain a higher drawbar pull than the rest of the combined parameters. However, considering the fact that all other combined parameter conditions include a higher load, thus increasing the denominator of the drawbar pull coefficient, explains the difference in magnitude.

### 7.4 Review of all DOE Conditions

The drawbar pull coefficient and sinkage responses for all conditions of the design of experiment have been discussed separately but will now be displayed together to see the comparative difference among the parameter changes. Figure 7-10 shows the drawbar pull response of all conditions in the design of experiment.

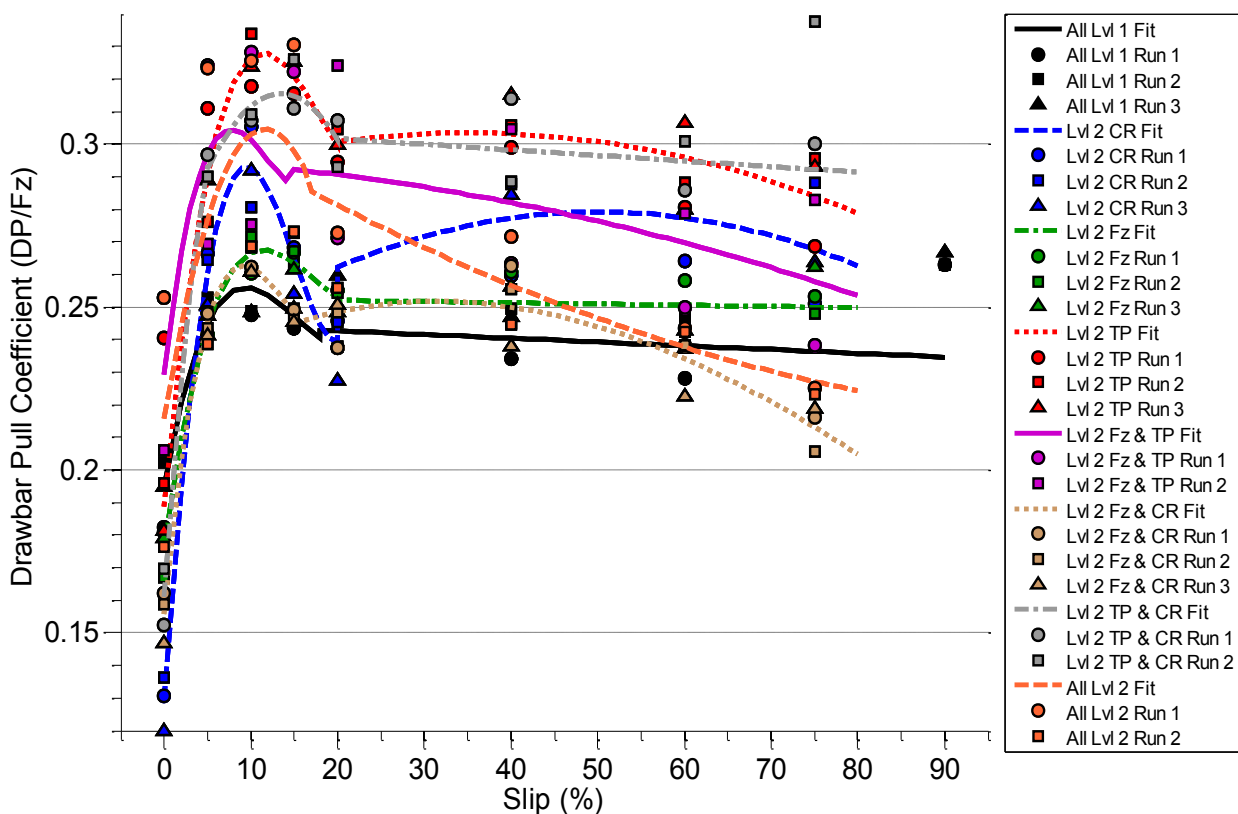


**Figure 7-10. DP coefficient vs slip response to all the conditions of DOE. The black and orange curves represent all parameters set to level one and two, respectively. The individual parameter changes and their representative color are: blue, compaction (CR); green, normal load (Fz) ; and red, inflation pressure (TP). The following second level parameter combinations and their representative color are: magenta, Fz and TP; beige, Fz and CR; and gray, TP and CR.**

In review of the conditions in the design of experiment, the individual second level change of the inflation pressure provides the greatest drawbar pull coefficient. All other multiple parameter combinations perform better than the individual changes except for the second level combination of the normal load and soil compaction. All conditions appear to improve the tractive performance of the tire in comparison to the baseline condition of all parameters set to the first level. However, some conditions measured a lower drawbar pull coefficient, such as for the momentary dip in performance at 20% slip for the second level of compaction and the descend in performance for both the second level combination of the normal load and soil compaction, and the second level combination of all parameters, past 60% slip.

Figure 7-11 shows the measured sinkage response to all the conditions of the design of experiment.

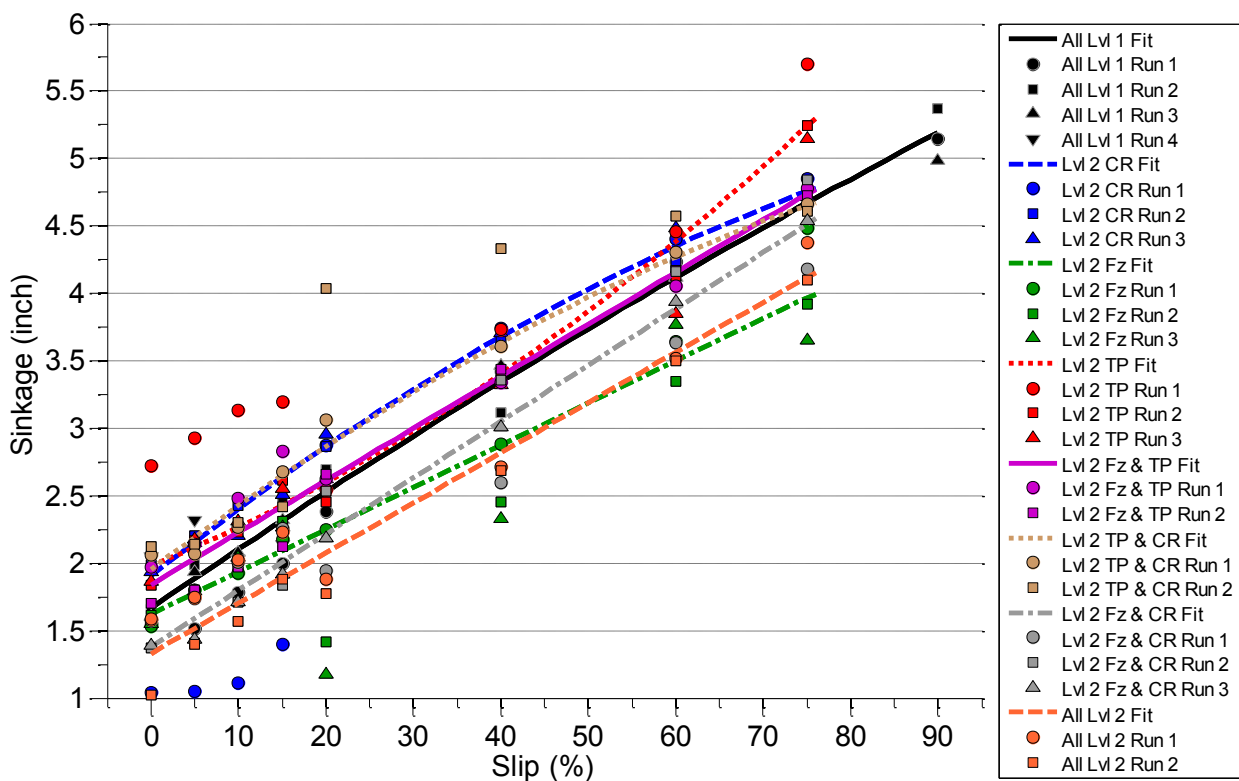


**Figure 7-11. Sinkage vs slip response to all the conditions of DOE. The black and orange curves represent all parameters set to level one and two, respectively. The individual parameter changes and their representative color are: blue, compaction (CR); green, normal load(Fz) ; red, inflation pressure (TP); purple, Fz and TP; beige, TP and CR; and gray, Fz and CR.**

In review of the various parameter configurations of the design of experiment, changing the parameters individually yielded the most sinkage, whereas most parameter combinations were observed to have a reduced sinkage depth. The condition to achieve the greatest depth in sinkage at 75% slip is the sole parameter change of lowered inflation pressure at 20 psi; this condition surprisingly surpassed the sinkage depth of the pure level one baseline condition at 90% slip. The combination of all second level parameters yielded the least amount of sinkage.

## 7.5 Main Effects and Interaction of Parameters

Main effects and interaction plots of the average drawbar pull coefficient and sinkage will give a clear representation of the effects that the individual parameters have on the conditions of the design of experiment. The main effects plot simply shows the average outcome of the response variable and correlates this with the levels of each parameter, or factor. The larger the response variable for a specific parameter, the greater effect it has on the result.

For an interaction plot, the levels of two factors are plotted against each other to see whether there is an interaction. The levels of one factor are listed as the independent variable, and the response variable resulting from the two levels of the other factor are plotted against the other parameter. An interaction is identified if the plotted factor levels intersect; if the plotted factors levels remain parallel, there is no interaction.

The interaction plot presented in this section will be displayed as a matrix plot where the rows and columns of the matrix equal the number of factors. The mini plot shown in the off-diagonal position (i, j) is the interaction of the two factors whose label is identified on the row diagonal (i,i) and column diagonal (j,j), respectively.

### 7.5.1 Parameter Effects on Drawbar Pull Response

Considering the nonlinear behavior of the drawbar pull versus slip relationship and the fact that both main effects and interaction plots require an average response, the peak and high slip drawbar pull coefficients are used to create plots rather than the slip range. The main effects plot for the peak drawbar pull coefficient response is shown in Figure 7-12.

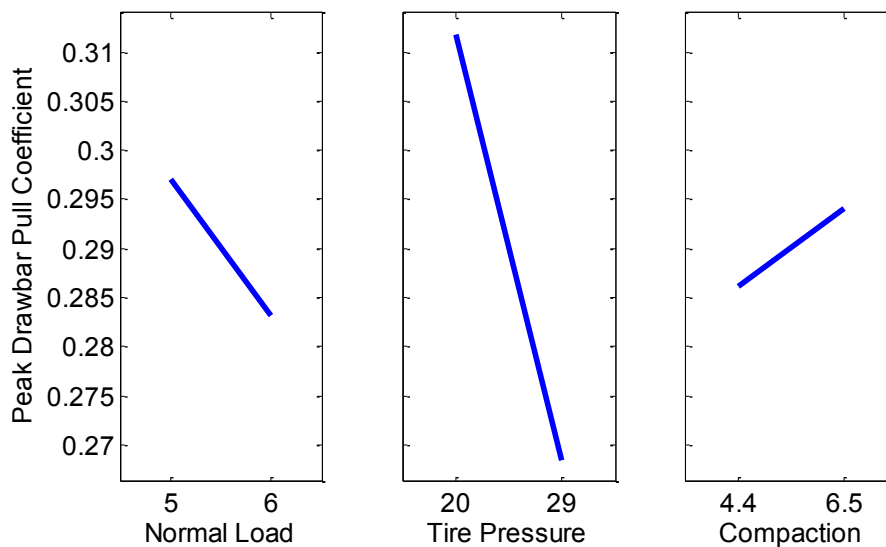


**Figure 7-12. Main effects plot of the average peak drawbar pull coefficient.**

The main effects plot fortifies claims of the previous subsections, such as the large positive impact that a lower inflation pressure has on tire performance. The plot also shows that the normal

load is the next big factor, as a larger drawbar pull coefficient is observed with a lower normal load and vice versa. The soil compaction is found to have the least effect among the three parameters.

The main effects plot for the drawbar pull measured at 75% slip is shown in Figure 7-13. Due to the fact that a 75% slip run was not tested for the baseline condition of all parameters kept at the first level, an average was taken on the drawbar pull response between 60% and 90% slip.

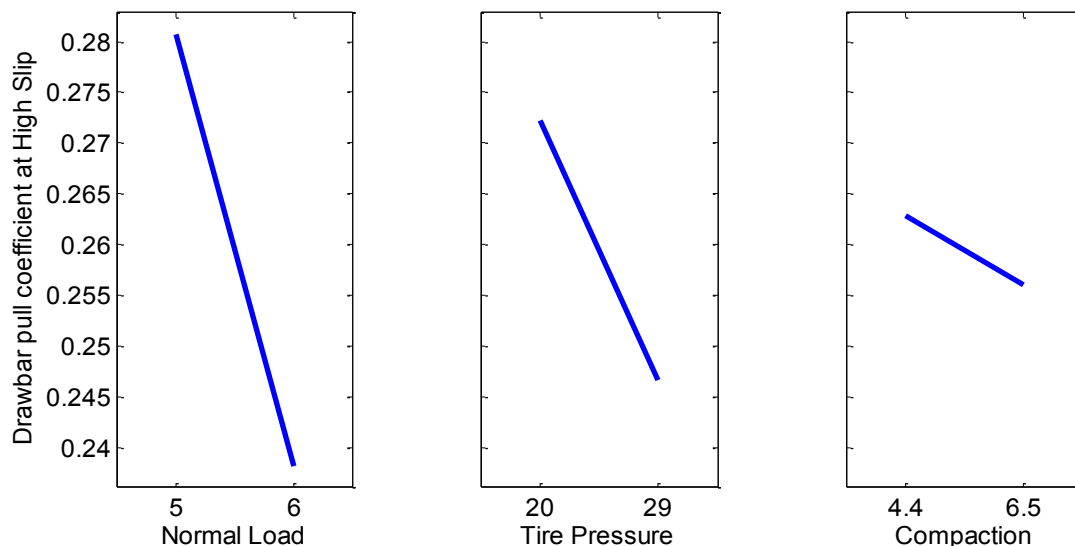


**Figure 7-13. Main effects plot of the average high slip drawbar pull coefficient.**

Towards the high slip region of the drawbar pull response, the normal load is shown to be the main effect. Inflation pressure again is the second greatest effect. Although the least effective, the first compaction level has a greater impact on the drawbar pull response than the second level, as opposed to the measured peak drawbar pull response.

The interaction of the parameters on the drawbar pull response coefficient is shown in Figure 7-14.

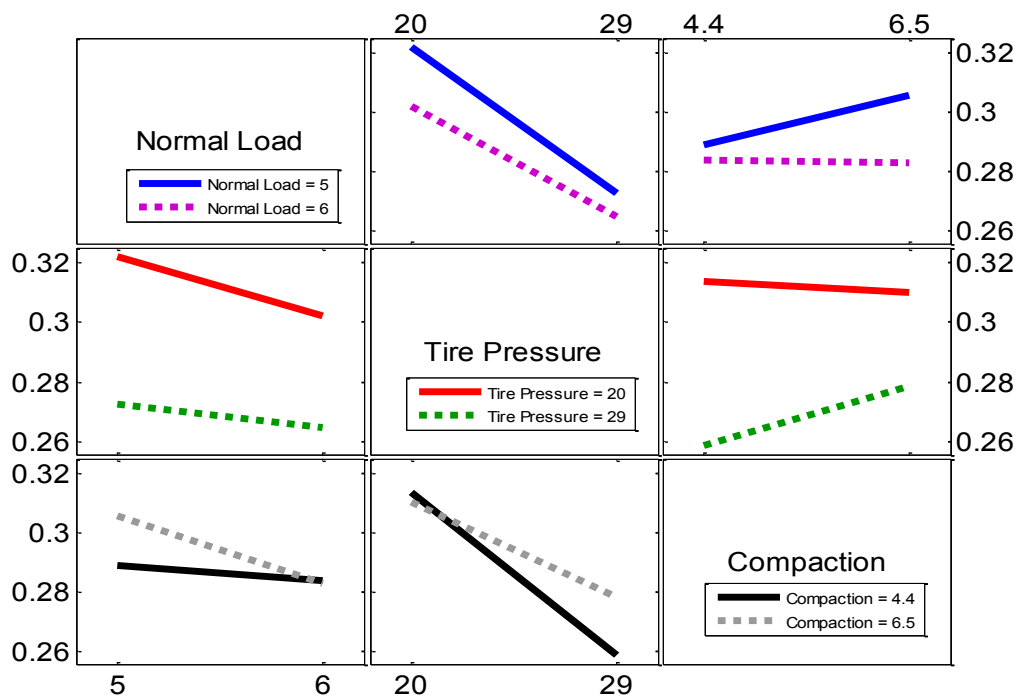


**Figure 7-14. Interaction plot of the normal load, inflation pressure, and soil compaction parameter levels on the peak drawbar pull response.**

The interaction plot for the peak drawbar pull response shows that the normal load does have an impact on the soil compaction. The inflation pressure also has an interaction with the soil compaction. This confirms the claims presented in the previous plots. All other parameters are shown to have no interaction.

The interaction plot for the drawbar pull response at high slip is shown in Figure 7-15.

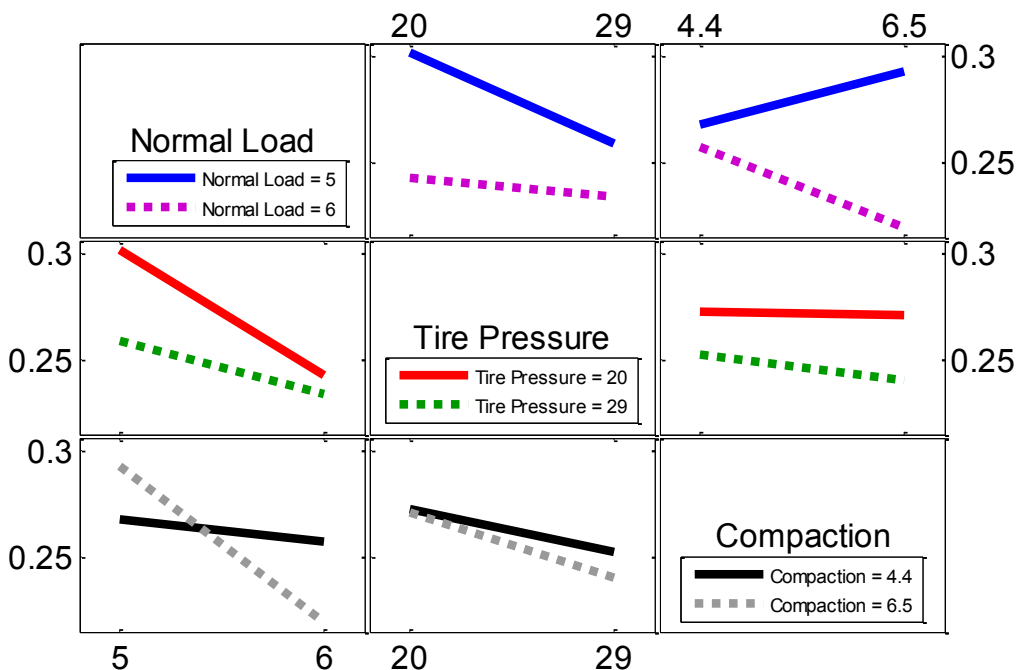


**Figure 7-15. Interaction plot of the normal load, inflation pressure, and soil compaction parameter levels on the high slip drawbar pull response.**

In review of the interaction plot for the high slip drawbar pull response, the normal load is shown to have an even greater impact. This is quite evident in the multiple parameter conditions that include normal load. There is less of an interaction between tire pressure and soil compaction but is still present. Interactions among the other parameter combinations again are nonexistent.

### 7.5.2 Parameter Effects on Sinkage Response

Because the sinkage response for all conditions follow, more or less, a linear trend, the average sinkage response throughout all slip levels will be used in this graphing statistical analysis. The main effects plot for the overall sinkage, shown in Figure 7-16, yields near similar results to the high slip drawbar pull plot.

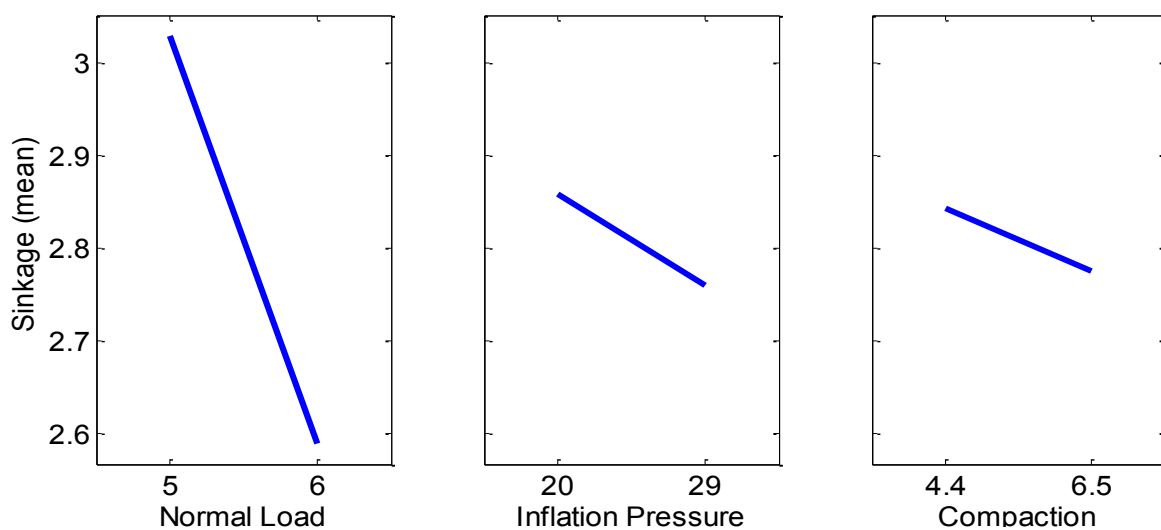


**Figure 7-16. Main effects plot of the overall average sinkage.**

The normal load is shown to have the greatest effect on the overall sinkage response. This fortifies the consistently reduced sinkage witnessed among conditions involving a higher normal load. Both the inflation pressure and soil compaction appear to have similar magnitudes of effect.

The interaction between the three parameters on the overall sinkage response is shown in Figure 7-17.

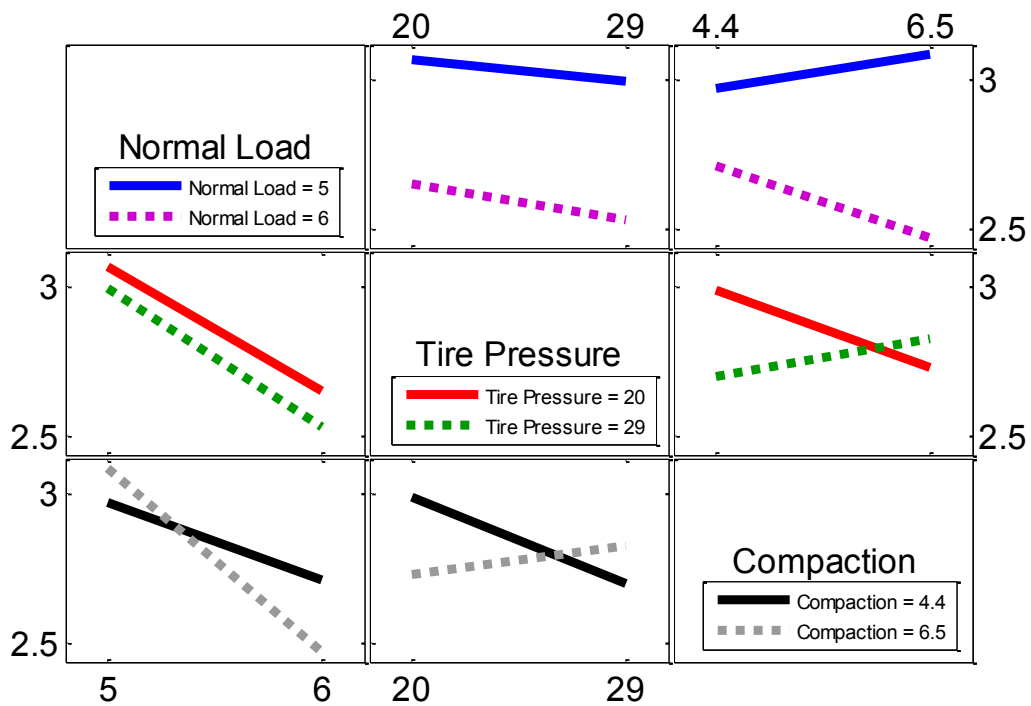


**Figure 7-17. Interaction plot of the normal load, inflation pressure, and soil compaction parameter levels on the sinkage response.**

More parameter interactions are present upon review of the interaction plot for the overall sinkage response. Like the drawbar pull response, the normal load and soil compaction interact as well as the tire pressure and compaction. However, these parameters interact in a higher degree on the wheel sinkage, rather than the drawbar pull response. The different soil compaction levels also interact similarly to the inflation pressure.

## 7.6 Parameter Variation

Although the parameters in the design of experiment were intended to remain constant throughout a test run, some variation was observed between runs and slip ranges. Due to the low resolution of the pressure gauge ( $\pm 0.5$  psi), the inflation pressure between runs and conditions was found to remain constant. Although if it were to have varied by a fraction of 1 psi, the variation could not have made a great impact on the test results; as evident from preliminary tests which found that a 10% variation in tire pressure had little effect on drawbar pull performance.

In review of the level one normal load condition of 5 kN, the results show that the normal load variation remained under the target acceptable range of a 3% difference for most of the slip values. Upon higher slip ranges, primarily 75-90% slip, the normal load controller had difficulty maintaining a constant normal load. The impact on the drawbar pull results for these conditions is evident by the outliers shown in Figure 7-5 and Figure 7-7. The outliers represent how sensitive the drawbar pull coefficient is to a 3% and greater variation in normal load.

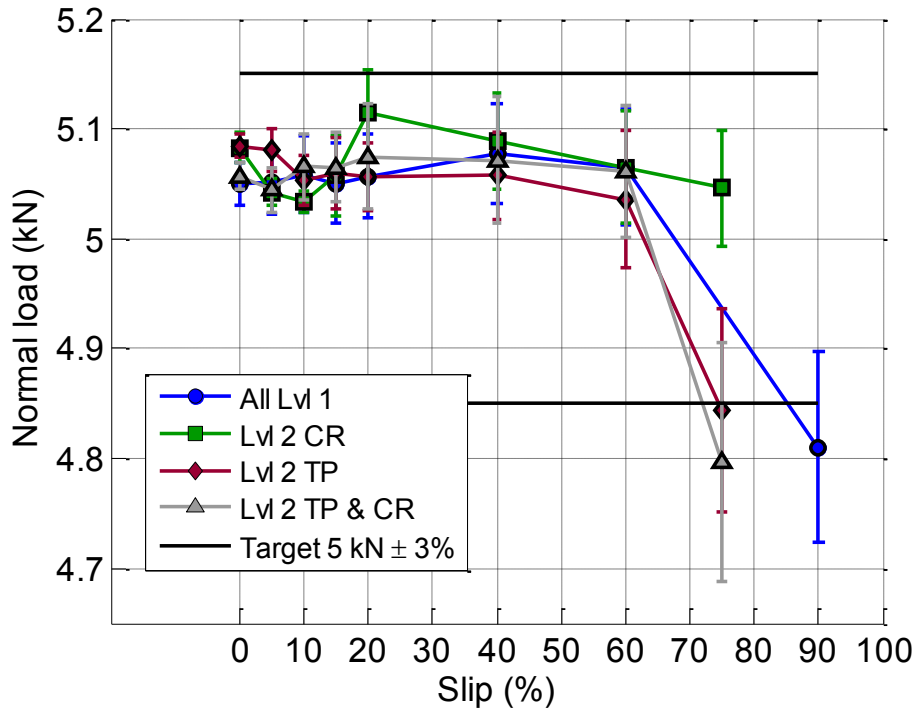


**Figure 7-18. Normal load variation for the level one condition of 5 kN.**

The increase in normal load at 20% slip for the high compaction resistance condition also aids the dip found in the drawbar pull coefficient in Figure 7-5.

The conditions with a level two normal load of 6 kN, as shown in Figure 7-19, were observed to have experienced more variation in the higher slip range than in the lower range, similar to the level one condition.

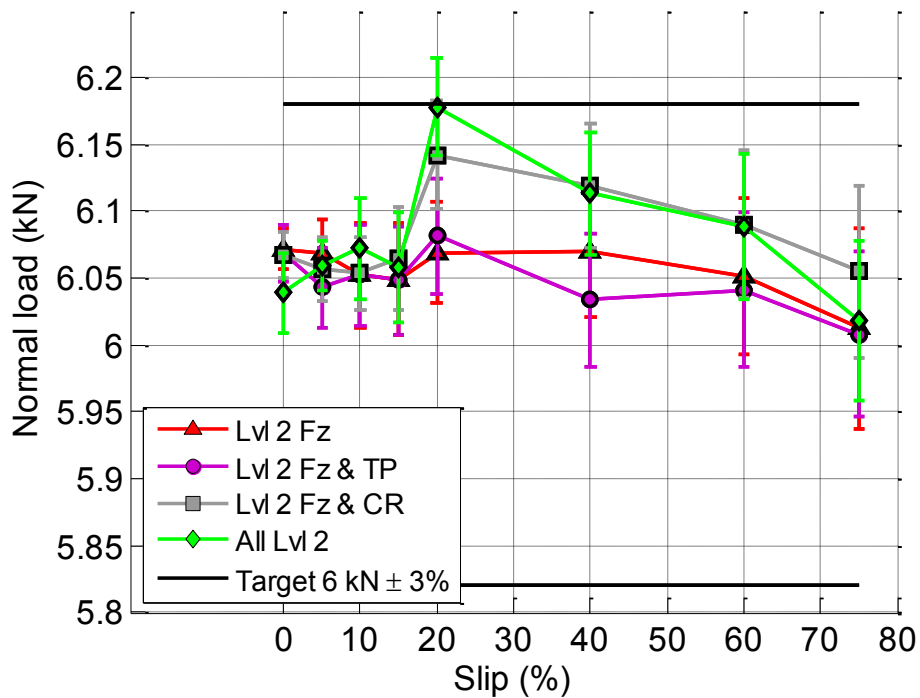


**Figure 7-19. Normal load variation for the level two condition of 6 kN.**

For the higher load conditions, most of the load variation was kept under a 3% difference. However, for the conditions which include a higher compaction resistance at 20% slip, the normal load was found to spike up to a 3% difference. This correlates with the dip in drawbar pull coefficient for both conditions shown in Figure 7-7.

The variation in soil compaction as a response in the cone index gradient is shown in Figure 7-20.

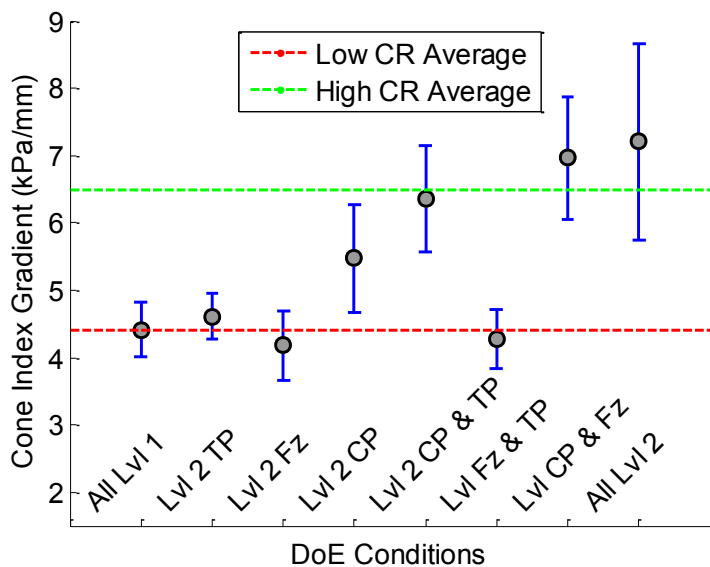


**Figure 7-20. Soil compaction variation measured with the CI gradient (kPa/mm) between all DOE conditions.**

The low level soil compaction condition of 4.4 kPa/mm was found to have little variation of 0.4 kPa/mm, whereas the high level compaction condition of 6.5 kPa/mm had greater variation of 0.9 kPa/mm. The all level two condition experienced the greatest variation in soil compaction. This is expected to be attributed to the soil that was being removed from the unused lane of unprepared soil in the rig while testing. The removal of soil appears to have affected the soil boundary layer which explains the large variation in the drawbar pull coefficient for the all level two condition.

Because both levels of compaction required a common moisture content reference, soil samples for nearly each run of all conditions was collected and measured for moisture content and are plotted in Figure 7-21.

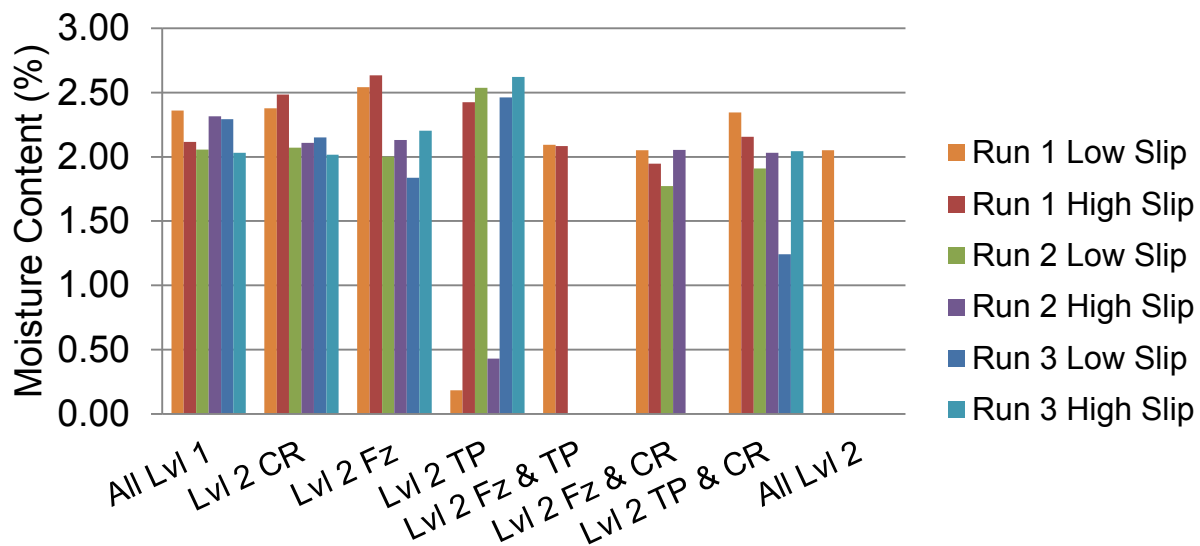


**Figure 7-21. Moisture content variation between each condition and run.**

The target moisture content to achieve was approximately 2.6 %, yet as shown in Figure 7-21, that target is barely achieved. Prior to testing for a particular condition, the moisture content is adjusted to measure nearly 2.6% with a variation of 10%. Once the MC is at an acceptable level, testing commences and samples are collected while testing. To increase time efficiency between test runs and reduce water drainage, MC of the soil samples are tested while the rig is preparing the soil for a test run i.e. , MC testing is done in parallel with soil preparation and not prior to a test run. While testing, if the MC for an earlier test run shows a reduced MC, then a small amount of water is added to the soil. However when the results for a condition are reviewed, the variation in MC tends to vary much from the first run sample. This is especially evident in the condition of a low tire pressure termed “Lvl 2 TP” in Figure 7-21. The variation in moisture content may be the reason for the increased tire sinkage depth observed in the higher slip range.

The variation in MC results show that the microwave test method for measuring MC requires too much time and does not give representative MC results for the depth of prepared soil. Because the initial soil preparation for a test condition requires newly added water to adjust the MC to an ideal range, the microwave test results from this preparation can yield higher MC results as the water in the soil has not had much time to drain or evaporate. Additionally, several soil samples are required for each test run to get an average of the MC. As the samples are waiting to be measured from a test run, several things can happen to provide false results such as soil sample vials may fall and break or a portion of soil falls from the vial while the weight is being measured. It is because of these reasons that several MC results are missing from the Figure 7-21. Therefore for future soft soil testing where moisture content should be closely controlled, a faster, alternative method of measuring moisture content should be explored.

## 8 Conclusions and Future Work

This was an experimental study to improve the understanding of the interaction between a pneumatic tire and deformable terrain. A thorough literature review revealed the techniques and measurement methods utilized in various studies of tire-soil interaction and tire instrumentation. A design of experiment was employed to investigate the effect of individual tire and soil parameters as well as the effect of the parameter interactions. The parameters investigated were: eight levels of wheel slip range from 0% to 90% in the most extreme condition, normal load of 5 and 6 kN, inflation pressure of 20 and 29 psi, and soil compaction cone index gradient of  $4.4 \pm 0.4$  kPa and  $6.5 \pm 0.9$  kPa. The drawbar pull and sinkage of the off-road test tire was the response measured for the several combinations of the design of experiment.

The findings of this experiment show that low inflation pressure had the greatest impact on improving the drawbar pull response of the tire. The lower inflation pressure was also observed to achieve the greatest depth in sinkage, by threefold from the 0% to 75% slip, while following an exponential trend past 40% slip. The increased sinkage depth in the higher slip range is suspected to be attributed to inconsistent soil moisture content and normal load. Meanwhile, only the conditions with a higher normal load experienced the least amount of sinkage in comparison. This is suspected to be result of the higher normal load increasing the tire contact patch. The higher soil compaction was observed to follow a similar trend in wheel sinkage compared to the results of the cone index gradient measured. In general, a higher normal load, lower inflation pressure, and higher soil compaction improved the tire drawbar pull coefficient, with the exception of the higher drawbar pull having a negative impact on the tire performance past 60% slip.

From a graphing statistical standpoint, the inflation pressure resulted in having the greatest effect on the peak drawbar pull coefficient, while the normal load had mainly affected the lower slip region. The normal load was observed to consistently reduce the drawbar pull performance in the higher slip region. This soil compaction level was found to have an interaction with inflation pressure and even more on the normal load. The soil compaction level was also found to have a strong interaction with both inflation pressure and normal load in the sinkage response.

The results of the study were made possible by the several modifications done to the Terramechanics rig. The greatest of which, was the addition of the normal load controller, which is able to respond quickly to variations in the terrain while maintaining a constant normal load on the tire. The motor control for the rig was vastly improved with the newly modified remote control box and re-vamped programming control logic so that it could run efficiently and apply the desired input slip changes. Smaller improvements done to the rig helped to reduce the total preparation time and operator fatigue between test runs.

Additionally, the newly developed Wireless Internal Tire Sensors (WITS) have given the rig the ability to measure wheel sinkage. The design, development and validation of the sensors were presented to show its tire carcass deflection measurement capabilities. The angular rate and chamber angle tire could also be extracted from the data collected by WITS.

Furthermore, a great emphasis was put into developing a repeatable soil preparation procedure to ensure consistent test conditions between experiments. Additionally, laboratory test work was administered on the test soil of the study to determine unique properties of the soil, such as internal friction angle and cohesion.

## **8.1 Recommendations**

In review of the work of this study, there are several improvements that can be made to the Terramechanics rig and WITS system. The first of which, is validation of the slip changes done on the rig. While the motor control program was modified to allow slip changes, there was notable error between the desired and output speed of the wheel motor when high slip values were requested of the system. This could be improved by fine-tuning the gains in the motor control algorithm. Additionally, the WITS system can provide another source of feedback for the wheel speed.

The normal load control of the rig can also be improved to handle large variations in the terrain. As observed in high slip conditions, the wheel would sink too fast for the load controller to adapt to the change, primarily at 90% slip. Therefore, the control algorithm can use improvement, such as consideration of the nonlinearity of the system.

The rig can also benefit from a more automated method of preparing the soil. Soil preparation was the greatest delay experienced during experimental testing. Most of the time spent in the procedure required manual labor which was very exhausting for the operator. Moreover, as the fatigue on the operator increases, the likelihood of the loosening process not being executed properly increases as well. This can be avoided by modifying the rig to perform the loosening step of the soil preparation procedure. A large tiller could be attached to the rig to perform this step.

As a result of the sinkage tests, the tire was observed to sink considerably deep. This raises concern about impact the soil vane may have on the boundary layer of the undisturbed soil. As noted by a recommendation of the tire industry, the depth of the undistributed soil should be a minimum of five times the max sinkage, which is not the case in this study. This can be resolved by installing a partition along the center of the soil vane to support a larger depth of soil.

Soil moisture content (MC) was a parameter of interest to the study but was found to be too difficult to maintain and monitor. Therefore, a more controlled method of raising the moisture content and keeping it constant in a test should be investigated. The method used to monitor the MC was

also too slow as it required repetitive reheating of soil samples; this can range from 15-30 minutes, which could be enough time to allow the MC to drain in the soil and give false results. This could be resolved by employing a faster means of measuring the MC. The use of an electronic soil hydrometer may be able to provide this information.

Lastly, the WITS system can benefit from a number of improvements. The primary improvement would be to perform another set of validation testing on its current configuration; as the initial test had too much variability in the sensor-rim attachments and inflation pressure. The system can also benefit from using Lithium-ion batteries which are lighter and can have a larger energy capacity than the current alkaline batteries used. In addition to using better batteries, a charger circuit could be attached to the wheel such that it can accept a power source without needing to remove the tire. Other arrangements of the WITS optical sensors can be investigated to give more information of the contact patch, such as the deflection in the lateral direction.

## References

- [1] E. J. Pinto, "A Three Dimensional Discretized Tire Model for Soft Soil Applications," *Master Thesis.*, 2012.
- [2] I. Society of Automotive Engineers and G. I. C. Canada, *Vehicle Dynamics Terminology: SAE J670e*: Global Info Centre Canada, 1978.
- [3] J. Y. Wong, *Theory of ground vehicles*, 4th ed. Hoboken, N.J.: Wiley, 2008.
- [4] R. N. Jazar, *Vehicle Dynamics: Theory and Application*: Springer Science+Business Media, LLC, 2008.
- [5] J. Y. Wong, *Terramechanics and off-road vehicles*: Elsevier, 1989.
- [6] N. R. M. a. A. J. Green, "Effects of Test Techniques on Wheel Performance," *Journal of Terramechanics*, vol. 6, pp. 37-52, 1969.
- [7] A. C. Woodward, "Experimental Analysis of the Effects of the Variation of Drawbar Pull Test Parameters for Exploration Vehicles on GRC-1 Lunar Soil Simulant," Masters, Mechanical Engineering, Virginia Tech Blacksburg, 2011.
- [8] T. Šmerda and J. Čupera, "Tire inflation and its influence on drawbar characteristics and performance – Energetic indicators of a tractor set," *Journal of Terramechanics*, vol. 47, pp. 395-400, 2010.
- [9] R. L. Raper, A. C. Bailey, E. C. Burt, T. R. Way, and P. Liberati, "The effects of reduced inflation pressure on soil-tire interface stresses and soil strength," *Journal of Terramechanics*, vol. 32, pp. 43-51, 1995.
- [10] K. S. L. W. Y. Park, "The Effect of Dynamic Load, Inflation Pressure and Number of Passes of Tire on Soil Compaction under the Tire," *Journal of Biosystems Engineering*, vol. 27, pp. 1-10, 2002.
- [11] J. Pytka, J. Dabrowski, M. Zajac, and P. Tarkowski, "Effects of reduced inflation pressure and vehicle loading on off-road traction and soil stress and deformation state," *Journal of Terramechanics*, vol. 43, pp. 469-485, 2006.
- [12] B. P. Taylor, "Experimental Evaluation and Semi-Empirical Modeling of the Tractive Performance of Rigid and Flexible Wheels on Lunar Soil Simulant," Master of Science In Mechanical Engineering, Mechanical Engineering, Virginia Polytechnic Institute and State University, Blacksburg, 2009.
- [13] Y. Kawase, H. Nakashima, and A. Oida, "An Indoor Traction Measurement System for Agricultural tires," *Journal of Terramechanics*, vol. 43, pp. 317-327, 2006.
- [14] K. S. A. Mardani, A. Rahmani, B. Mashoofi, H. Karimmaskak, "Studies on a long soil bin for Soil-Tool interaction," *Cercetări Agronomice în Moldova*, vol. XLIII, p. 142, 2010.
- [15] V. K. Tiwari, K. P. Pandey, and A. K. Sharma, "Development of a tyre traction testing facility," *Journal of Terramechanics*, vol. 46, pp. 293-298, 2009.
- [16] B. Breuer, "The Darmstadt tire sensor - A mechatronic system to detect dynamic events within the rotating tire," *KGK-Kautschuk und Gummi Kunststoffe*, vol. 55, pp. 610-614, 2002.
- [17] T. Becherer, "The Sidewall Torsion Sensor System. 2," *DarmstädterReifenkolloquium*, p. 130, 1998.
- [18] M. V. R. a. S. N. Magori V., "On-line determination of tyre deformation, a novel sensor principle," *IEEE Ultrasonics Symp. Proc.*, pp. 485-488, 1998.
- [19] G. Erdogan, Alexander, L. and Rajamani, R., "Estimation of tire-road friction coefficient using a novel wireless piezoelectric tire sensor," *IEEE Sensors J.*, vol. 11, p. 267, 2011.
- [20] G. Erdogan, Alexander, L. and Rajamani, R., "A novel wireless piezoelectric tire sensor for the estimation of slip angle," *Meas. Sci. Technol.*, vol. 21, p. 015201, 2010.
- [21] A. Pohl, Steindl, R. and Reindl, L., "The 'intelligent tire' utilizing passive saw sensors— measurement of tire friction," *IEEE Trans. Instrum. Meas.*, vol. 48, p. 1041, 1999.

- [22] M. E. Palmer, "Wireless smart - tires for road friction measurement and self state determination," *A collection of technical papers on ... / AIAA/ASME/ASCE/AHS Structures, Structural Dynamics, and Materials Conference*, vol. 4, pp. 2728-2736, 2002.
- [23] A. J. a. H. Tuononen, L., "Optical position detection sensor to measure tyre carcass deflections in aquaplaning," *Int. J. Veh. Syst. Modelling Test.*, vol. 3, p. 189, 2008.
- [24] A. J. Tuononen, "On-board estimation of dynamic tyre forces from optically measured tyre carcass deflections," *Heavy Veh. Syst.*, vol. 16, p. 362, 2009.
- [25] A. J. Tuononen, "Optical position detection to measure tyre carcass deflections," *Veh. Syst. Dyn.*, vol. 46, p. 471, 2008.
- [26] A. J. a. M. Tuononen, M. J., "Real-time estimation of aquaplaning with an optical tyre sensor," *Proc. Inst. Mech. Eng.*, vol. 223, p. 1263, 2009.
- [27] A. J. Tuononen, "Laser triangulation to measure the carcass deflections of a rolling tire," *Measurement science & technology*, vol. 22, pp. 125304-125304, 2011.
- [28] J. Yi and E. H. Tseng, "A "smart tire" system for tire/road friction estimation," in *2008 ASME Dynamic Systems and Control Conference, DSCC 2008, October 20, 2008 - October 22, 2008*, Ann Arbor, MI, United states, 2009, pp. 847-854.
- [29] R. Matsuzaki and A. Todoroki, "Wireless flexible capacitive sensor based on ultra-flexible epoxy resin for strain measurement of automobile tires," *Sensors & Actuators: A. Physical*, vol. 140, pp. 32-42, 2007.
- [30] R. Matsuzaki, T. Keating, A. Todoroki, and N. Hiraoka, "Rubber-based strain sensor fabricated using photolithography for intelligent tires," *Sensors and Actuators: A Physical*, vol. 148, pp. 1-9, 2008.
- [31] R. Matsuzaki and A. Todoroki, "Passive wireless strain monitoring of actual tire using capacitance-resistance change and multiple spectral features," *Sensors and Actuators A (Physical)*, vol. 126, pp. 277-86, 2006.
- [32] R. Matsuzaki and A. Todoroki, "Passive wireless strain monitoring of tyres using capacitance and tuning frequency changes," *Smart Materials and Structures*, vol. 14, pp. 561-8, 2005.
- [33] J. S. Biggans, "Design of a Terramechanics Rig," Masters, Mechanical Engineering, Virginia Tech, Blacksburg, 2007.
- [34] T. N. Holley, "Empirical Analysis of the Pneumatic Tire Friction on Ice," Masters, Mechanical Engineering, Virginia Tech, Blacksburg, 2010.
- [35] D. F. B. Hopkins, J. Caffee, B. Sides, W. Burke, M. Craft, S. Taheri, "Design, Construction, and Validation of a Portable Tire Test Rig," *Journal of Materials Science and Engineering*, 2011.
- [36] Proportion-Air, "QB1 & QB2 Electro-Pneumatic Control Valves," *Brochure*, pp. 5-6, 2012.
- [37] V. T. Goodyear, "Engineered Products | Air Springs 3B12-304," *Specification Sheet*, 2008.
- [38] E. Technologies, "M1d Proportional Pneumatic Control Valve " *Datasheet*, pp. 1-2, 2010.
- [39] Parallax, "PING))) Ultrasonic Distance Sensor (#28015)," *Datasheet*, pp. 1-3, 2008.
- [40] D4643, "Test Method for Determination of Water (Moisture) Content of Soil by Microwave Oven Heating," *Annual Book of ASTM Standards*, vol. 4.08.
- [41] J. Y. Wong, *Terramechanics and off-road vehicle engineering : terrain behaviour, off-road vehicle performance and design*. Amsterdam; Boston: Butterworth-Heinemann, 2010.
- [42] J. Y. Wong, and Reece, A. R. , "Prediction of Rigid Wheel Performance Based on the Analysis of Soil-Wheel Stresses. Part I. Performance of Driven Rigid Wheels," *Journal of Terramechanics*, vol. 4, pp. 81-98, 1967.
- [43] O. Onafeko and A. R. Reece, "Soil stresses and deformations beneath rigid wheels," *Journal of Terramechanics*, vol. 4, pp. 59-80, 1967.
- [44] J. Y. Wong, and Reece, A. R. , "Prediction of Rigid Wheel Performance Based on the Analysis of Soil-Wheel Stresses. Part II. Performance of Towed Rigid Wheels," *Journal of Terramechanics*, vol. 4, pp. 7-25, 1967.
- [45] SHARP, "Wide angle Distance Measuring Sensor Unit," *GP2Y3A001K0F Datasheet*, 2006.
- [46] DIGI, "XBee ZigBee/802.15.4 Modules," *Datasheet*, 2009.

- [47] D2487, "Standard Practice for Classification of Soils for Engineering Purposes (Unified Soil Classification System)," *Annual Book of ASTM Standards*, vol. 04.08.
- [48] ASTM, "D422-63 - Standard Test Method for Particle-Size Analysis of Soils," ed: ASTM International, 2007.
- [49] D698, "Standard Test Methods for Laboratory Compaction Characteristics of Soil Using Standard Effort (12 400 ft-lbf/ft<sup>3</sup> (600 kN-m/m<sup>3</sup>)," *Annual Book of ASTM Standards*.
- [50] D2850, "Standard Test Method for Unconsolidated-Undrained Triaxial Compression Test on Cohesive Soils," *Annual Book of ASTM Standards*, vol. 04.08.
- [51] P. H. Cronjé and P. S. Els, "Improving off-road vehicle handling using an active anti-roll bar," *Journal of Terramechanics*, vol. 47, pp. 179-189, 2010.

## **Appendices**

<b>Appendix (A) Raw Data.....</b>	<b>109</b>
<b>Appendix (B) Drawbar Pull Plots .....</b>	<b>111</b>
<b>Appendix (C) Sinkage Plots .....</b>	<b>115</b>
<b>Appendix (D) WITS Circuit Diagrams and Notes.....</b>	<b>119</b>
<b>Appendix (E) Normal Load Controller Manual .....</b>	<b>124</b>

## Appendix (A) Raw Data

**Table A-1. All DOE Raw Data.**

No.	Slip	Drawbar Pull Coefficient			Max Wheel Sinkage				DOE
		Run 1	Run 2	Run 3	Run 1	Run 2	Run 3	Run 4	Cond.
1	0	0.1826	0.2024	0.1949	1.5512	1.6556	1.6061	2.0484	All Lvl 1
2	5	0.2484	0.2530	0.2503	1.5141	1.9890	1.9378	2.3182	
3	10	0.2475	0.2489	0.2482	1.7848	2.2307	2.0767	2.0289	
4	15	0.2434	0.2633	0.2495	1.9969	2.4806	2.3152	2.1385	
5	20	0.2375	0.2378	0.2597	2.3793	2.6964	2.5723	0.0000	
6	40	0.2340	0.2493	0.2467	3.4237	3.1134	3.4599	0.0000	
7	60	0.2282	0.2457	0.2373	4.2291	4.2047	4.1141	0.0000	
8	75	0.2630	0.2631	0.2668	5.1496	5.3709	4.9860	0.0000	
9	0	0.1307	0.1364	0.1200	1.0375	1.9847	1.9389	0.0000	Lvl 2 CR
10	5	0.2662	0.2646	0.2506	1.0453	2.2031	2.1450	0.0000	
11	10	0.3055	0.2806	0.2919	1.1089	2.4283	2.2032	0.0000	
12	15	0.2682	0.2727	0.2540	1.3982	2.6672	2.5029	0.0000	
13	20	0.2456	0.2454	0.2275	2.8761	2.8681	2.9535	0.0000	
14	40	0.2597	0.2876	0.2844	3.7396	3.6623	3.7095	0.0000	
15	60	0.2640	0.2881	0.2800	4.4055	4.2292	4.4829	0.0000	
16	75	0.2509	0.2883	0.2639	4.8471	4.6428	4.7192	0.0000	
17	0	0.1811	0.1672	0.1792	1.5309	1.6104	1.5504	0.0000	Lvl 2 Fz
18	5	0.2418	0.2487	0.2472	1.7979	1.7515	1.7952	0.0000	
19	10	0.2604	0.2716	0.2607	1.9270	1.9815	2.0459	0.0000	
20	15	0.2668	0.2672	0.2615	2.1765	2.3077	2.2651	0.0000	
21	20	0.2553	0.2544	0.2482	2.2460	1.4121	1.1725	0.0000	
22	40	0.2608	0.2449	0.2564	2.8846	2.4562	2.3317	0.0000	
23	60	0.2582	0.2491	0.2428	3.6442	3.3461	3.7707	0.0000	
24	75	0.2532	0.2480	0.2624	4.4838	3.9165	3.6558	0.0000	
25	0	0.2406	0.1959	0.1813	2.7178	1.8367	1.8651	0.0000	Lvl 2 TP
26	5	0.3110	0.2761	0.2888	2.9234	2.1708	2.1720	0.0000	
27	10	0.3178	0.3338	0.3238	3.1348	2.2259	2.3092	0.0000	
28	15	0.3153	0.3249	0.3253	3.1957	2.6174	2.5531	0.0000	
29	20	0.2944	0.3045	0.2999	2.5458	2.4495	2.6231	0.0000	
30	40	0.2990	0.3059	0.3149	3.7330	3.3996	3.3206	0.0000	
31	60	0.2807	0.2882	0.3064	4.4581	4.1248	3.8527	0.0000	
32	75	0.2684	0.2955	0.2930	5.7029	5.2408	5.1461	0.0000	
33	0	0.2528	0.2060	0.0000	1.9730	1.7040	0.0000	0.0000	Lvl 2 Fz & TP
34	5	0.3239	0.2694	0.0000	2.1415	1.7970	0.0000	0.0000	
35	10	0.3283	0.2755	0.0000	2.4785	1.9693	0.0000	0.0000	
36	15	0.3222	0.2495	0.0000	2.8253	2.1232	0.0000	0.0000	
37	20	0.2712	0.3242	0.0000	2.6265	2.6630	0.0000	0.0000	
38	40	0.2634	0.3046	0.0000	3.3424	3.4362	0.0000	0.0000	
39	60	0.2499	0.2786	0.0000	4.0503	4.1704	0.0000	0.0000	
40	75	0.2383	0.2828	0.0000	4.7827	4.7258	0.0000	0.0000	

41	0	0.1621	0.1590	0.1470	1.5772	1.3708	1.3920	0.0000	<b>Lvl 2 Fz &amp; CR</b>
42	5	0.2478	0.2434	0.2412	1.7421	1.4076	1.4374	0.0000	
43	10	0.2623	0.2683	0.2607	2.0098	1.7094	1.7121	0.0000	
44	15	0.2490	0.2461	0.2454	2.2612	1.8336	1.9129	0.0000	
45	20	0.2375	0.2484	0.2506	1.9444	2.5296	2.1869	0.0000	
46	40	0.2624	0.2554	0.2379	2.5947	3.3557	3.0107	0.0000	
47	60	0.2382	0.2382	0.2224	3.6383	4.1661	3.9343	0.0000	
48	75	0.2161	0.2057	0.2188	4.1839	4.8426	4.5356	0.0000	
49	0	0.1526	0.1697	0.0000	2.0625	2.1245	0.0000	0.0000	<b>Lvl 2 TP &amp; CR</b>
50	5	0.2968	0.2898	0.0000	2.0675	2.1418	0.0000	0.0000	
51	10	0.3072	0.3089	0.0000	2.2612	2.3028	0.0000	0.0000	
52	15	0.3109	0.3258	0.0000	2.6755	2.4216	0.0000	0.0000	
53	20	0.3073	0.2930	0.0000	3.0625	4.0349	0.0000	0.0000	
54	40	0.3138	0.2883	0.0000	3.6108	4.3323	0.0000	0.0000	
55	60	0.2857	0.3010	0.0000	4.3033	4.5726	0.0000	0.0000	
56	75	0.3002	0.3374	0.0000	4.6590	4.6052	0.0000	0.0000	
57	0	0.2529	0.1765	0.0000	1.5876	1.0212	0.0000	0.0000	<b>All Lvl 2</b>
58	5	0.3232	0.2387	0.0000	1.7491	1.3938	0.0000	0.0000	
59	10	0.3256	0.2684	0.0000	2.0219	1.5688	0.0000	0.0000	
60	15	0.3304	0.2732	0.0000	2.2319	1.8844	0.0000	0.0000	
61	20	0.2726	0.2558	0.0000	1.8793	1.7780	0.0000	0.0000	
62	40	0.2715	0.2447	0.0000	2.7167	2.6886	0.0000	0.0000	
63	60	0.2435	0.2423	0.0000	3.5168	3.4989	0.0000	0.0000	
64	75	0.2250	0.2232	0.0000	4.3786	4.0998	0.0000	0.0000	

## Appendix (B) Drawbar Pull Plots

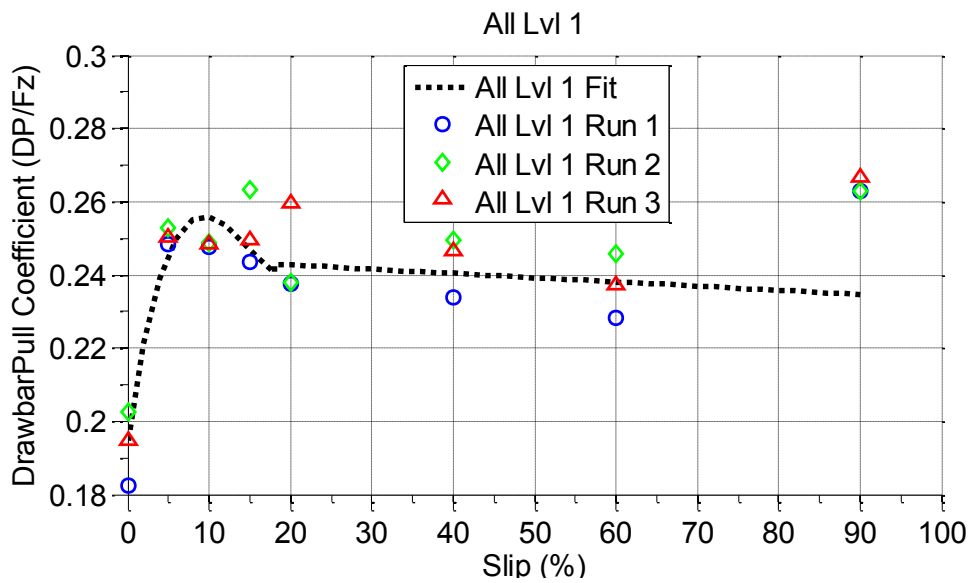


**Figure B-1. DP of three runs of all parameters held at level 1; specifically 5 kN load, 29 psi inflation pressure, and 4.4 kPa/mm cone index gradient.**

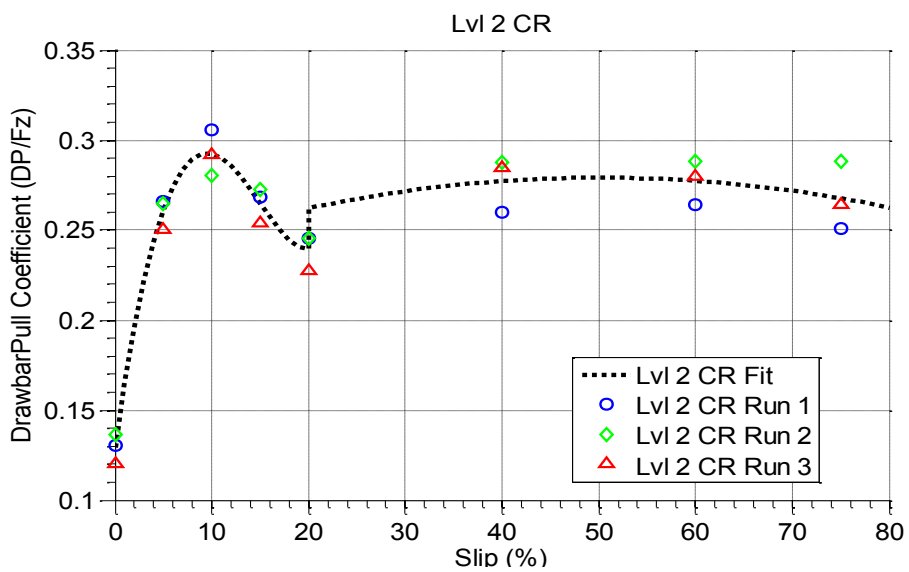


**Figure B-2. DP of three runs of soil compaction held to level 2; specifically 5 kN load, 29 psi inflation pressure, and 6.5 kPa/mm cone index gradient.**

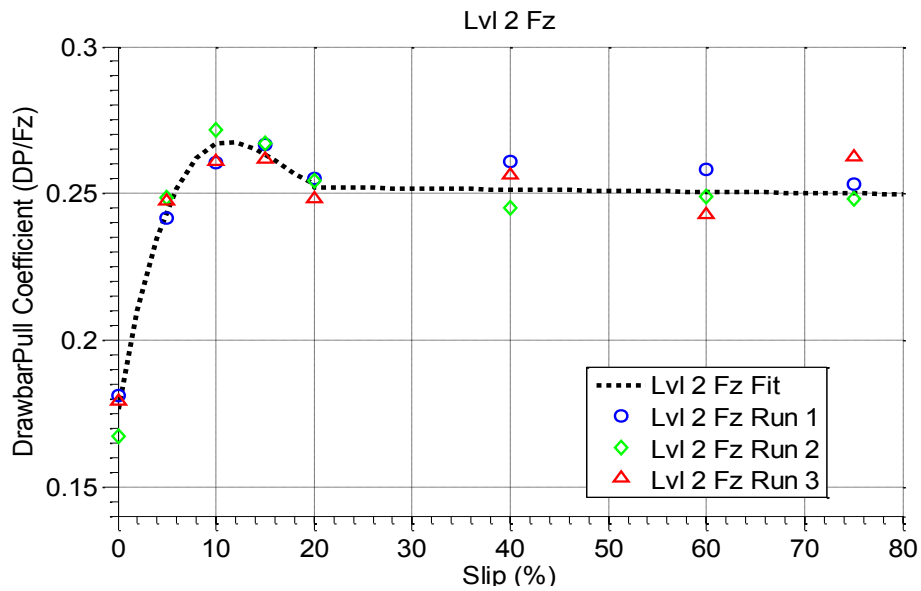


Figure B-3. DP of three runs of normal load held to level 2; specifically 6 kN load, 29 psi inflation pressure, and 4.4 kPa/mm cone index gradient.

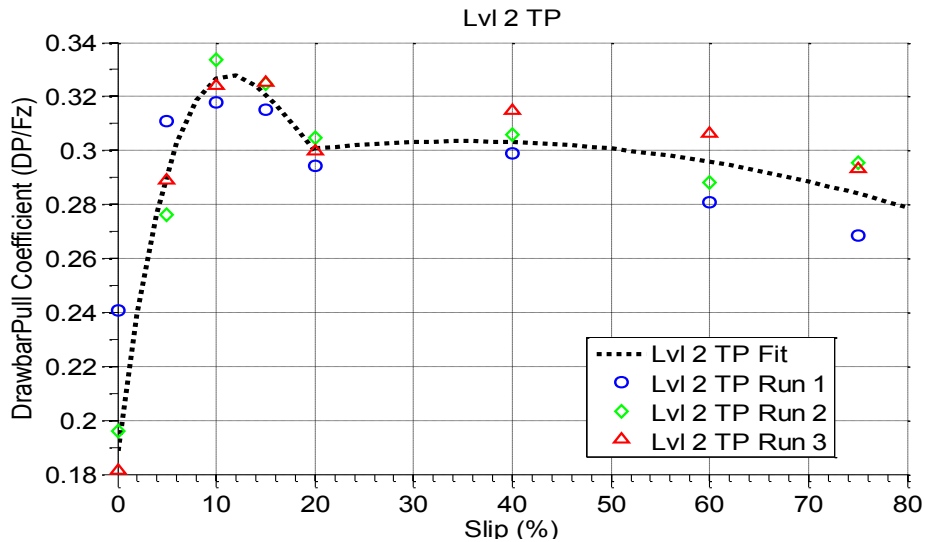
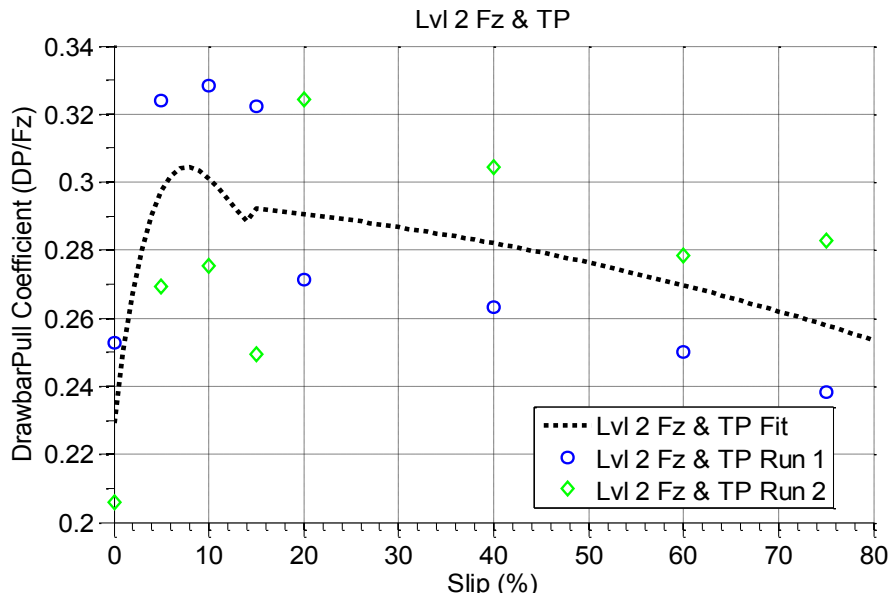
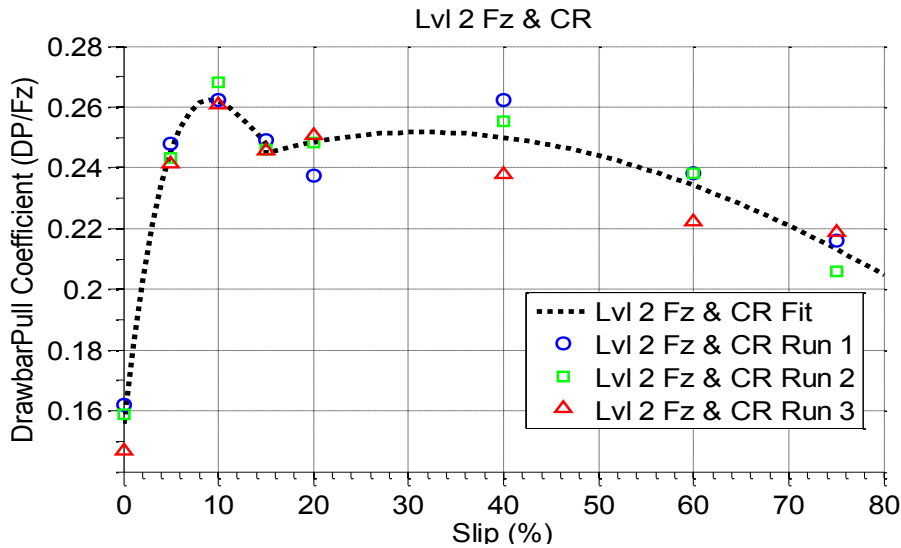


Figure B-4. DP of three runs of inflation pressure held to level 2, specifically 5 kN load, 20 psi inflation pressure, and 4.4 kPa/mm cone index gradient.



**Figure B-5. DP of two runs of both normal load and inflation held at level 2, specifically 6 kN load, 20 psi inflation pressure, and 4.4 kPa/mm cone index gradient.**



**Figure B-6. DP of three runs of normal load and soil compaction held at level 2, specifically 6 kN load, 29 psi inflation pressure, and 6.5 kPa/mm cone index gradient.**

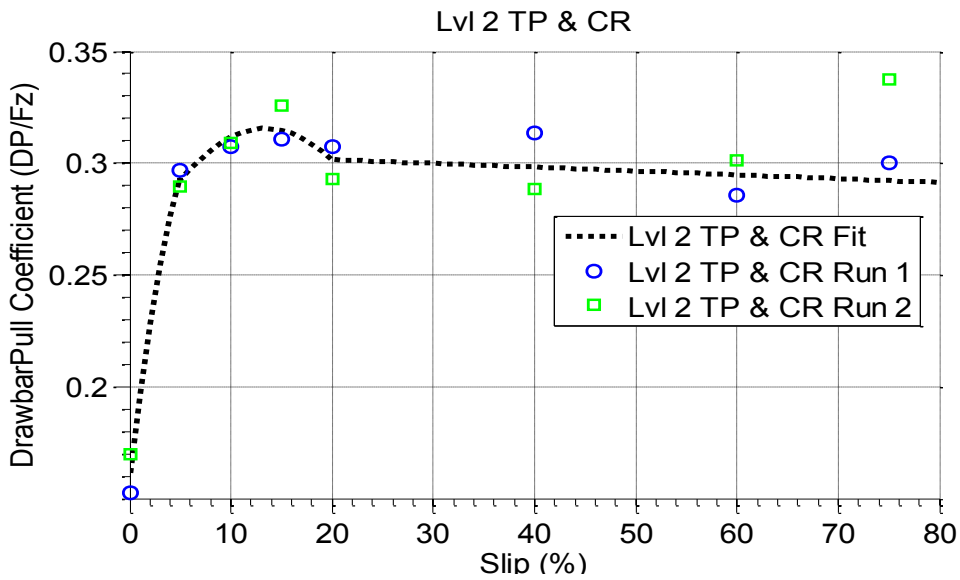


**Figure B-7. DP of two runs of both inflation pressure and soil compaction held at level 2, specifically 5 kN load, 20 psi inflation pressure, and 6.5 kPa/mm cone index gradient.**

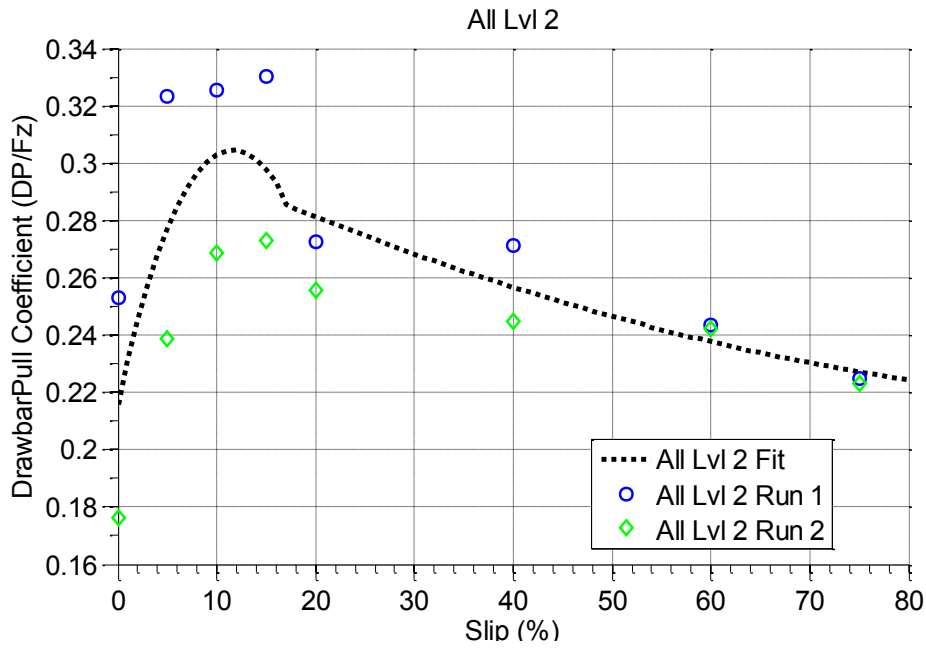


**Figure B-8. DP of two runs of all parameters held at level 2, specifically 6 kN load, 20 psi inflation pressure, and 6.5 kPa/mm cone index gradient.**

## Appendix (C) Sinkage Plots

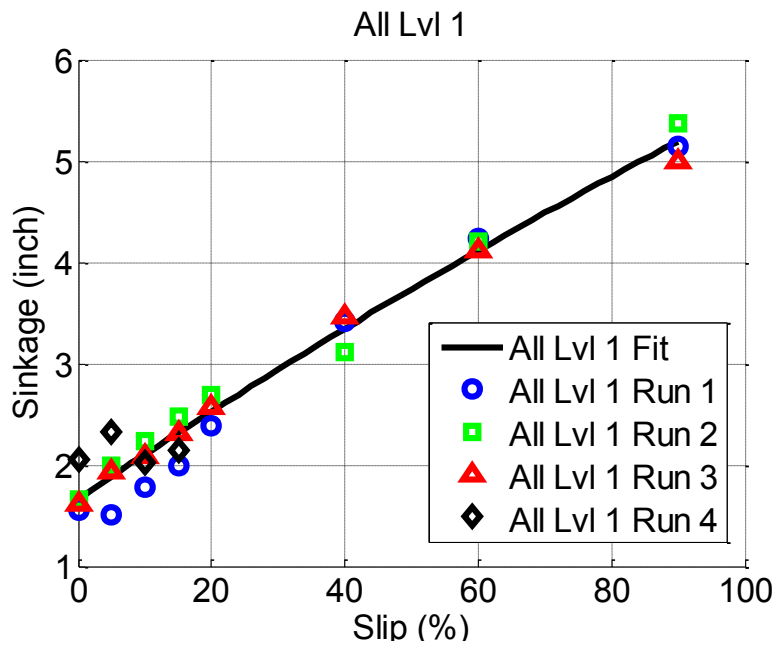


Figure C-1. Sinkage of three runs of all parameters held at level 1, specifically 5 kN load, 29 psi inflation pressure, and 4.4 kPa/mm cone index gradient.

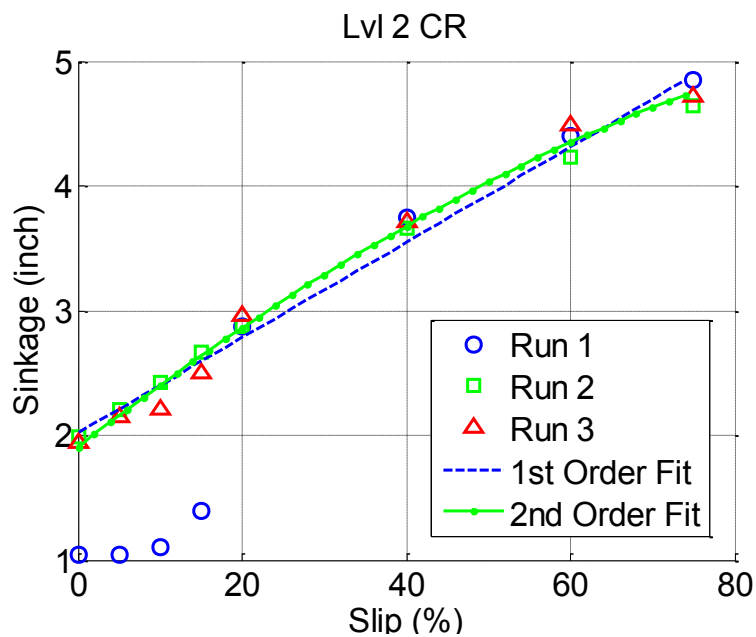


Figure C-2. Sinkage of three runs of soil compaction held to level 2; specifically 5 kN load, 29 psi inflation pressure, and 6.5 kPa/mm cone index gradient.

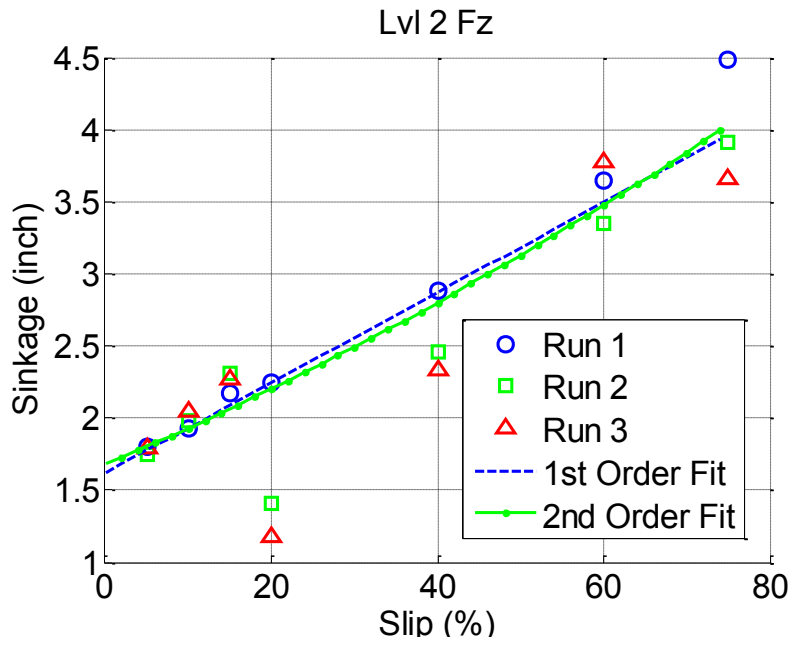


Figure C-3. Sinkage of three runs of normal load held to level 2; specifically 6 kN load, 29 psi inflation pressure, and 4.4 kPa/mm cone index gradient.

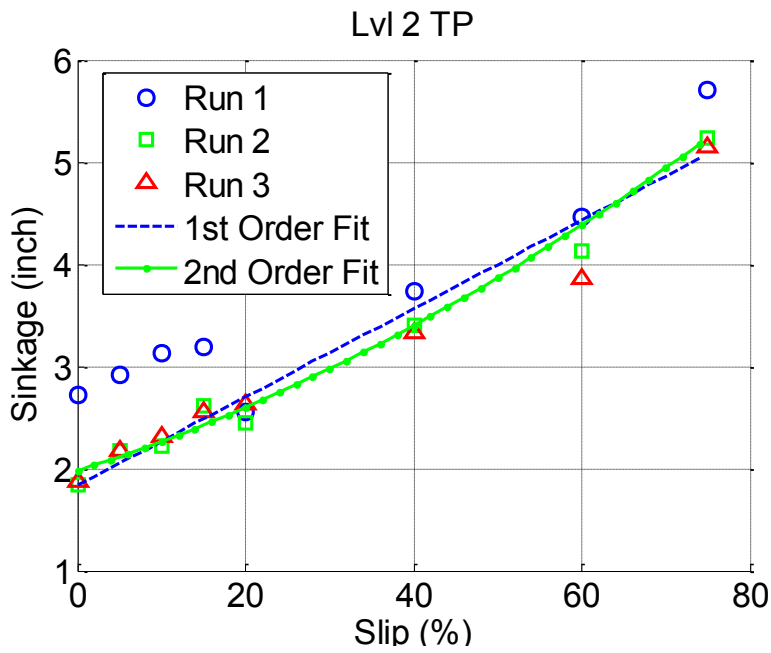
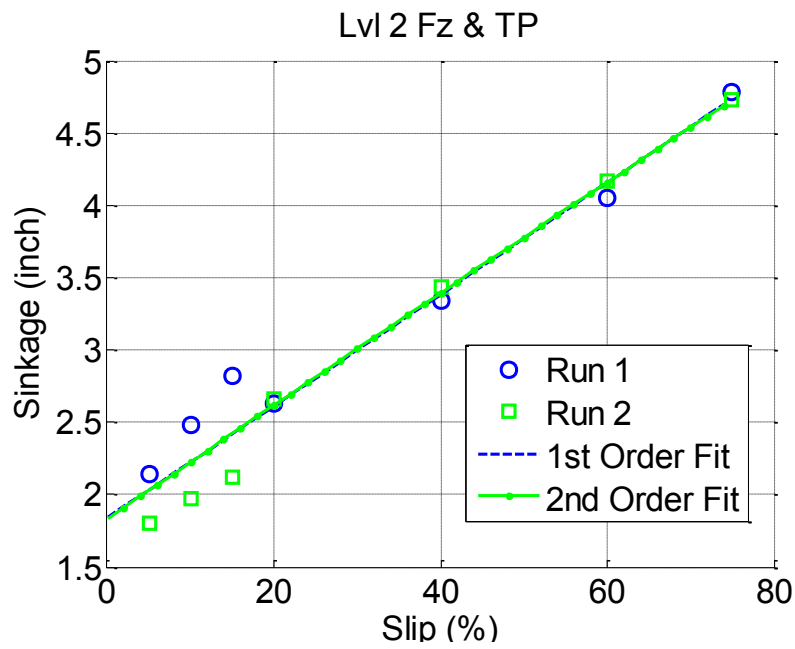
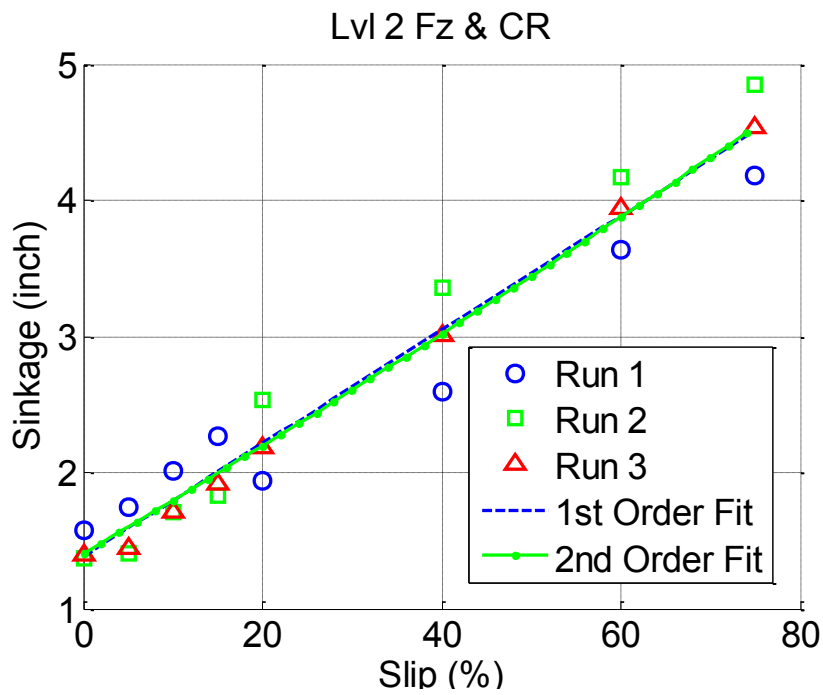


Figure C-4. Sinkage of three runs of inflation pressure held to level 2, specifically 5 kN load, 20 psi inflation pressure, and 4.4 kPa/mm cone index gradient.



**Figure C-5. Sinkage of two runs of both normal load and inflation held at level 2, specifically 6 kN load, 20 psi inflation pressure, and 4.4 kPa/mm cone index gradient.**



**Figure C-6. Sinkage of three runs of normal load and soil compaction held at level 2, specifically 6 kN load, 29 psi in-flation pressure, and 6.5 kPa/mm cone index gradient.**

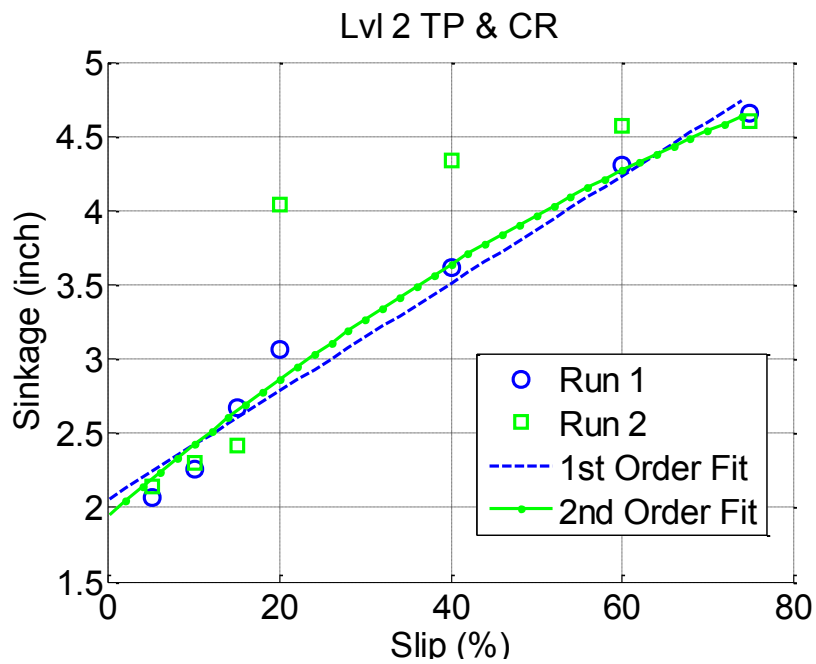


Figure C-7. Sinkage of two runs of both inflation pressure and soil compaction held at level 2, specifically 5 kN load, 20 psi inflation pressure, and 6.5 kPa/mm cone index gradient.

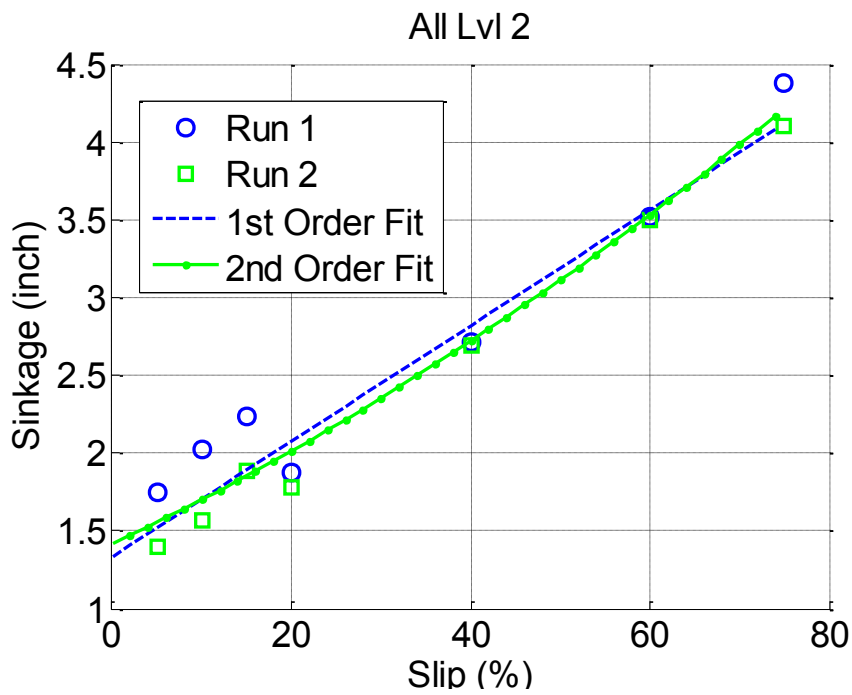


Figure C-8. Sinkage of two runs of all parameters held at level 2, specifically 6 kN load, 20 psi inflation pressure, and 6.5 kPa/mm cone index gradient.

# Appendix (D) WITS Circuit Diagrams and Notes

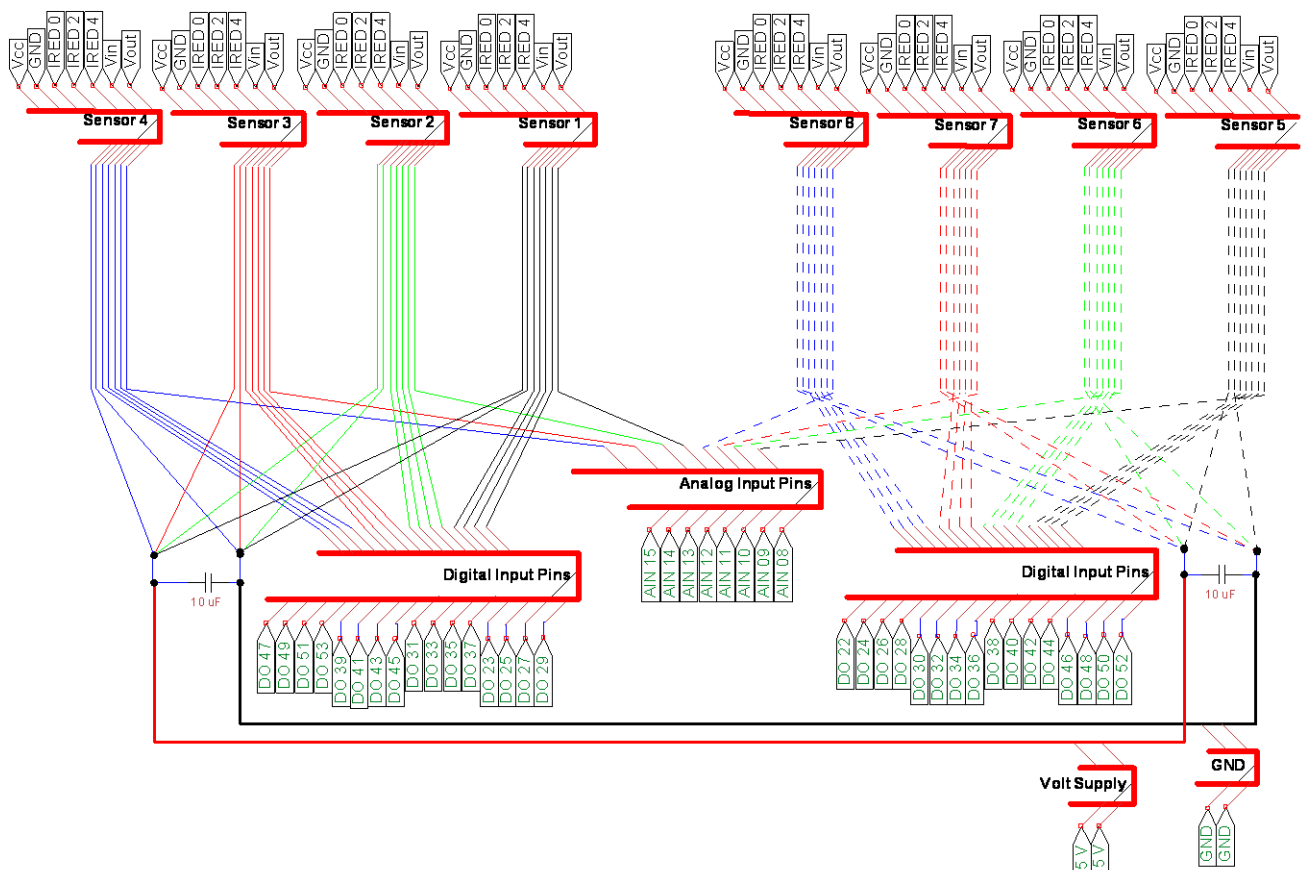


Figure D-1. Wire harness for all sensors to connect to the microcontroller.

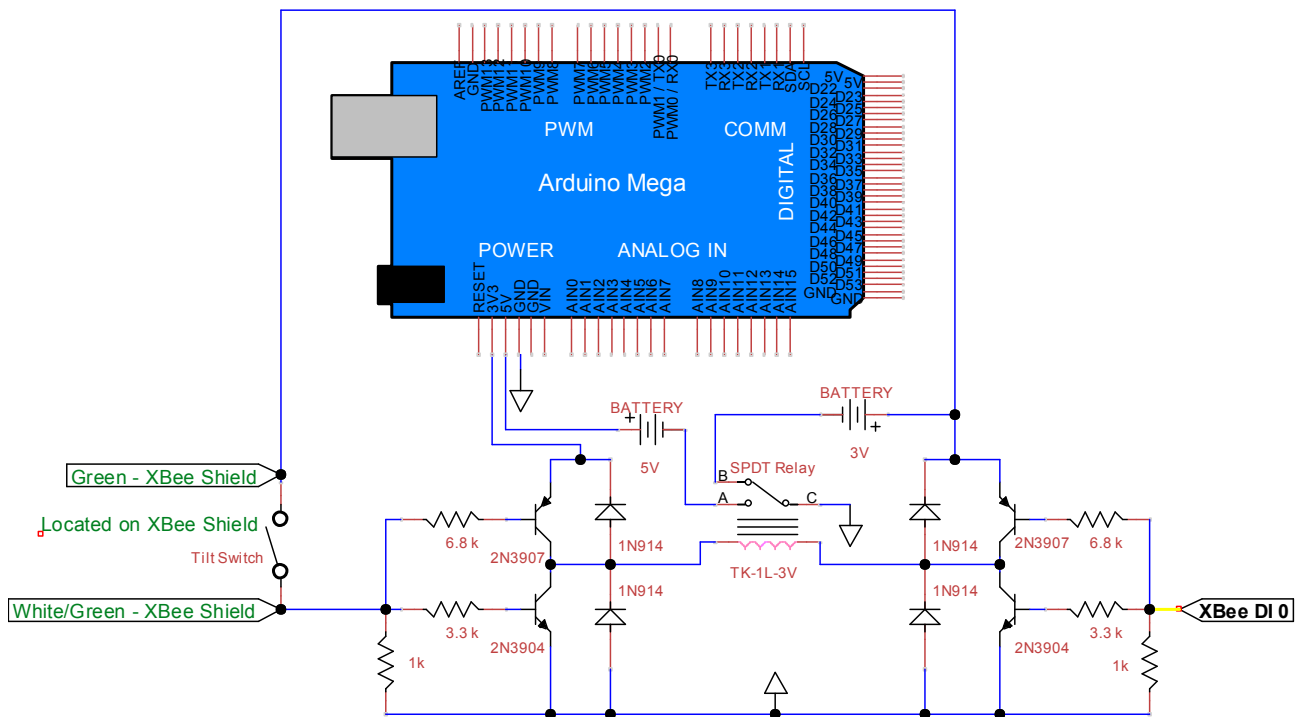
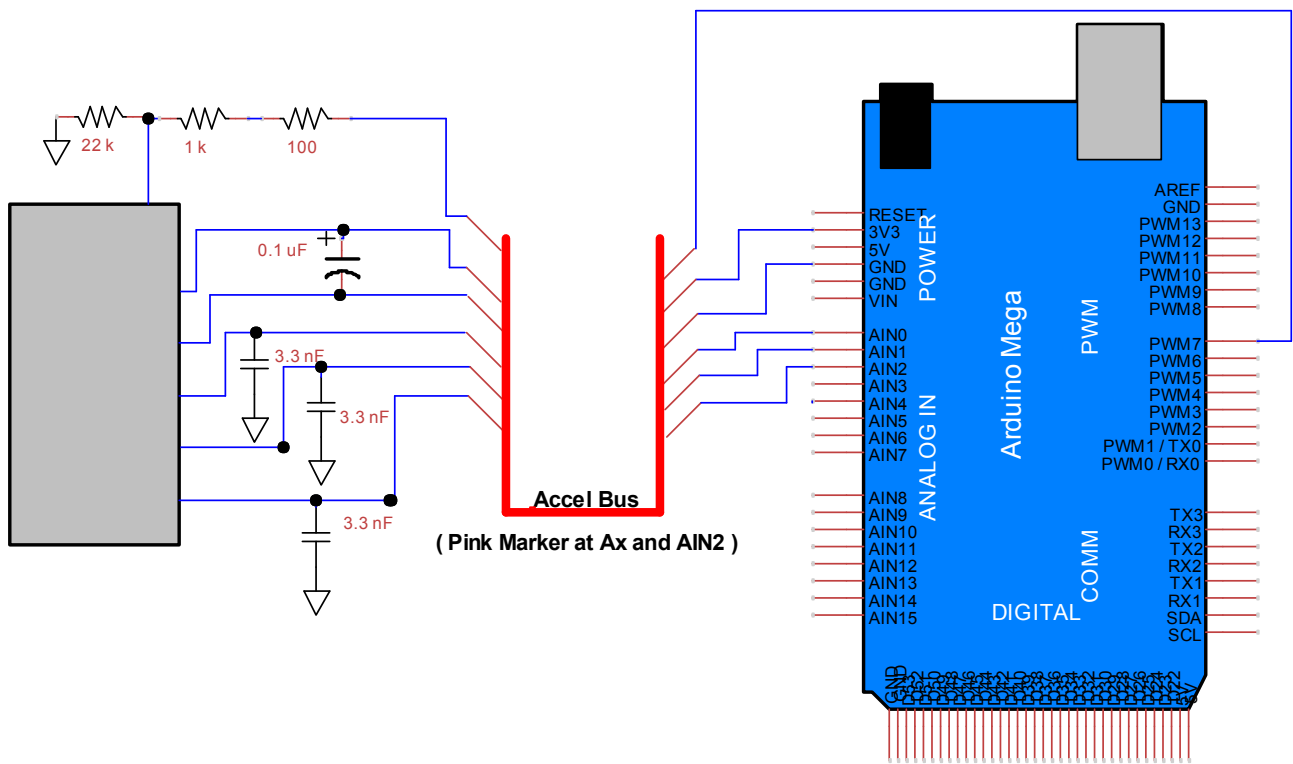
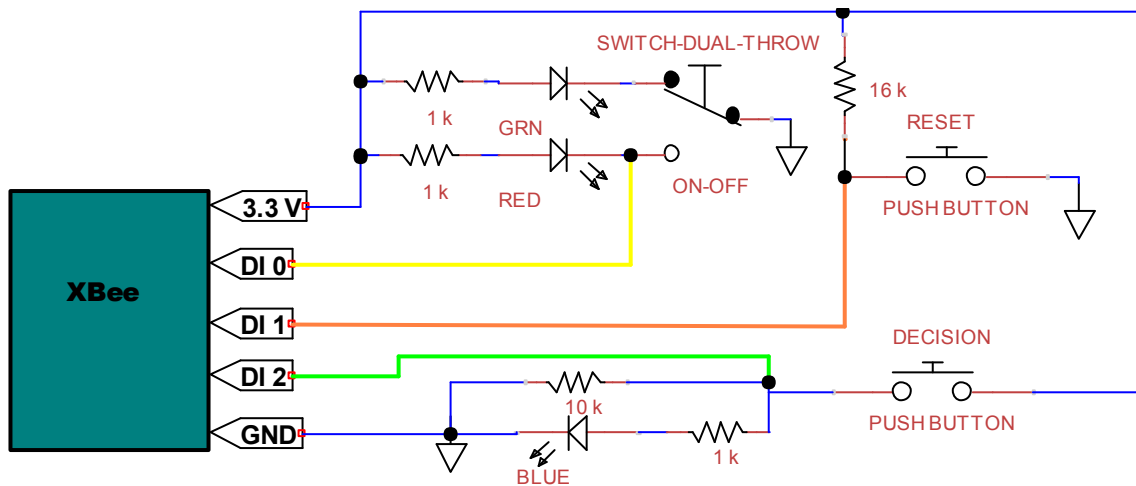


Figure D-2. H-bridge circuit that controls the relay that supplies power to the microcontroller

The H-bridge circuit in Figure D-2 is used to connect and disconnect the WITS system from its main power source via the single-pole-double-throw relay. The circuit connects the WITS system to its power source when the tilt switch connects with its own power supply. When WITS (on the wheel) is positioned in the second and third quadrant of the wheel (ON position), the tilt switch makes a connection, otherwise, if in the first and fourth quadrant of the wheel (OFF position) the tilt switch remains disconnected, with respect to the operator observing the face of the wheel. When WITS is in the OFF position, either the first or fourth quadrant of the wheel face, and the operator XBee in Figure D-4 is switched to illuminate the green LED, WITS will power off. If WITS is in the ON position and the green LED is illuminated, then the tilt switch and the XBees will repeatedly switch the polarity of the relay coil, wasting both the main and tilt switch power supplies. The operator should avoid this condition if the wheel is not in motion; otherwise this condition can be used to conserve the power when the wheel is rotating to warm up or being used to prepare soil.



**Figure D-3. Accelerometer to microcontroller connection, made directly to the SD logger shield rather than the microcontroller itself.**



**Figure D-4. Operator XBee circuit to communicate with the microcontroller.**

The dual-throw switch in Figure D-4 is used to give the WITS-connected XBee permission to power the WITS system on or off. If the green LED is illuminated, WITS will not turn on. If the red LED is illuminated, WITS may be powered on if the tilt switch is in position to trigger the H-bridge circuit. The reset push button simply resets the running WITS program to the original menu. The decision push button allows the user to select the options in the WITS menu via the number of times the decision button is pressed. To activate the use of the decision button, the operator must repeatedly press the button until the WITS program recognizes it and awaits the input. If WITS does not recognize the decision button input, the operator needs to reset the program and try again. The decision button was made to allow the operator to communicate with WITS when text input over the serial connection is not working. This has been observed to occur often after the operator XBee has been disconnected and reconnected to the operator computer.

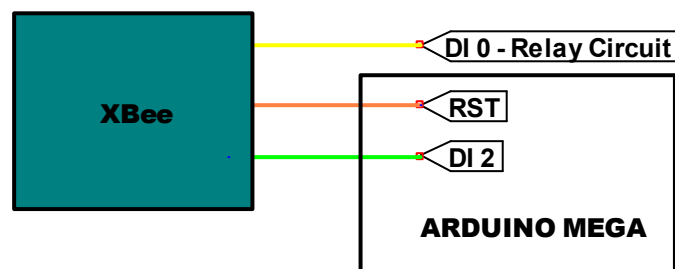


**Figure D-5. XBee to microcontroller connection. Digital signals are passed from the operator.**

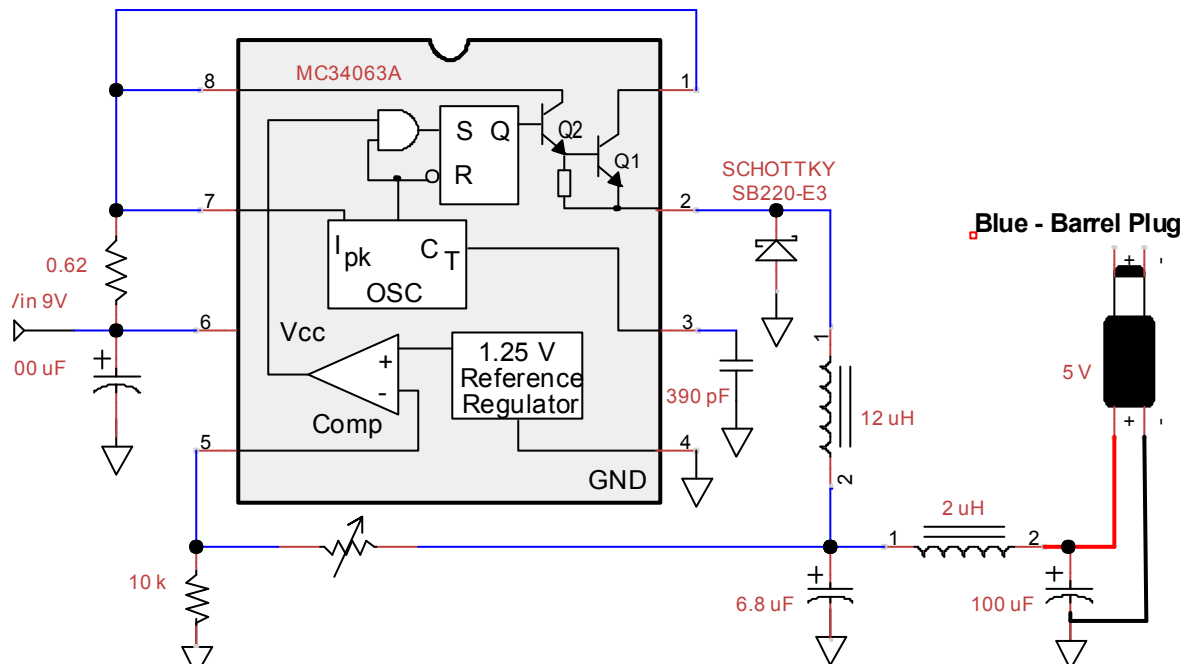


**Figure D-6. DC to DC converter circuit used to provide a clean 5 V power to the WITS system.**

Note that some of the components of the step down voltage regulator circuit in Figure D-6 may differ than what is currently on the circuit but the components should still provide a near exact response of providing a clean 5 V power from the input 9 V power.

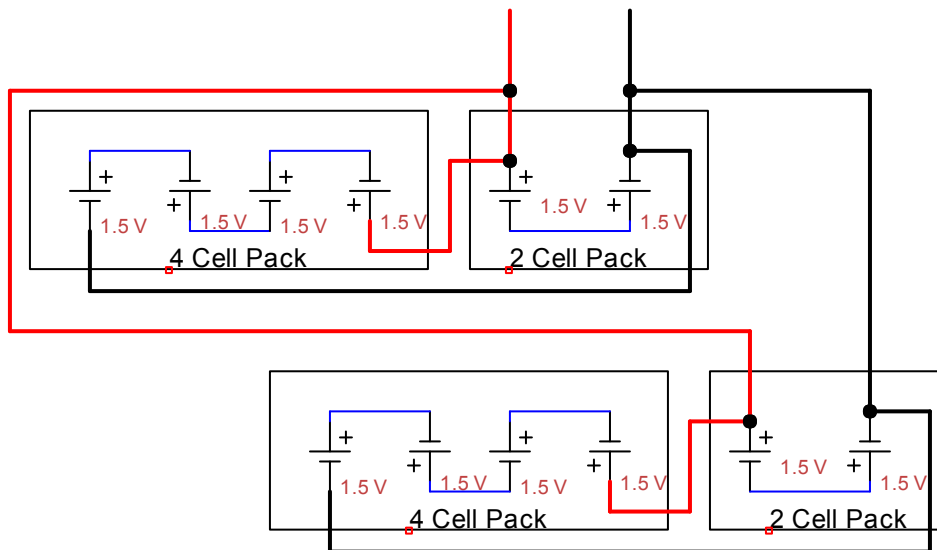


**Figure D-7. Several batteries in series and parallel provide a 9 V voltage battery power supply for the DC-DC converter circuit used to power the WITS system.**

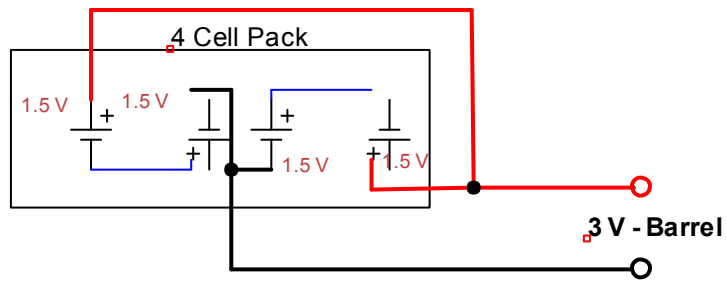


**Figure D-8. Battery pack for the tilt switch used to trigger the WITS system to power on when disconnected from its own power supply.**

## Appendix (E) Normal Load Controller Manual

1. Calibrate Kistler sensor prior to use of the normal load controller.
2. Start Normal load Control LabVIEW VI.

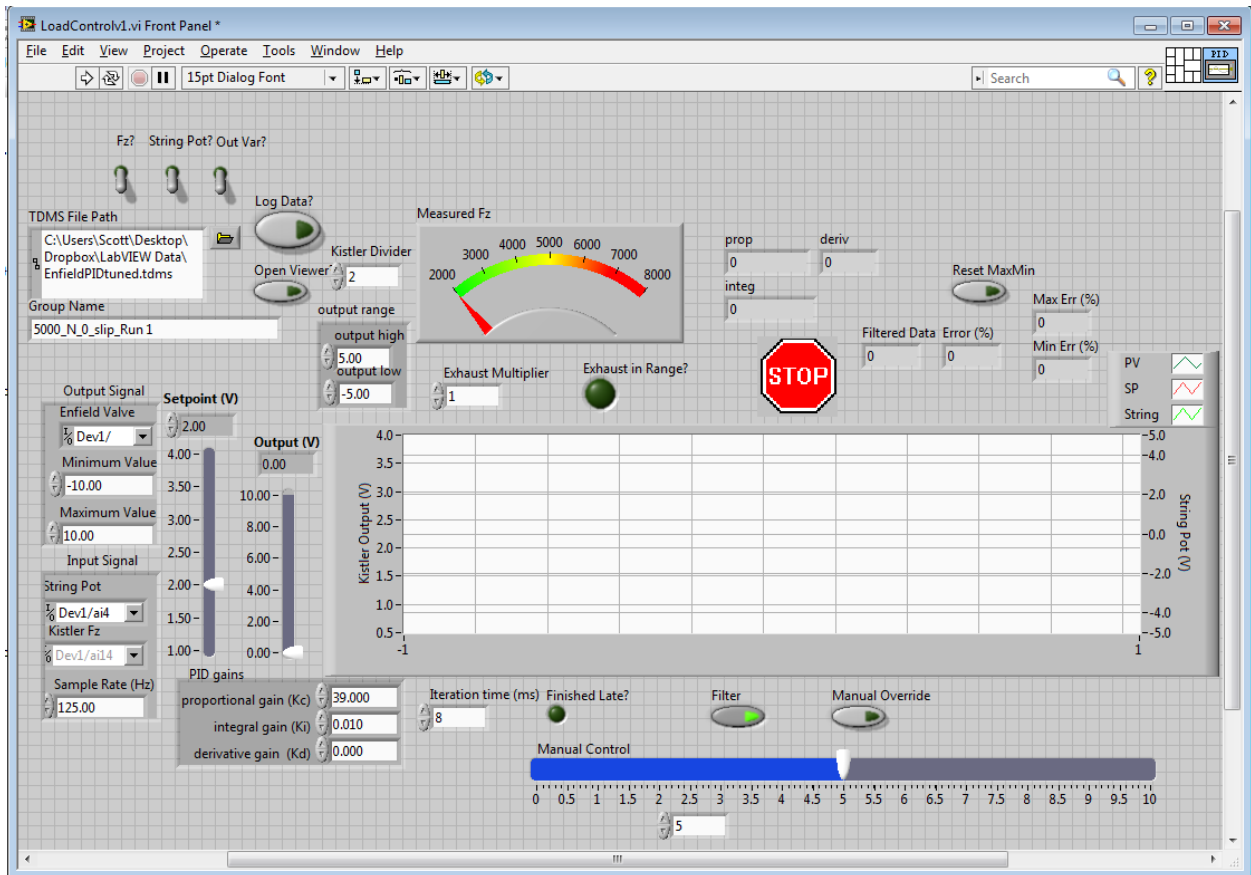


Figure E-1. LabVIEW VI used for normal load control.

### 3. Power On Electronics

- a. Must provide at least 24 VDC nominal (12 – 36 VDC) at 1.1 A max of power.



Figure E-2. Voltage supply for the electro-pneumatic control valve.

Note Figure E-2 shows a variable power supply. This can be easily replaced with a fixed power supply of 24VDC and 1.1 A max current and a switch to power off and on. This should be done in the future to reduce clutter at the Terramechanics rig computer desk and utilize the variable power supply for other developing electronic projects.

#### 4. Supply Air

- a. Release supply air lever
- b. Confirm manual regulator reads 70 psi. Adjust as needed.



**Figure E-3. Manual regulator and filter for the inlet supply air of the electro-pneumatic control valve.**

#### 5. Run VI Program as Need